Retrieval of Surface Emissivity of Sea Ice and Temperature Profiles over Sea Ice from Passive Microwave Radiometers

von
M.Sc. Applied Phys. Nizy Mathew

24. Mai 2007

Contents

Abstract

Polar regions play a key role in the global climate. The information on atmospheric parameters in these regions is sparse. Among the polar surfaces, sea ice varies in extent and physical properties with region and season and so does the surface emissivity.

In the present study a method to retrieve the emissivity is applied over two selected regions in the Arctic, one covered by first-year ice and the other by multiyear ice and it investigates the application of them in the improvement of temperature profile retrieval over sea ice.

The retrieval of surface emissivity is done by combining simulated brightness temperatures with the satellite measured brightness temperature. In order to determine the surface emissivity of sea ice, the observations of the microwave instruments AMSU (Advanced Microwave Sounding Unit) and AMSR-E (Advanced Microwave Scanning Radiometer- Earth Observing System) are used.

Determination of emissivity requires the knowledge of the temperature of the emitting layer. The penetration depth of microwaves in sea ice varies between millimeters and decimeters depending on the frequency and micro-physical structure. A year-round observation of temperature profiles of sea ice from the Surface Heat Budget of the Arctic Ocean (SHEBA) campaign at a first-year and a multiyear ice site is used to derive a set of coefficients a and b to linearly relate the lowest level air temperature and the different emitting layer temperatures. The method accounts for the variation of the penetration depth with frequency, air temperature and sea ice temperature.

An algorithm to retrieve temperature profiles from AMSU data is modified using the retrieved emissivities and the derived temperature correction factors so that the retrieval accuracy of temperature profiles over sea can be improved.

5

List of Publications

Parts of the works presented in this thesis have been published and presented at conferences.

Reviewed

Mathew, N., Heygster, G., Melsheimer, C. and Kaleschke, L., 2006: Surface emissivity of Arctic sea ice at AMSU window frequencies. *IEEE Trans. Geosci. Rem. Sens.* accepted.

Mathew, N., Heygster, G., 2007: Surface emissivity of Arctic sea ice at AMSR-E frequencies. *IEEE Trans. Geosci. Rem. Sens..* In preparation.

Proceedings/Reports/Abstract

Mathew, N., Heygster, G. and Rosenkranz, P. W., 2006: Retrieval of emissivity andtemperature profile in polar regions. In Proc. *IGARSS 2006.*

Mathew, N.: Retrieval of Surface Emissivity and Temperature Profiles in Polar Regions, 22-06-2006, *1st workshop on Remote sening and modelling of surface properties, Paris, France.*

Mathew, N., Heygster, G.: Comparison of Retrieved Temperature Profiles from AMSU and Radiosonde Data in Polar Regions, 03-04-2006, *EGU-2006, Vienna, Austria.*

Mathew, N., Heygster, G.: Surface emissivity of polar regions from AMSU data, *2nd Alfred Wegener Symposium* (30 October – 02 November 2005, Alfred Wegener Institute and German Maritime Museum, Bremerhaven, Germany).

Heygster, G., Melsheimer, C., Mathew, N., Toudal, L., Saldo, R., Andersen, S., Tonboe, R., Schyberg, H., Tveter, F. T., Thyness, V., Gustafsson, N., Landelius, T., Dahlgren, P. and Perov, V., 2006: Integrated Observation and Modeling of the Arctic Sea ice and Atmosphere. *Tech. Rep., IUP, University of Bremen. Final Report for EU project EVK-CT-2002-00067.*

1 Introduction

The polar regions play a key role in the global climate system. They strongly contribute to the energy balance and they act as indicators for global warming because the global warming is especially pronounced in the Arctic. Therefore, a precise and continuous survey of the atmospheric temperature profile is essential input for global circulation models. In addition such profiles are needed input to numerical weather prediction models. Atmospheric temperature profiles are used to assess response of the global climate system to increasing greenhouse effect due to anthropogenic activities. Due to the hostile conditions of polar regions, in-situ measurements of atmospheric parameters such as temperature and humidity profiles are very sparse.

The coverage of the polar regions with polar orbiting satellite temperature sounding passive microwave radiometers is dense. Instruments like AMSU, SSMIS cover large parts of the Arctic about 10 times a day. The Arctic atmosphere is often very dry and the surface signal is usually significant. Therefore, in order to retrieve atmospheric parameters from satellite borne measurements in these regions, a reliable estimate of the emissivity of sea ice, snow, land ice and open water is required (Selbach, 2003; Haggerty and Curry, 2002; Rosenkranz, 2006). Among the polar surfaces, sea ice is very important. It covers $5-8\%$ of Earth's surface. However, as it is highly variable in extent and surface properties presently no operational surface emissivity model exists for sea ice.

In this thesis, in order to determine the surface emissivity of sea ice, observations of the microwave instruments AMSU (Advanced Microwave Sounding Unit) on the polar orbiting satellites of National Atmospheric and Oceanic Administration (NOAA), NOAA-15, -16, -17 and AMSR-E (Advanced Microwave Scanning Radiometer- Earth Ob-

serving System) on Aqua satellite are used. AMSU instruments were found efficient in atmospheric and surface parameter studies in low and mid latitudes (Rosenkranz, 2001; Weng et al., 2003; Hong et al., 2005; Karbou et al., 2005b). The passive microwave radiometers AMSU consists of two modules 'A' and 'B'. The AMSU-A has 15 channels in the frequency range $23-89$ GHz, with window channels at 23.8, 31.4, 50.3 and 89 GHz and 11 temperature sounding channels between 50 and 60 GHz. The AMSU-B has 5 channels in the frequency range $89-183$ GHz. AMSU is a cross-track scanning radiometer.

Imaging Microwave sensors such as SSM/I and AMSR-E are widely used for the study of surface parameters such as near real time (NRT) sea ice concentration (Spreen et al., 2005, 2007), snow cover, ice temperature (Comiso et al., 2003) and cloud signatures (Miao et al., 2000). AMSR-E was developed by the Japan Aerospace Exploration Agency (JAXA). It has 14 channels at six different window frequencies ranging from $6-89$ GHz, each measuring radiance in both vertical and horizontal polarizations (Kawanishi et al., 2003).

In contrast to sea ice, the ocean surface is radiatively cool and ocean emissivity models have been developed (English and Hewison, 1998; Wentz, 1983) and are satisfactory for the use in atmospheric applications. For sea ice also, such models have been developed, but they are far from the state of maturity required for operational application (Fuhrhop et al., 1997, 1998; Tonboe et al., 2006; Heygster et al., 2006). Therefore, here sea ice emissivity is determined empirically.

Various efforts have been made to retrieve land surface emissivity from satellite observations in the microwave frequencies. Land surface emissivities have been calculated using AMSU observations and are used effectively for atmospheric temperature and humidity retrieval (Karbou et al., 2005b,a). Quantitative knowledge of the spatial and temporal variability of surface emissivity is essential for the retrieval of atmospheric parameters over polar regions from space borne microwave observations (Melsheimer and Heygster, 2005; Haggerty and Curry, 2002). A global scale investigation of sea ice emissivities in the microwave frequency region was done by Comiso (1983) using both infrared and microwave measurements at SMMR frequencies. However, they are different from the AMSU observing frequencies. Temporal

variation of first-year and multiyear ice emissivity from ground measurements limited in space and time is reported by Grenfell and Lohanick (1985); Grenfell (1992). Moreover, emissivities of different ice types and snow are calculated from airborne measurements. Hollinger et al. (1984) have determined emissivities at a frequency range of 19 – 140 GHz for different Arctic ice types during the freeze-up period in October. Hewison and English (1999) have retrieved the surface emissivity in the frequency range of 24 – 157 GHz over the Baltic sea ice and snow sites on land. However, the Baltic sea ice has lower salinity than the Arctic sea ice. Haggerty and Curry (2001) have retrieved the emissivity of sea ice at 37, 89, 150 GHz and 220 GHz near the SHEBA ice camp in May and July. They assumed lowest level air temperature as surface temperature. During this period, the temperature difference between atmospheric temperature and ice temperature is only about 1 K. However, their surface temperature assumptions are not valid in the freezing period.

Determination of emissivity requires the knowledge of the temperature of the emitting layer. The penetration depth of microwave in sea ice varies between millimeters and decimeters depending on the frequency and micro-physical structure. Typically, the snow surface temperature is considerably lower than the ice temperature, which in turn is lower than the temperature of water underneath the ice ($-1.8\,^\circ$C). In most of the above cited studies on sea ice emissivity the temperature of the emitting layer has been assumed to be equal to the infrared measured surface temperature. The error is small during late spring and summer when the snow or ice is relatively isothermal (Haggerty and Curry, 2001). During winter, this is a potential source of error because of the temperature gradient in the sea ice and the resulting overestimation of emissivity (Tonboe, 2006).

A year-round observation of temperature profiles of sea ice from the Surface Heat Budget of the Arctic Ocean (SHEBA) campaign at a first-year and a multiyear ice site is used to derive a set of coefficients a and b to linearly relate the lowest level air temperature and the different emitting layer temperatures. The method accounts for the variation of the penetration depth with frequency, air temperature and sea ice temperature.

In the present study a method to retrieve the emissivity is applied over two selected regions in the Arctic, one covered by first-year ice and the other by multiyear ice. In order to retrieve the surface emissivities, simulated brightness temperatures based on atmospheric model profiles of temperature and humidity from ECMWF and AMSU brightness temperatures from corresponding satellite over-passes are used. Corrections are made to the lowest level air temperature in order to get the principal emitting layer temperatures. Sea ice emissivities are retrieved from AMSR-E at two test regions where the AMSU emissivity retrieval has been done. AMSR-E measures radiance at both horizontal and vertical polarizations whereas AMSU measures only in one mixed polarizations mode. The AMSR-E retrieved emissivities at two polarizations are combined together to simulate the AMSU polarization combinations for comparison.

An existing temperature retrieval algorithm (Rosenkranz, 2006), is modified to improve the temperature profile application over sea ice by using the retrieved sea ice emissivities and the derived temperature correction factors. The modification of the algorithm is done by:

1. providing varying *a-priori* surface emissivities for each month
2. deriving the emitting layer temperature from the lower level air temperature
3. modifying surface brightness temperature retrieval.

The organization of the thesis is as follows:

Chapter 2 gives a short introduction to physical and electromagnetic properties of sea ice, snow and atmosphere and the principles behind microwave radiometry.

Chapter 3 describes about the satellite instruments AMSU and AMSR-E and SHEBA data, Polarstern data and ECMWF data, which are used to study emissivity of sea ice and to retrieve temperature profiles.

Chapter 4 outlines the method adopted to retrieve surface emissivity of sea ice using the data from satellite radiometers. The method is validated over open water.

Chapter 5 describes surface temperature assumptions for the surface emissivity retrieval.

Chapter 6 shows the emissivities retrieved using the data obtained from the satellite instruments AMSU and AMSR-E.

Chapter 7 introduces optimal estimation method used for the temperature profile retrieval.

Chapter 8 shows the comparison of the retrieved temperature profiles with radiosonde measured temperature profiles.

Chapter 9 presents the modification made to the retrieval algorithm to improve the temperature profile retrieval over sea ice and the results.

Chapter 10 presents the conclusions and outlook.

2 Theory

Polar surfaces of consideration in this study are sea ice and snow. The physical and electrical properties of them are described in sections 2.1 and 2.2 respectively. The properties of atmosphere are described in section 2.3. In order to study the surface and the atmosphere of polar regions, passive microwave radiometry is very useful. It measures the radiation emitted naturally by Earth's surface and atmosphere. It doesn't need sun light, it can easily penetrate clouds and no emitting sources are required, to name a few advantages of passive microwave radiometry over visible/infrared sounding and radars. The microwave region generally spans the range from about 3 GHz to 300 GHz. Section 2.4 of this chapter describes the basic theory of passive microwave radiometry.

2.1 Sea Ice

Sea ice forms at the ocean surface when the surface temperature drops below the freezing point. The freezing point for salty ocean water is about $-2\,°C$, slightly colder than it is for fresh water ($0\,°C$). When sea ice forms, salt is expelled from the ice crystal structure, but the ice still ends up being slightly salty. This is distinct from the land ice (ice shelves), which originally formed from snow falling on land, and so is completely fresh. The scattering and emission of microwave by sea ice are highly sensitive to even small variation in its composition and structure (Tucker III et al., 1992).

Sea ice covers $5-8\,\%$ of Earth's surface. It plays an important role in global energy balance and atmospheric and oceanic circulation. The albedo of sea ice ($0.45-0.98$) is much higher than that of open water

(0.03 – 0.1). Consequently, sea ice reflects much more solar radiation, which results in negative surface radiation budget and strong surface air temperature inversion. During summer, when sea ice melts, all available solar energy is used to melt the sea ice and covering snow. So the surface air temperatures become low and hence water vapor in the air. Hence sea ice cover maintains the horizontal gradients of air temperature and water vapor content between polar and temperate latitudes, which is the driving force in the general atmospheric circulation. However, relative humidity is sufficiently high to cause a high percentage of cloud cover in polar regions. During the growth and aging of sea ice, it rejects large quantities of salt into the ocean. A cold, highly saline and therefore, very dense water forms and sinks by vertical convection into the deep ocean called Deep Bottom Water. This cause thermohaline circulation (Comiso et al., 2003).

Sea ice growth begins with the formation of small platelets and needles called frazil. The frazil crystals combined with sea water, a soapy mixture is formed called grease ice. When the freezing continues under quiet conditions, frazil crystal coalesce together and forms solid cover of ice up to 10 cm thickness which behaves elastically and is called nilas. This sea ice cover becomes thicker under favorable cold and quiet conditions and finally reaches the state of first-year ice (FYI) at a thickness of about 30 cm. First year ice is sea ice of not more than one winter growth. Multiyear ice has distinct properties that distinguish it from first-year ice, based on processes that occur during the first summer melt. Multiyear ice contains much less brine and more air pockets than first-year ice.

Sea ice is a heterogeneous mixture of liquid-brine inclusions and air packets scattered within the ice medium. The brine inclusions contain salt and water. Its a high dielectric constant has high imaginary part compared to that of ice. The salinity profile of first-year ice typically decreases from about $5-16\,\text{‰}$ near the surface to about $4-5\,\text{‰}$ in the bulk of the ice and increases rapidly to $30\,\text{‰}$ near the ice-water interface ('C-shape'). In contrast, the salinity of multiyear ice usually is less than $1\,\text{‰}$ in the surface layer and about $2-3\,\text{‰}$ in the bulk portion. These values are representative of sea ice in the Arctic Ocean, where the salinity of liquid water is of the order of $32\,\text{‰}$.

Thus, for first-year ice, the microwave emission comes approximately from the snow/ice interface and is not subject to scattering, except that caused by the snow on the top of the ice. On the other hand, since the radiation emanates from further down for multiyear ice, scattering caused by the presence of air pockets becomes an important factor and cause a reduction in the radiation observed above ice surface (Ulaby et al., 1986). Surface and volume scattering of sea is to be considered. Scattering from a given sample of ice depends on the electromagnetic frequency, polarization and direction of incidence. The most fundamental difference between first-year ice and multiyear ice is the presence of brine in the former and the replacement of the brine by air pockets in the latter in the free board layer. The effect of density of sea ice is twofold: (1) lower density causes less emitting material per layer of ice and (2) low density ice has more air pockets, which act as scatterer. Ultimately low density cause lowering of the measured brightness temperature (Comiso and Kwok, 1996).

2.2 Snow

The snow cover on sea ice plays a central role in exchange of mass and energy across the ocean-sea ice-atmosphere interface (Barber et al., 1998). During winter the snow acts as thermal insulator, decreases heat exchange with ocean and retards freezing. During the summer the high albedo of the snow reduces the short-wave radiation input and slows down the surface melting (Tucker III et al., 1992). The thickness of the snow cover varies both temporally and spatially. Temporally, drastic snow cover changes occur during the summer melt period and early freeze-up. The maximum snow cover thickness is located between the North Pole and the northern parts of Greenland and the Canadian Arctic Archipelago (Warren et al., 1999; Przybylak, 2003) in June (40 – 46 cm). Generally the snow depth over multiyear ice is greater than on first-year ice (Tucker III et al., 1992).

In winter, the snow surface temperature is considerably lower than the ice temperature which in turn is lower than the temperature of water underneath. In summer a positive temperature gradient is ob-

served towards the snow surface (Perovich et al., 1997). Dry snow
consist of ice crystals and air voids. The density of dry snow varies
from $0.1\,\mathrm{g\,cm^{-2}}$ to $0.5\,\mathrm{g\,cm^{-2}}$. The density increases with age due to
metamorphism and melt-freeze cycle (Hallikainen and Winebrenner,
1992). The scattering in snow cover affects the brightness tempera-
ture measurements above 35 GHz. The emission at higher frequen-
cies where the penetration depth is less than the snow thickness is
only sensitive to snow. The typical snow depth is a few centimeters
in the Arctic and dry snow affects the brightness temperature mea-
surements above 30 GHz. Snow with even 1 % water content affects
all microwave frequencies, a value typically reached at temperatures
about 1 °C (Garrity, 1992).

2.3 The Earth's Atmosphere

The atmosphere of a planet is the gaseous envelope surrounding it.
The vertical structure of the atmospheric temperature is used to iden-
tify the atmospheric layers. The atmosphere up to 100 km (homo-
sphere) is divided into four distinct layers: the troposphere (up to
about 15 km), stratosphere (up to about 50 km), mesosphere and ther-
mosphere. The levels separating these layers are referred to as the
tropopause, stratopause, mesopause and thermopause respectively.
Since the planet's atmosphere is in the planet's gravitational field
its density will fall with altitude.

In the troposphere the temperature decreases with height at a typ-
ical lapse rate of $6.5\,\mathrm{K\,km^{-1}}$. It is called the lower atmosphere. Most
of the weather phenomena such as cyclones, fronts, hurricanes, rain,
snow, thunder and lightning occur here (Andrews, 2000). The tropical
tropopause is at about 16 km while it is at about 8 km in the polar
regions. Approximately 90 % of the atmospherics mass is in the tro-
posphere. A notable feature of the stratosphere is that it contains the
major portion of the ozone molecules. In the stratosphere the tem-
perature increases with altitude. Temperature decreases again in the
mesosphere up to about 85 km. A little less than 10 % of atmospheric
mass is in the stratosphere and 0.1 % in the mesosphere and above.
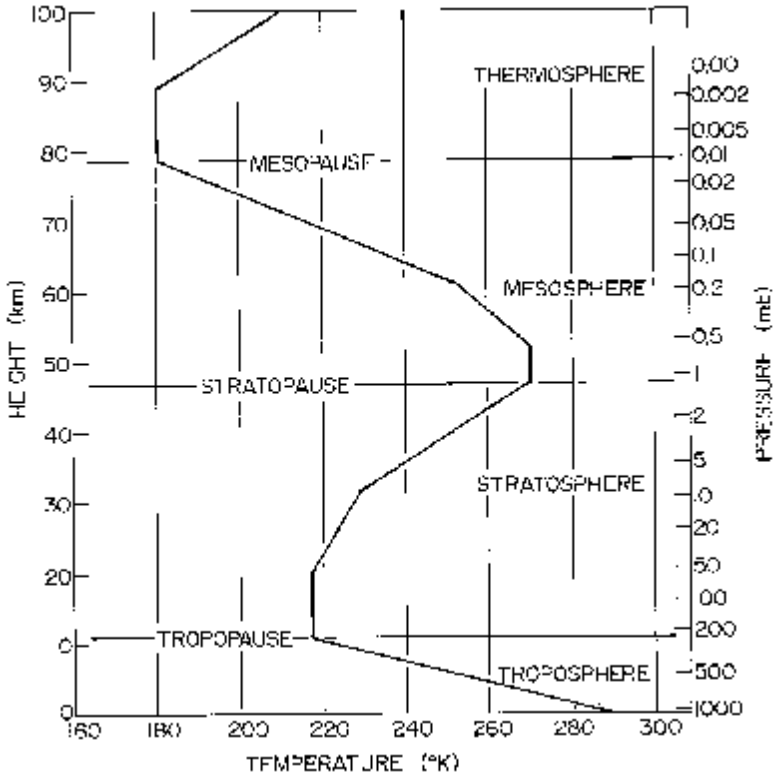
Figure 2.1: Variation of temperature in Earth's atmosphere (Figure courtesy: Houghton (2002)).

The stratosphere and mesosphere together are called the middle atmosphere. The lowest natural terrestrial temperatures are found in the mesopause. There are large variations of the temperature structure of the atmosphere with latitude and season. At the Earth's surface and at the level of the stratopause, the equator is warmer than the polar regions. However, the tropopause and mesopause are colder over the equator than over the polar regions. The summer stratopause is lower and warmer than the winter stratopause and the summer mesopause is extremely cold (Andrews, 2000; Houghton, 2002).

Atmospheric water vapor and ozone play important roles in the tem-

perature of the atmosphere. Since the air temperature in the Arctic troposphere is very low, the water vapor burden is so too. The annual mean total water vapor content in the Arctic atmosphere is around $5 - 7\,\mathrm{kg\,m^{-2}}$ while that of the tropics is around $50\,\mathrm{kg\,m^{-2}}$. At high latitudes, processes such as mid latitude cyclones and anticyclones strongly influence the tropospheric temperature profile.

Temperature inversion is a frequent feature of the Arctic climate: temperature increases with height. The polar inversions are caused by the net negative radiation balance at the surface. It occurs mainly over snow and ice surfaces. The highest inversion frequency occurs in winter $(98 - 99\,\%)$.

2.4 Thermal Radiation

Any idealized material that absorbs all electromagnetic radiation incident upon it and emits electromagnetic radiation with perfect efficiency is called a blackbody. Planck's law states that the specific intensity resulting from the materiel's thermal emission is given by:

$$B_\nu = \frac{2hc^{-2}\nu^3}{\mathrm{e}^{\left(\frac{h\nu}{kT}\right)} - 1} \tag{2.1}$$

where
B_ν : Blackbody spectral brightness $[\,\mathrm{W\,m^{-2}\,sr^{-1}\,Hz^{-1}}]$
h : Planck's constant [J]
ν : Frequency [Hz]
k : Boltzmann constant $[\mathrm{J\,K^{-1}}]$
c : Velocity of light $[\mathrm{m\,s^{-1}}]$
The wavelength corresponding to the maximum in a thermally emitted intensity is determined by differentiating (2.1):

$$\lambda_m T = 2.987\,\mathrm{m^{-3}\,K} \tag{2.2}$$

This is known as Wien's displacement law, and shows that as temperature increases, the intensity maximum shift towards shorter wavelengths. For real materials, the thermal emission will generally be less than that of a blackbody. And the deviation from a blackbody is a

function of frequency (Lubin and Massom, 2006). A real material (gray body) is characterized by its spectral emissivity:

$$\varepsilon_\nu = \frac{I(\nu)}{B_\nu(T)} \tag{2.3}$$

where

ε_ν : the spectral emissivity

$I(\nu)$: Radiation emitted at frequency ν.

Kirchhoff's law states that good absorbers are good emitters, so that absorptivity (a_ν) is equal to emissivity. The absorptivity is defined as the ratio of radiation absorbed at a frequency ν to that incident at a frequency ν. Kirchhoff's law applies when the material is in *local Thermodynamic Equilibrium* (LTE), meaning that thermodynamic temperature applies throughout the volume under consideration. LTE applies to most of the Earth's atmosphere, however, above $100\,\text{km}$ molecular collisions are rare and different gases can have different thermodynamic temperatures.

For Microwaves (centimeter and millimeter waves), $\frac{h\nu}{kT} \ll 1$. So (2.1) can be rewritten as:

$$B_\nu(T) = \frac{2\nu^2 T}{c^2} \tag{2.4}$$

known as Rayleigh-Jeans approximation. Since the the intensity is proportional to the temperature, the convention in microwave remote sensing is to divide the intensity by $2\nu^2 c^{-2}$ to yield the *brightness temperature* (T_b) of the scene being observed, a quantity is much more physically intuitive than unit of intensity. The emissivity (ε) of a material can be defined as the ratio of brightness temperature of the material to the brightness temperature of a black body at the same temperature:

$$\varepsilon(\theta, \nu) = \frac{T_b}{T} \tag{2.5}$$

where T_b is the brightness temperature of the material is that of the black body $(\varepsilon=1)$.

If the height variations of a surface are much smaller than the wavelength of the radiation, such surface is called a smooth or a specular

surface. The following Fresnel equations relate the specular emissivity at horizontal (h) and vertical (v) polarizations to the dielectric constant:

$$\varepsilon_{\mathrm{h}}(\theta, \nu) = 1 - \left| \frac{\mu \cos \theta - \sqrt{\epsilon\mu - \sin^2 \theta}}{\mu \cos \theta + \sqrt{\epsilon\mu - \sin^2 \theta}} \right|^2 \tag{2.6}$$

$$\varepsilon_{\mathrm{v}}(\theta, \nu) = 1 - \left| \frac{\epsilon \cos \theta - \sqrt{\epsilon\mu - \sin^2 \theta}}{\epsilon \cos \theta + \sqrt{\epsilon\mu - \sin^2 \theta}} \right|^2 \tag{2.7}$$

where θ is the local incidence angle, ϵ is the dielectric constant and μ is the relative permeability.
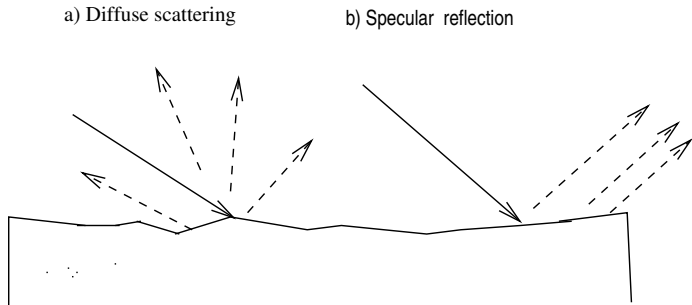
Figure 2.2: Surface scattering: a) diffuse and b) specular.

The primary gaseous absorbers in the troposphere and lower stratosphere for frequencies below 300 GHz are diatomic oxygen (O_2) and water vapor (H_2O). The microwave absorption spectrum of the linear molecule $^{16}O_2$ in the electronic ground state arises from a fine structure transition caused by the interaction of the molecule's permanent magnetic dipole with the magnetic field produced by the electron's orbital angular momentum. Approximately 33 transitions of significant strength in the atmosphere are located between 50 and 70 GHz and an isolated line is located at 118.75 GHz. The microwave absorption spectrum of the asymmetric top $^1H_2{}^{16}O$ is due to rotational transitions induced by the interaction of external fields with molecule's permanent electric-dipole moment. Rotational lines at 22.2 GHz, 183.3 GHz and several lines above 300 GHz are produced by electric interactions with

the incident field. An additional absorption contribution by water vapor takes the form of a 'continuum' that varies slowly with frequency (Janssen, 1993).

The absorption or emission spectrum of a molecule consists of sharply defined frequency lines corresponding to transition between sharply defined energy levels of the molecule. Such a spectrum would be characteristics of an isolated, undisturbed and stationary molecular system. However, the molecules are in constant motion, interacting and colliding with each other and with other material objects. These disturbance cause the energy levels to vary in width, which results in spectral lines with finite broadening called line broadening. There are several reasons for this broadening: *thermal (Doppler) broadening* and *pressure broadening*. Doppler line-broadening results from the random motion of radiating molecules, and therefore depends on temperature. Thermal broadening of typical atmospheric lines is about 10^{-6} times the line frequency. For microwave frequencies pressure broadening is prominent in the stratosphere and and troposphere. Pressure broadening is the perturbation of an absorbing molecule's line spectrum by collision with other molecules. At atmospheric densities, the shape and width of line is proportional to pressure (Ulaby et al., 1981; Mätzler, 2005).

2.4.1 Penetration Depth

The penetration depth of electromagnetic radiation is defined as the distance in which the power density decreases by a factor of e:

$$\frac{P(\delta)}{P(0)} = \frac{1}{e} \tag{2.8}$$

where $P(\delta)$ is the transmitted power at depth δ and $P(0)$ is the transmitted power just beneath the surface.

The complex permittivity of a medium is:

$$\epsilon = \epsilon' - j\epsilon'' \tag{2.9}$$

where ϵ' is the permittivity and ϵ'' the dielectric loss factor (L).

The electric field intensity at the depth z for a plane wave propagating in a lossy medium

$$E(z) = E_0 \, e^{-\gamma z} \tag{2.10}$$

where E_0 is the field intensity at $z = 0$ and

$$\gamma = \alpha + j\beta \tag{2.11}$$

where γ, α and β are the propagation, absorption and phase constant of the medium.

$$\alpha = \frac{2\pi}{\lambda} \epsilon'' \tag{2.12}$$

and

$$\beta = \frac{2\pi}{\lambda} \epsilon' \tag{2.13}$$

where λ is the wavelength.

The penetration depth is:

$$\delta = \frac{\lambda}{4\pi\epsilon''} \tag{2.14}$$

is valid only in a scatter free medium. In order to calculate penetration depth, one requires the dielectric loss factor (ϵ'') of the medium (Ulaby et al., 1986).

Satellite radiometers normally measure radiation, expressed as brightness temperature. In order to extract the needed information from the measured radiation several techniques are used. The emissivity retrieval method is described in Chapter 4 and temperature retrieval method is explained in Chapter 7.

3 Data

Data from remote measurement, in-situ measurements and from model runs are used in this thesis. The data set and radiative transfer model used are described this chapter. Remote sensing data is obtained from the satellite instruments AMSU and AMSR-E described in sections 3.1 and 3.2. Other data sources used are described in the following sections (3.3 to 3.5). Section 3.6 is dedicated to the radiative transfer model MWMOD which is used for the radiative transfer calculations of the emissivity retrieval.

3.1 Advanced Microwave Sounding Unit

Advanced Microwave Sounding Unit (AMSU) is a microwave radiometer. It is on the new generation polar orbiting satellites NOAA-15, NOAA-16 and NOAA-17. AMSU consists of two modules 'A' and 'B'. The frequencies and bandwidth are listed in Table 3.1. Fig. 3.1 shows the zenith opacity of a mid-latitude summer atmosphere for the microwave frequency range. The zenith opacity is the vertically integrated absorption coefficient and can be calculated as:

$$\tau(s) = \int_0^s \alpha(s')\, \mathrm{d}s' \tag{3.1}$$

where τ is the optical depth (which is also called opacity) and α is the absorption coefficient.

The observation scan angles angles of the instruments vary from $-48°$ to $+48°$, there by the local zenith angles (Fig. 3.2) varies in the range of $\pm 50°$. The retrieval of surface emissivity is most accurate for the atmospheric window channels since these measurements are least affected by the atmospheric absorption and emission. The satellite has
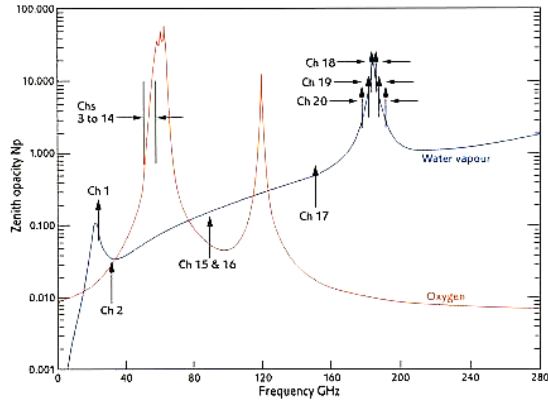
Figure 3.1: Atmospheric zenith opacity due to O_2 and water vapor for the microwave frequency range. The positions of 20 channels of AMSU can also be seen. Low opacity channels are atmospheric window channels (channels 1, 2, 3, 15, 16 and 17).

an orbital inclination of $98°$, and the swath width is around $2068\,\mathrm{km}$. The orbital period is 102 minutes.

Both AMSU-A and AMSU-B have $89\,\mathrm{GHz}$ channels, but with different resolutions.

3.1.1 AMSU-A

The AMSU-A is a temperature sounder. It has 15 channels in the frequency range $23 - 89\,\mathrm{GHz}$. Channels at 23.8, 31.4, 50.3 and $89\,\mathrm{GHz}$ are atmospheric window channels. There are 11 temperature sounding channels between 50 and $60\,\mathrm{GHz}$ in the oxygen band. AMSU-A has an instantaneous field of view (IFOV) of $3.3°$ at half power points. There are 30 measurements on each scan line. The footprint size is $50 \times 50\,\mathrm{km}^2$ for the innermost scan position near nadir and increases to $150 \times 80\,\mathrm{km}^2$ for the outermost scan position from nadir.
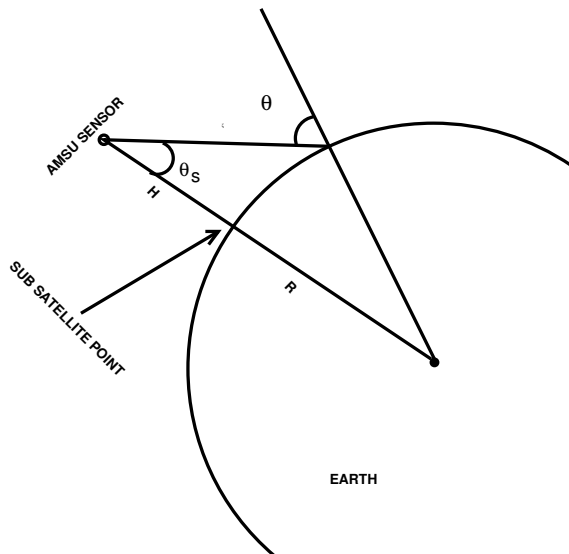
Figure 3.2: The scan angle θ_s and local zenith angle θ of AMSU.

3.1.2 AMSU-B

The AMSU-B is a humidity sounder. It has five channels in the frequency range $89 - 183$ GHz. There are 90 measurements on each scan line. The IFOV of AMSU-B is $1.1°$ (Goodrum et al., 2000). The footprint size varies from 20×16 km^2 for the innermost scan position and increases to 64×27 km^2 for the outermost scan position from nadir. Channels at 89 and 150 GHz are window channels.

3.1.3 AMSU Observations in Polar Regions

Due to the orbital inclination, the high latitude regions (latitudes $> 80°$) are covered only with the right-hand high scan angle portions of the swath (Fig. 3.3). At high scan angle positions, the horizontal resolution is much lower than at the nadir. Both AMSU-A (Weng et al., 2003) and AMSU-B (Buehler et al., 2005) show scan asymmetries. In both the cases it is pronounced in the high scan angle portion. However, the data coverage in polar regions are very high.
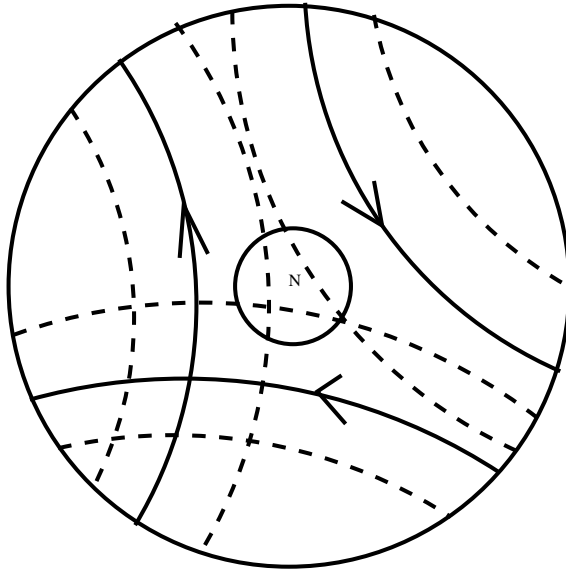
Figure 3.3: Both poles are covered with only high scan angle portion of the swath.

3.2 AMSR-E data

The Advanced Microwave Scanning Radiometer for Earth Observing System (AMSR-E) is on the National Aeronautics and Space Administration's Earth observing System Aqua satellite since May 2002. AMSR-E is a multi-frequency, dual-polarized microwave radiometer that detects faint microwave emissions from the Earth's surface and atmosphere. It measures at six different frequencies in range $6.9 - 89\,\text{GHz}$ in both vertical and horizontal polarizations. It is a conically scanning instrument with an incidence angle of around $55°$. The foot print size varies from $43 \times 75\,\text{km}^2$ for $6.9\,\text{GHz}$ to $3.5 \times 5.9\,\text{km}^2$ for $89\,\text{GHz}$ (JAXA, 2005).

As the footprints at $89\,\text{GHz}$ are rather small, there is a large gap between the scan lines. So there is an additional scan line in between that means there are two feedhornes $0.5°$ difference in off-nadir angle for this channel. The two scan lines are called A-scan and B-scan.

Table 3.1: AMSU channel characteristics

Channel	Frequency [MHz]	Band width [MHz]
1	23 800	270
2	31 400	180
3	50 300	180
4	52 800	400
5	53 596	170
6	54 400	400
7	54 940	400
8	55 500	330
9	$\nu_0 := 57\,290.344$	330
10	$\nu_0 \pm 217$	78
11	$\nu_0 \pm 322.2 \pm 48$	36
12	$\nu_0 \pm 322.2 \pm 22$	16
13	$\nu_0 \pm 322.2 \pm 10$	8
14	$\nu_0 \pm 322.2 \pm 4.5$	3
15	89 000	6000
16	$89\,000 \pm 900$	1000
17	$150\,000 \pm 900$	1000
18	183310 ± 1000	500
19	183310 ± 3000	1000
20	183310 ± 7000	2000

Table 3.2: AMSR-E channels and resolution

Frequency [GHz]	Band Width [MHz] [MHz]	IFOV [km × km]
6.9	350	43 × 75
10.6	100	29 × 51
18.7	200	16 × 27
23.8	400	18 × 32
36.5	1000	8.2 × 14.4
89.0(b)	3000	3.5 × 5.9

3.3 ECMWF Data

The European Center for Medium-Range Weather Forecasts (ECMWF) provides meteorological data such as temperature, pressure, geopotential height, zonal wind, meridional wind, vertical wind, specific humidity, cloud cover, cloud liquid water content and cloud ice water content from their model runs. ECMWF data is in a 1.5° grid having 60 vertical levels. The profiles are available globally every 6 hours (Uppala and others, 2005).

3.4 Polarstern Data

The German research vessel Polarstern makes research cruises every year in the polar region. Radiosonde measurements from Polarstern cruises are one possible source of atmospheric profiles (Koenig-Langlo and Marx, 1997). Cruises are normally in the summer. So measurements over sea ice are very few in number.

3.5 SHEBA Data

To gain a better understanding about the Arctic climate a comprehensive set of surface and atmospheric measurements have been collected in the Arctic during 1997 and 1998 as part of the Surface Heat Budget of the Arctic Ocean (SHEBA) experiment (Moore et al., 2002). In SHEBA the emphasis was on surface processes. It provides year round observation of temperature profiles of ice and snow cover over different kinds of sea ice. The measurements can be used to compare in-situ data with modeling results and to obtain more detailed knowledge about the physical processes in the atmosphere such as cloud microphysics, radiation and boundary-layer turbulence. We have used measurements from two sites, one covered by first-year ice and the other with multiyear ice. Thermistor string observations were conducted to measure the temperature profiles of snow and ice. The first-year ice site is called 'Baltimore' and the mutiyear ice site is called 'Quebec2'.

From Baltimore we obtained 7252 profiles with the vertical resolution
of 10 cm. The snow-sea ice interface is referred as zero height. So we
obtained temperature measurements upto the height of 60 cm and a
depth of 230 cm. From 'Quebec2' site we obtains 7724 temperature
profiles with a vertical resolution of 5 cm. The measurements go upto
a height of 95 cm and depth of 295 cm.

3.6 MWMOD

The radiative transfer model MicroWave radiative transfer MODel
(MWMOD) (Fuhrhop et al., 1997, 1998) is designed to compute bright-
ness temperatures between 1 and 300 GHz, assuming a scatter free
atmosphere and a specular reflecting surface. The input to MWMOD
are vertical profiles of temperature, pressure and humidity. MWMOD
simulation have been compared with other models and observation
and the brightness temperatures are with an error limit of 2 K. It can
be used to model both the downward and upward microwave radiation
over sea ice and open ocean.

4 Emissivity Retrieval Method

Satellites measure radiation that emanates from the Earth's surface and atmosphere. Here we need to retrieve the surface emissivity from the measured radiation. The method used to retrieve surface emissivity from the radiation measured (T_b) by the satellite radiometer is described in section 4.1. The emissivity method is tested over open water where emissivity can be modeled. The validation of retrieval method over open water is described in section 4.2.

4.1 Determination of Emissivity

The total brightness temperature $(T_b(\nu, \theta))$ measured by the satellite can be written as

$$T_b(\nu, \theta) = T_u(\nu, \theta) + \varepsilon(\nu, \theta) \, T_s \mathrm{e}^{-\tau \sec \theta} \\ + (1 - \varepsilon(\nu, \theta)) \, T_d(\nu, \theta) \mathrm{e}^{-\tau \sec \theta} \tag{4.1}$$

where $T_u(\nu, \theta)$ is the up-welling radiation from the atmosphere, T_s is the physical temperature of the surface, ε is the emissivity of the surface, $T_d(\nu, \theta)$ is the down-welling radiation, τ is the total atmospheric opacity and ν and θ are the observing frequency and incidence angle, respectively. Here the cosmic background (T_c) is ignored, which is usually less than $3\,\mathrm{K}$. Eqn. (4.1) can be solved for the emissivity:

$$\varepsilon(\nu, \theta) = \frac{T_b(\nu, \theta) - T_u(\nu, \theta) - T_d(\nu, \theta) \mathrm{e}^{-\tau \sec \theta}}{(T_s \mathrm{e}^{-\tau(0) \sec \theta} - T_d(\nu, \theta) \mathrm{e}^{-\tau \sec \theta})} \tag{4.2}$$

Substituting $\varepsilon = 0$ and $\varepsilon = 1$, Eqn. (4.1) becomes

$$T_b(\varepsilon = 0) = T_u(\nu, \theta) + T_d(\nu, \theta) \mathrm{e}^{-\tau \sec \theta} \tag{4.3}$$

and

$$T_b(\varepsilon = 1) = T_u(\nu, \theta) + T_s e^{-\tau \sec \theta} \tag{4.4}$$

Substituting Eqns. (4.3) and (4.4) to Eqn. (4.2), we obtain

$$\varepsilon(\nu, \theta) = \frac{T_b(\nu, \theta) - T_b(\varepsilon = 0)}{T_b(\varepsilon = 1) - T_b(\varepsilon = 0)} \tag{4.5}$$

Felde and Pickle (1995) and Hong et al. (2003) used this method for the retrieval of land surface emissivity. $T_b(\varepsilon = 0)$ and $T_b(\varepsilon = 1)$ are simulated brightness temperature with $\varepsilon = 0$ and ($\varepsilon = 1$) respectively for a given ν and θ. They are determined from known atmospheric profiles.

In order to simulate $T_b(\varepsilon = 0)$ and $T_b(\varepsilon = 1)$ in Eqn. (4.5) we use the radiative transfer model MWMOD. Due to the scarcity of in-situ measurements of atmospheric parameters such as temperature or humidity data in the selected study region, data from ECMWF model runs are used. ECMWF profiles over sea ice are compared with in-situ measurements and found good agreement (Chapter 8). Emissivities shown in this thesis are calculated from the brightness temperatures measured by AMSU on NOAA-15 and collocated to ECMWF data using a space window of ± 100 km, and a time window of ± 3 hours.

4.1.1 AMSU Emissivities

The AMSU instruments measure in a mixed linear polarization mode. If θ_s is the scan angle between the observation direction and the nadir on the satellite and θ is the local zenith angle on earth, then the surface emissivity ε for AMSU window channels can be written as

$$\varepsilon(\theta) = \varepsilon_v(\theta) \cos^2(\theta_s) + \varepsilon_h(\theta) \sin^2(\theta_s) \tag{4.6}$$

where ε_v and ε_h are the vertically and horizontally polarized surface emissivities, respectively (Weng et al., 2003, 2001). θ_s can be written in terms of θ as

$$\theta_s = \arcsin\left(\frac{R}{R+H}\sin(\theta)\right) \tag{4.7}$$

where R is the radius of the Earth and H is the height of the satellite. Since in general (for plain Fresnel emissivities), ε_v increases with incidence angles while ε_h decreases, this compensates the decreasing of cosine square and the increasing of sine square for low incidence angles. However, at high incidence angles, i.e., near the borders of a swath, the horizontally polarized part of emissivity dominates because of the sine square and causes much variation, usually a decrease. Figure 4.1 shows the viewing angle dependence of the specular emissivity of sea water for the four AMSU-A window frequencies derived using the relations (2.6) and (2.7). The dotted lines represent emissivities at different v polarization and dashed lines represent those at h polarization. Solid lines represent emissivity with AMSU polarization mixing (represented by solid lines) using the relation (4.6). Vertically polarized emissivity first increases with incidence angle till around $60°$ and then decreases. The horizontal emissivity decreases with incidence angle. As the frequency increases the emissivity also increases in the case of sea water. The emissivity with AMSU polarization mixing remains constant up to around $45°$ and then decreases. The dielectric constant of saline water is represented by an equation of Debye form. Equations for the parameters in the Debye expression are function of the water temperature and salinity (Stogryn, 1971).

4.2 Validation of Method over Open Water

In order to validate the emissivity algorithm, retrieved emissivities over open water were compared with modeled emissivities. The microwave emissivity of open water is well known (provided the wind speed and water temperature are known), here we used the state-of-the-art model FASTEM(English and Hewison, 1998). The retrieval has been done for all AMSU-A viewing angles and at all four window channels by collocating the radiosonde profiles from Polarstern and AMSU-A overpasses in time interval of ±3 hours and space interval of $\pm100\,$km. The maximum and minimum wind speed values and the
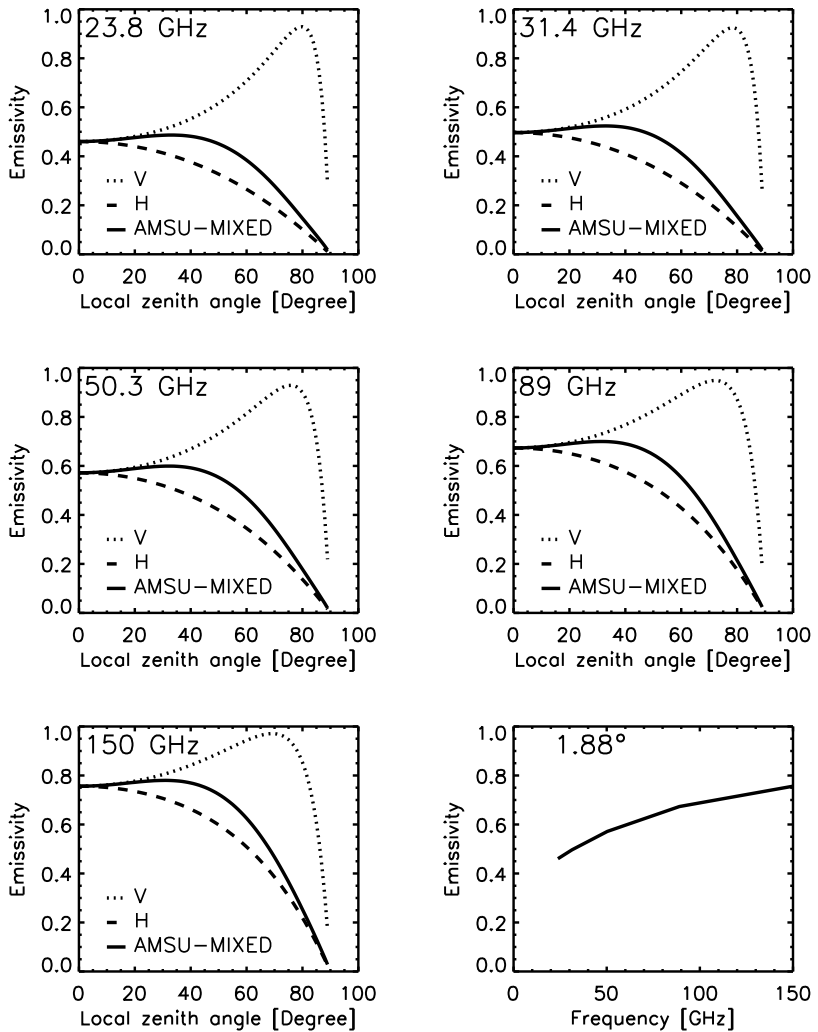
Figure 4.1: The viewing angle dependence of specular emissivity at vertical and horizontal polarizations and (lower right) specular emissivity variation at with frequency for AMSU polarization mixing at mean nadir incidence ($\theta = 1.88°$).

temperatures from the lowest levels of radiosondes (10 m above sea level) are used for modeling. In order to obtain cloud information, synoptic observations concurrent to the radiosonde launches are used. In Figs. 4.2 and 4.3, lines represent emissivities modeled by FASTEM and symbols represent the emissivities retrieved. The solid line is for the lowest wind speed and dashed line for the highest wind speed. Special care has been taken to avoid high emissivity values from measurements over the marginal ice zone.

In the Antarctic, 16 profiles satisfied the conditions of total cloud cover less than 3 oktas (3/8) over open ocean. The profiles are from the cruises in the years 2000–2002. In Fig. 4.2, solid line is for the lowest surface wind of $6.3 \, \mathrm{m \, s^{-1}}$ among the profiles and the corresponding surface temperature (271 K). The dashed lines represent the highest surface wind of $16.8 \, \mathrm{m \, s^{-1}}$ and the corresponding surface temperature (274.7 K).
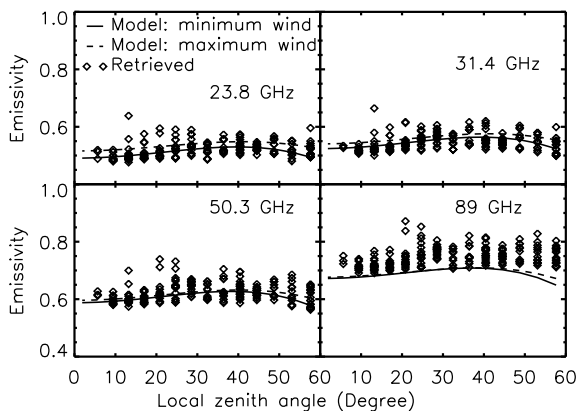
Figure 4.2: Emissivities retrieved from Polarstern radiosonde profiles and modeled using FASTEM over the Antarctic for all AMSU-A window channels.

In the Arctic there were seven test profiles having less than 3 oktas cloud cover. The retrieved emissivity is shown in Fig. 4.3. Here the emissivities modeled are for surface winds of $2.8 \, \mathrm{m \, s^{-1}}$ (solid line) and $28 \, \mathrm{m \, s^{-1}}$ (dashed line) and the corresponding temperatures of 278.7 K and 279 K, respectively.
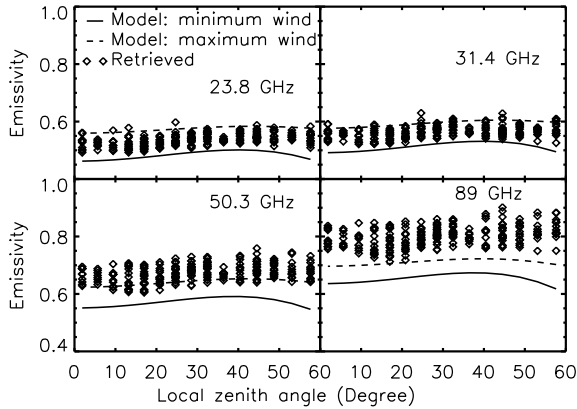
Figure 4.3: Emissivities retrieved from Polarstern radiosonde profiles and modeled using FASTEM over the Arctic for all AMSU-A window channels.

In both the test cases above, the modeling has been done for the two extreme surface winds and the corresponding temperatures in the profiles used. The main factors affecting the ocean surface emissivity are surface wind speed and surface temperature (Wentz, 1983). Over the Antarctic, because of the particular temperature and wind combinations, the modeled emissivities are all similar and the retrieved emissivities are very close to the modeled ones (Fig. 4.2). For the lower frequencies, in the Arctic (Fig. 4.3), the calculated emissivities lie well within the two modeled emissivities. At 89 GHz, the retrieved data seem to have a positive bias. It is the channel that is most sensitive to atmospheric influences, e.g., high water vapor content. Moreover, FASTEM predicts that the effect of wind decreases with frequency.

The retrieval method described in this chapter is used for the retrieval of emissivities from AMSU and AMSR-E data and it is shown in Chapter 6.

5 Surface Temperature Assumptions for the Emissivity Retrieval

5.1 Introduction

Surface emissivity retrieval requires surface temperature information. The radiation at microwave frequencies emanates from a layer of finite depth depending on frequency. In the case of snow covered sea ice, except for the summer months, the snow surface temperature is considerably lower than the ice temperature, which in turn is lower than the temperature of water underneath the ice ($-1.8\,^{\circ}$C). Here, frequencies in the range of $6-150$ GHz are considered for the retrieval of surface emissivity. At lower frequencies such as $6-37$ GHz dry snow is nearly transparent and the radiation can penetrate even sea ice. So to calculate the effective emissivity, the effective temperature (integrated emitting layer thermometric temperature) of the emitting layer is needed. For that, we need to know the dielectric properties and temperature profiles of sea ice and snow. There exists some emission models for sea ice (Tonboe et al., 2006) which models the effective temperature. The accuracy of such models again depends on the accuracy of the input sea ice and snow parameters such as salinity, density and permittivity.

In the present study, a set of regression coefficients is derived by analyzing temperature profiles of snow and ice to correct the lowest level air temperature in order to get the emitting layer temperature. We use a single temperature representative of whole emission. In order to derive the emitting layer temperatures, penetration depths of different frequencies inside snow and ice are considered.

5.2 Penetration Depth and Emission Layer Temperature

Microwave emission from snow covered sea ice can come from the snow and sea ice volume or from the underlying water. However, due to transmission losses and scattering, the intensity of radiation reaching the surface of snow covered sea ice is only from a certain layer. In order to find the layer from which the microwave emission comes from we need to to know the penetration depth. Haggerty and Curry (2001) determined the typical values for the penetration depths for different frequencies by calculating the dielectric loss factor ϵ'' following parameterization for various types of materials given by Ulaby et al. (1986) for frequencies in the range of $37-220\,\mathrm{GHz}$. The penetration depth (δ) at a given wavelength (λ) is calculated according to Equation (2.14).

Table 5.1: Penetration depths [cm] for different surface types at $-10\,^{\circ}\mathrm{C}$ interpolated from Haggerty and Curry (2001).

ν [GHz]	Dry snow	Multiyear ice	First-year ice
23.8	143.35	7.76	1.52
31.4	129.91	7.32	1.45
50.3	96.47	6.23	1.28
89.0	28	4	0.94
150	13	2	0.75

Table 5.1 shows penetration depths of different surface types at AMSU window channels interpolated/extrapolated from Haggerty and Curry (2001). In the case of dry snow, the assumed penetration depth is much higher for low frequencies ($23-50\,\mathrm{GHz}$) compared to the typical arctic snow cover ($<40\,\mathrm{cm}$, Przybylak (2003)). Due to low salinity, multiyear ice shows larger penetration depths than the more saline first-year ice. For all three cases, the penetration depth decreases with frequency.

Penetration depths simulated using the microwave emission model of layered snowpacks (MELMS) for first-year ice and multiyear ice are

shown in the Figure 5.1 for reference (Tonboe et al., 2006), assuming
a snow depth of 20 cm.
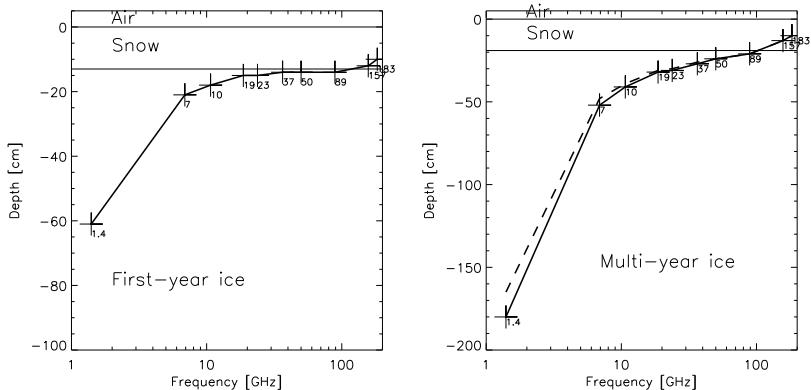
Figure 5.1: The penetration depth for first year ice and multi year ice.
(Figure courtesy: Rasmus Tonboe, DMI.)

The penetration depth varies with temperature as well. However,
that effect is negligible. Here the temperature of the assumed penetra-
tion depth is used as the representative temperature of the emitting
layer. Since the microwave radiation sensed by the satellite comes
from different layers depending on frequency, knowledge of the snow-
ice temperature profile is necessary to predict the apparent surface
temperature (emitting layer temperature) for each frequency (Comiso,
1983). In order to understand the variation of temperature inside snow
and ice measurements from SHEBA are analyzed.

5.3 SHEBA Measurements

A year-round observation of temperature profiles from Surface Heat
Budget of the Arctic Ocean Experiment (SHEBA) at two sites (a first-
year ice site ('Baltimore') and a multiyear ice site ('Quebec2')) are
used to establish a relation between the lowest level air temperature
(snow surface temperature) and the different emitting layer tempera-
tures.
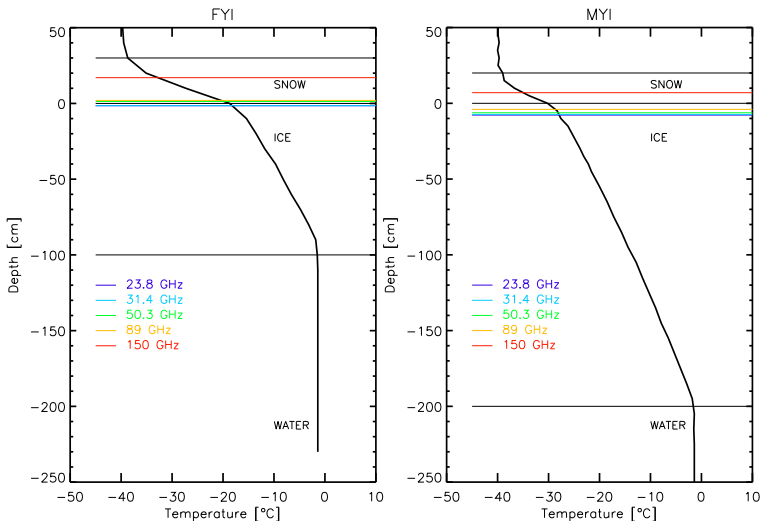
Figure 5.2: Examples of temperature profiles of snow and ice and penetration depths assumed for different frequencies for first-year (left) and multiyear ice (right).

Sample profiles of snow covered first-year ice and snow covered multiyear ice can be seen in Fig. 5.2. The penetration depths assumed for such typical cases for different AMSU frequencies are drawn by horizontal lines. For both first-year ice and multiyear ice profiles, depth '0' on the Y-axis represents the snow-ice interface. In the case of snow covered first-year ice (left panel), horizontal line at depth 30 cm represents the snow-air interface and that at depth -100 cm represents the ice-water interface (the sea ice thickness is 1 m). For multiyear ice (right panel), the snow-ice interface is at 20 cm and ice-water interface is at -200 cm depth (sea ice thickness is 2 m). In both the cases the air temperature is at around $-40\,^{\circ}$C and the underlying water temperature is at $-1.8\,^{\circ}$C. Stronger temperature gradient in snow than in ice can be noticed in both cases. In the case of first year-ice, 30 cm of snow caused a gradient in temperature of around $20\,^{\circ}$C and in the case of multiyear ice, the 20 cm snow cover caused a gradient in temperature of around $10\,^{\circ}$C.

In total 7252 temperature profiles from 'Baltimore' and 7724 from 'Quebec2' have been used in the subsequently described procedure.

5.4 Temperature Correction at AMSU Frequencies

SHEBA temperature profiles for different months of comparable snow depth and having similar temperature profile inside snow and ice are grouped together. When the snow depth is less than penetration depth, as in the case of low frequencies (23.8, 31.4 and 50.3 GHz), snow is assumed to be transparent. In such cases penetration depth inside ice is considered. During the summer months, first year ice melts and multiyear doesn't show temperature gradient inside snow and ice. In that case the lowest level air temperature without correction is assumed as temperature of the 'principal emitting layer'. Variation in snow depth, snow wetness and grain size can cause variation in penetration depth and hence emissivity especially, at high frequencies.

A linear relationship exists between the lowest level air temperature (snow surface temperature) and the temperature of the assumed emitting layer.

We will relate the temperatures of the emitting layers to the lowest layer air temperature according to the regression equation:

$$T_{\mathrm{emitting}} = aT_{\mathrm{air}} + b \qquad (5.1)$$

A set of coefficients a and b is derived from the linear relationship between the lowest level air temperature (T_{air}) and the emitting layer temperature (T_{emitting}) at different frequencies for sea ice. The derived regression coefficients can be used to correct the lowest air temperature to get emitting layer temperature of sea ice for different frequencies later. The regression coefficients a and b are derived for for first-year ice and multiyear ice separately.
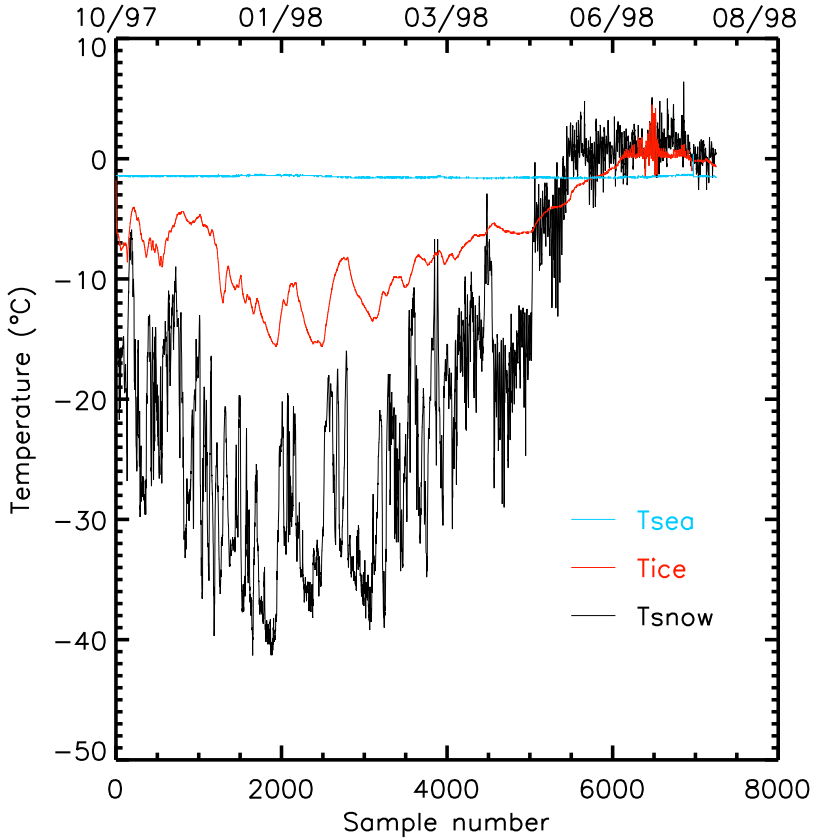
Figure 5.3: Variation of temperature for different months for snow covered sea ice: on the top of water (T_{sea}, constant), sea ice (T_{ice}, smooth) and snow (T_{snow}, noisy) (from SHEBA data). T_{snow} is the lowest level air temperature as well.

5.4.1 First-year Ice

Figure 5.3 gives the variation of temperature over water, sea ice and snow (air temperature) during the SHEBA measurement campaign for the first-year ice site 'Baltimore'. On the upper X-axis of the figure, both the month and year of the sample measurements are noted. Large difference between air temperature and water temperature during winter months is a noticeable feature of the figure. The temperature of the water underneath remains constant at $-1.8\,^\circ$C throughout the measurements. During summer months the air temperature becomes a few degrees above the freezing temperature.

Table 5.2: Slope (a) and Y-intercept (b) used to regress the emitting layer temperature of first-year ice from the lowest level air temperature. DJFM represents the months December to March and AMASON represents the months April, May, August, September, October and November.

ν [GHz]	Months	a	b [K]	rms error [K]
23.8		0.29	-4.97	1.58
31.4		0.29	-4.96	1.58
50.3	DJFM	0.30	-4.95	1.58
89.0		0.38	-4.27	1.53
150.0		0.82	-0.12	1.39
23.8		0.36	-2.94	1.12
31.4		0.36	2.93	1.12
50.3	AMASON	0.37	-2.91	1.12
89.0		0.37	-2.88	1.12
150.0		0.38	-2.86	1.12

Figs. 5.4 and 5.5 present the scatter plots of emitting layer temperatures assumed for different frequencies plotted against the lowest level air temperatures for the winter months December to March and for the months April, May, August, September, October and November respectively. The emitting layer temperature of the highest frequency (150 GHz) shows better correlation to the lowest level air temperature. The least penetration depth assumed is for this frequency. Emitting

23.8 GHz

$T_{emitting\ layer}$ [° C]

T_{air} [° C]

y=ax+b
a= 0.299
b=−4.970

31.4 GHz

a= 0.300
b=−4.963

50.3 GHz

a= 0.302
b=−4.948

89 GHz

a= 0.376
b=−4.267

150 GHz

a= 0.817
b=−0.121

Error

23 GHz: 1.583 K
31 GHz: 1.583 K
50 GHz: 1.583 K
89 GHz: 1.535 K
150 GHz: 1.392 K

Figure 5.4: Correlation between emitting layer temperature and air temperature for the months December to March. Error in the bottom right panel is the root mean square deviation of the points from the fit.

Figure 5.5: Correlation between emitting layer temperature and air temperature for the months April, May, August, September, October and November. Error in the bottom right panel is the root mean square deviation of the points from the fit.
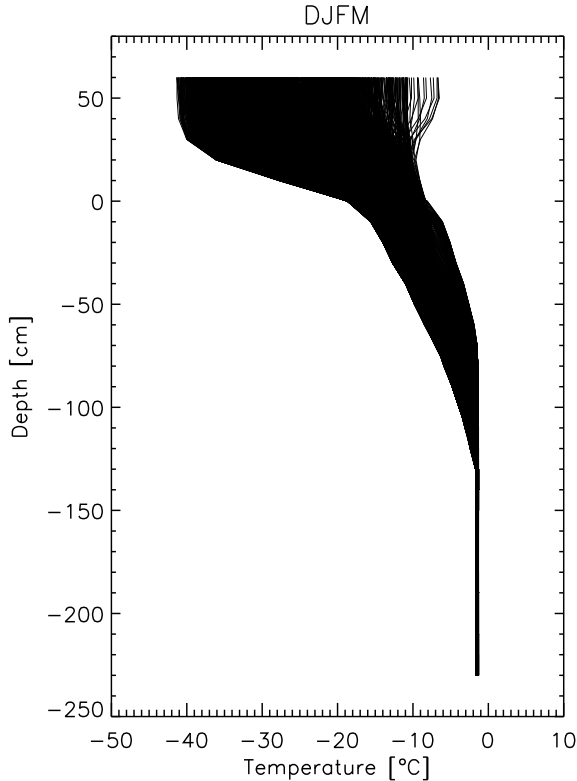
Figure 5.6: All 2904 ice profiles used to derive the correlation between the emitting layer temperature and air temperature for the months December to March. Sow-ice interface at depth 0.

layer temperatures of lower frequencies $(23 - 50 \, \text{GHz})$ show similar correlations with lowest level air temperatures. The penetration depth assumed is also similar at these frequencies.

Figure 5.6 shows all the 2904 profiles for the months December to March used in the scatter plots of Fig. 5.4. The spread of air temperatures (snow surface temperatures) is around $36 \, ^\circ\text{C}$ $(-42 \, ^\circ\text{C}$ to $-7 \, ^\circ\text{C})$, however the sea ice surface temperature spread is only around $10 \, ^\circ\text{C}$ $(-19 \, ^\circ\text{C}$ to $-11 \, ^\circ\text{C})$. The sea ice thickness varies from around $130 \, \text{cm}$ to around $70 \, \text{cm}$.

Table 5.2 summarizes the regression coefficients derived to deter-

mine the emitting layer temperature from the air temperature and the root mean square deviation from the regression line (rms error) over first-year ice regions for the months December to March (DJFM) and for April, May, August, September, October and November (AMASON). For the months June and July the lowest level air temperature is assumed as the surface temperature. The rms deviation (σ) is calculated using the equation:

$$\sigma = \sqrt{\frac{1}{n}\sum_{i=1}^{n}(y - x_i)^2} \tag{5.2}$$

$x_1, x_2, \ldots, x_n$ are the n points on the scatter plot.

5.4.2 Multiyear Ice

Table 5.3: Slope (a) and Y-intercept (b) used to regress the emitting layer temperature of multiyear ice from the lowest level air temperature. DJFM represents the months December to March and AMSON represents the months April, May, September, October and November.

ν [GHz]	Months	a	b[K]	rms error [K]
23.8		0.45	−9.01	2.47
31.4		0.46	−8.97	2.46
50.3	DJFM	0.46	−8.86	2.44
89.0		0.49	−8.41	2.37
150.0		0.81	−3.23	1.38
23.8		0.42	−3.86	2.21
31.4		0.42	−3.64	2.21
50.3	AMSON	0.43	−3.80	2.11
89.0		0.45	−3.67	2.06
150.0		0.48	−3.49	1.98

Figs. 5.7 and 5.8 present the scatter plots of emitting layer temperatures plotted against the lowest level air temperatures for the winter months December to March and for the months April, May, Septem-
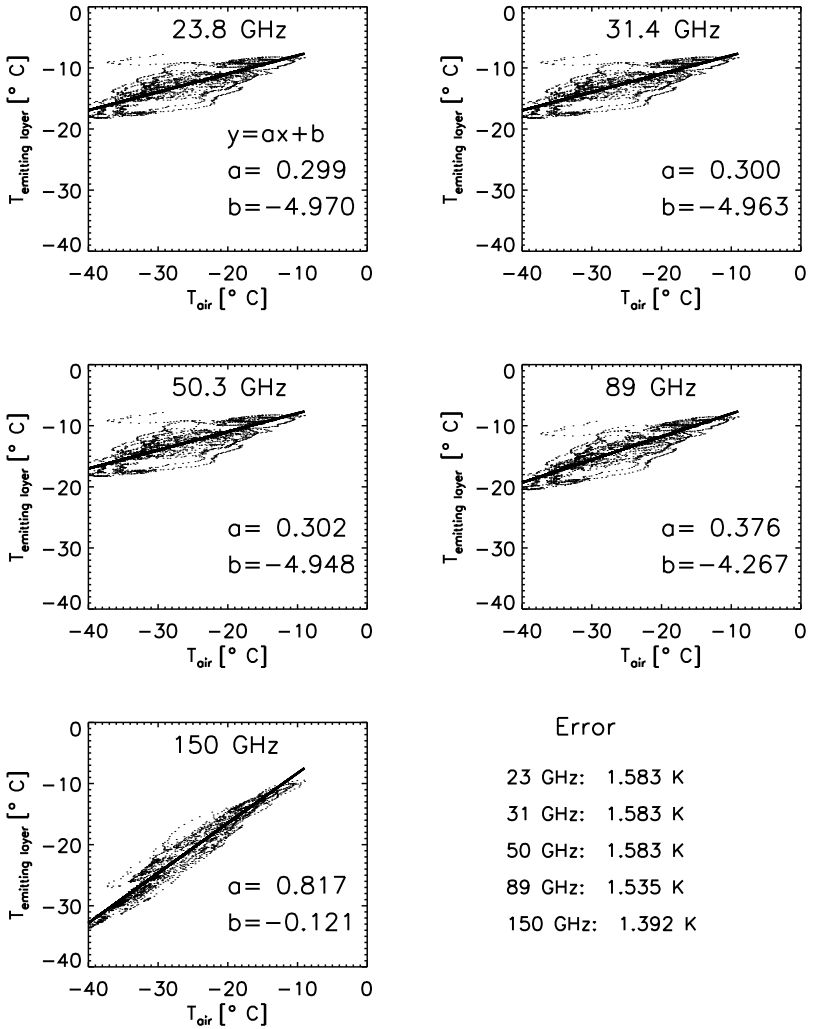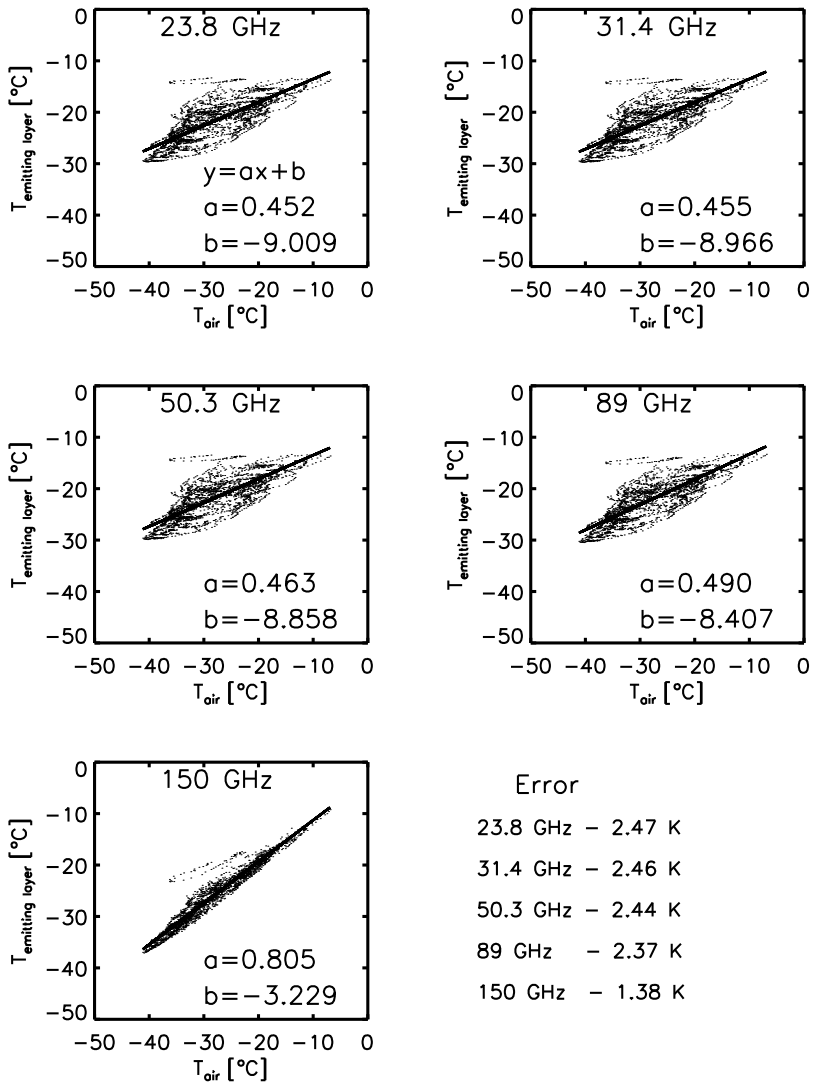
Figure 5.7: Correlation between emitting layer temperature and air temperature for the months December to March for multiyear ice. Error in the bottom right panel is the root mean square deviation of the points from the fit.
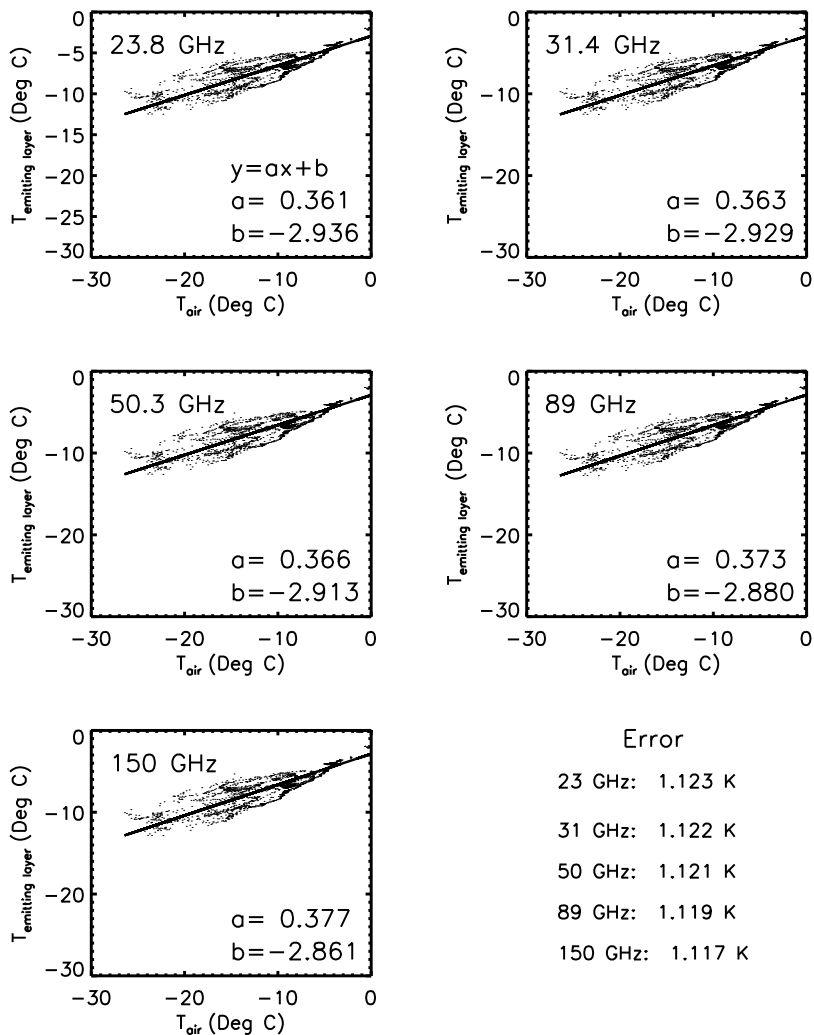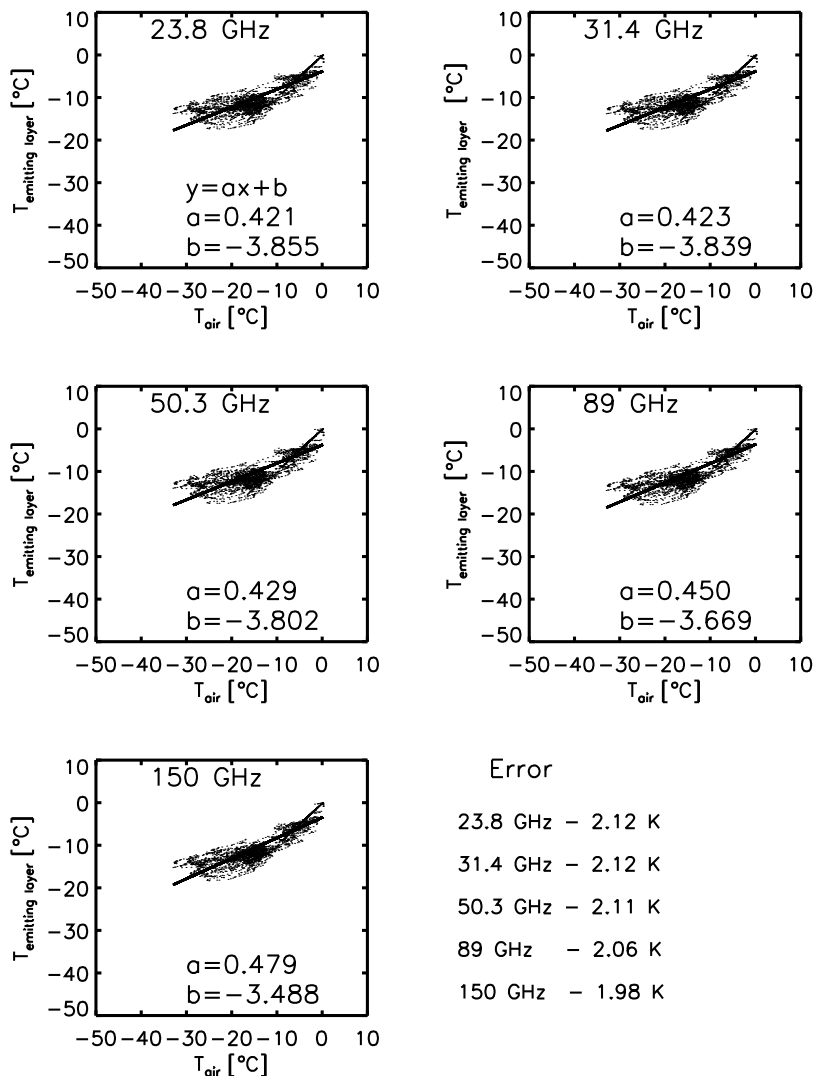
Figure 5.8: Correlation between emitting layer temperature and air temperature for the months April, May, September, October and November for multiyear ice. Error in the bottom right panel is the root mean square deviation of the points from the fit.

ber, October and November respectively for the multiyear ice. Table 5.3 gives the regression coefficients and rms error. For the months June, July and August the lowest level air temperature is assumed as the surface temperature. These rms errors in the emitting layer temperature are caused by the variation in ice thickness and by the variation of air temperature. For example ice thickness varies from 130 cm to 70 cm and air temperature varies from $-10\,^{\circ}$C to $-40\,^{\circ}$C for months December to March (from Fig. 5.6).

5.5 AMSR-E Frequencies

The relation of emitting layer temperature to the lowest level air temperature has also been analyzed at AMSR-E frequencies as described above for AMSU frequencies. Table 5.4 and 5.5 show the regression coefficients derived from the linear relationship between the air temperature and the emitting layer temperature.

The regression is applied to the lowest level air temperatures from the ECMWF for the calculation of surface emissivities with the assumption that the principal contribution to the radiation measured by the satellite instrument is from the indicated penetration depth (principal emitting layer) and the statistics of thickness and air temperature of first-year ice and multiyear ice are the same at test retrieval sites and at SHEBA measurement sites.

These values of regression coefficients derived here are typical for the Arctic first-year ice and multiyear ice respectively and therefore may be transferred to the retrieval described in the next chapter.

Table 5.4: Slope (a) and Y-intercept (b) used to regress the emitting layer
temperature of first-year ice from the lowest level air temperature at AMSR-
E frequencies. DJFM represents the months December to March and AMASON
represents the months April, May, August, September, October and Novem-
ber.

ν [GHz]	Months	a	b [K]	rms error [K]
6.9		0.23	-5.5	1.6
10.6		0.26	-5.2	1.6
18.7	DJFM	0.29	-5.0	1.6
23.8		0.29	-4.9	1.6
36.5		0.30	-4.9	1.6
89.0		0.37	-4.2	1.5
6.9		0.24	-3.5	1.1
10.6		0.29	-3.2	1.1
18.7	AMASON	0.35	-2.9	1.1
23.8		0.35	-2.9	1.1
36.5		0.36	-2.9	1.1
89.0		0.37	-2.8	1.1

Table 5.5: Slope (a) and Y-intercept (b) used to regress the emitting layer temperature of first-year ice from the lowest level air temperature at AMSR-E frequencies. DJFM represents the months December to March and AMSON represents the months April, May, August, September, October and November.

ν [GHz]	Months	a	b [K]	rms error [K]
6.9		0.27	-11.5	2.6
10.6		0.34	-10.5	2.6
18.7	DJFM	0.42	-9.5	2.5
23.8		0.43	-9.2	2.5
36.5		0.45	-8.9	2.4
89.0		0.49	-8.4	2.3
6.9		0.23	-4.5	2.2
10.6		0.26	-4.2	2.2
18.7	AMSON	0.29	-3.9	2.1
23.8		0.29	-3.9	2.1
36.5		0.30	-3.8	2.1
89.0		0.37	-3.6	2.0

6 Retrieved Surface Emissivities

The surface emissivity of sea ice calculated using the data obtained from the passive microwave instruments AMSU on NOAA-15 satellite and AMSR-E on Aqua satellite are presented here.

6.1 AMSU Emissivities

The results shown in this section are derived using the data from the passive microwave sounding instruments AMSU-A and AMSU-B on NOAA-15 satellite collocated to the ECMWF data for the year 2005. Collocations are done in a time window of ± 3 hours and a space window of ± 100 km. The data obtained from AMSU on NOAA-15 suffer from the scan asymmetry and radio frequency interference. However, errors introduced by both of them are ignored here. The retrieval method used is explained in chapter 4 and the surface temperature assumptions are explained in detail in chapter 5.

The $T_b(\nu, \theta)$ in (4.5) is the AMSU measured brightness temperature, $T_b(\varepsilon = 0)$ and $T_b(\varepsilon = 1)$ are the simulated brightness temperatures with surface emissivity zero ($\varepsilon = 0$) and one ($\varepsilon = 1$), which are simulated using microwave radiative transfer model MWMOD using the atmospheric profiles of temperature, pressure and humidity obtained from ECMWF model run as input.

Two sample regions are selected to study the variation of emissivity. A small region selected in the Kara sea (76.5°N to 78°N and 77°E to 79°N), which is usually covered with first year ice (area FYI) during the Arctic winter months. The other region of interest is a small region in the north of Greenland (84°N to 85.5°N and 31.5°W to 36°W), covered with multiyear ice (area MYI). The results presented in the

next sections are from the emissivity retrieved from these two test regions. The positions of the test regions are marked on the Figure 6.1. The two regions selected for study are only two representative regions. Other sea ice covered regions can be different from those for parameters such as concentration of different ice types, water, ice thickness, salinity and snow cover. In principle each region should be treated separately.
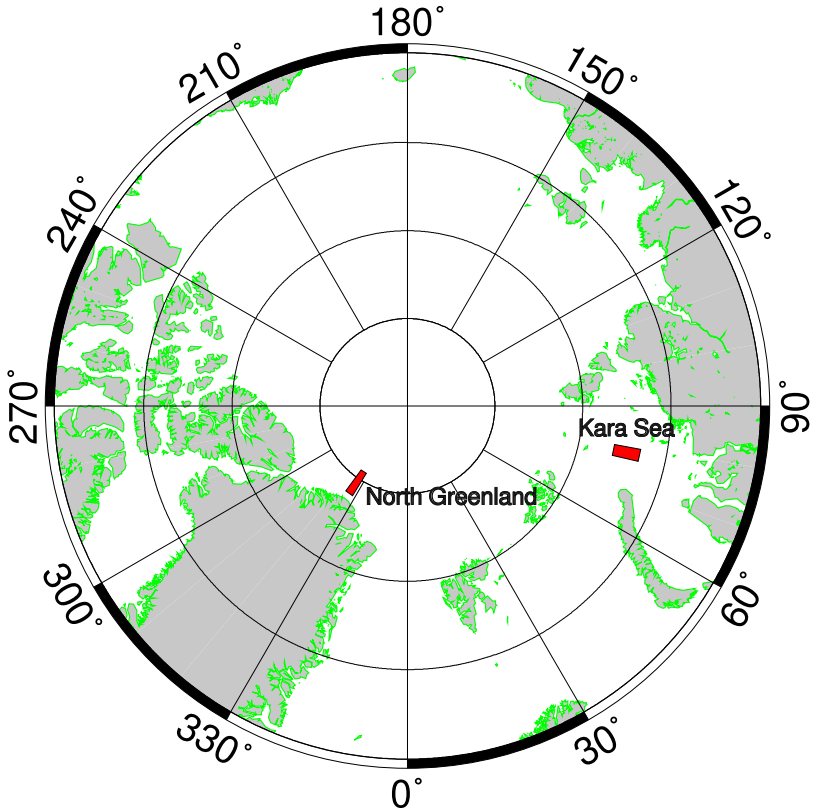
Figure 6.1: Positions of the test regions selected to study first-year ice emissivity (Kara sea) and multiyear ice emissivity (North of Greenland).

The emissivity variation with incidence angle, season and frequency are studied and are presented in sections 6.1.1, 6.1.3 and 6.1.2, respec-

tively. The results are compared with emissivity values in the literature and it is presented in section 6.1.4. Section 6.1.5 presents the emissivity maps. Sections 6.3 presents over all summary of emissivity retrieval.

6.1.1 Zenith Angle Variation of Surface Emissivity

The AMSU instruments measure in a mixed linear polarization mode according to Equation (4.6). Since in general (for plain Fresnel emissivities), ε_v increases with incidence angles while ε_h decreases, this compensates the decreasing of cosine square and the increasing of sine square for low incidence angles. However, at high incidence angles, i.e., near the borders of a swath, the horizontally polarized part of emissivity dominates because of the sine square and causes much variation usually a decrease.

The angular variation of the surface emissivity is shown for the two test regions in the Arctic. Figures 6.2 and 6.3 show the angular variation of the averaged emissivity of different months for the year 2005 for the area FYI and the area MYI, respectively. Different lines represent different window frequencies of AMSU. In the Kara sea region, from July to October there was no ice and the emissivity of those months is not plotted. For all frequencies and months the emissivity variation with local zenith angle is negligible till 45° and the emissivity decreases at high angles as explained above.

The sensitivity to atmospheric parameters increases with frequency, with the highest sensitivity at 150 GHz and so does the observed variability. The variability (standard deviation) of emissivity during the whole month is indicated by error bars. During the summer months, when the surface of the multiyear ice melts, the variability is higher as well (see months June, July and August in Figure 6.3). Change in sea ice concentration, snow and ice temperature variation, snow depth, snow wetness, snow grain size are contributing to the emissivity variability.

Figure 6.2: Angular variation of monthly averages of first-year ice emissivities for different months of 2005. Top left: January ('200501'), bottom right: December ('200512'); July to October excluded (no ice). 89 GHz and 89(b) GHz represent emissivities at 89 GHz channels of AMSU-A and AMSU-B respectively.
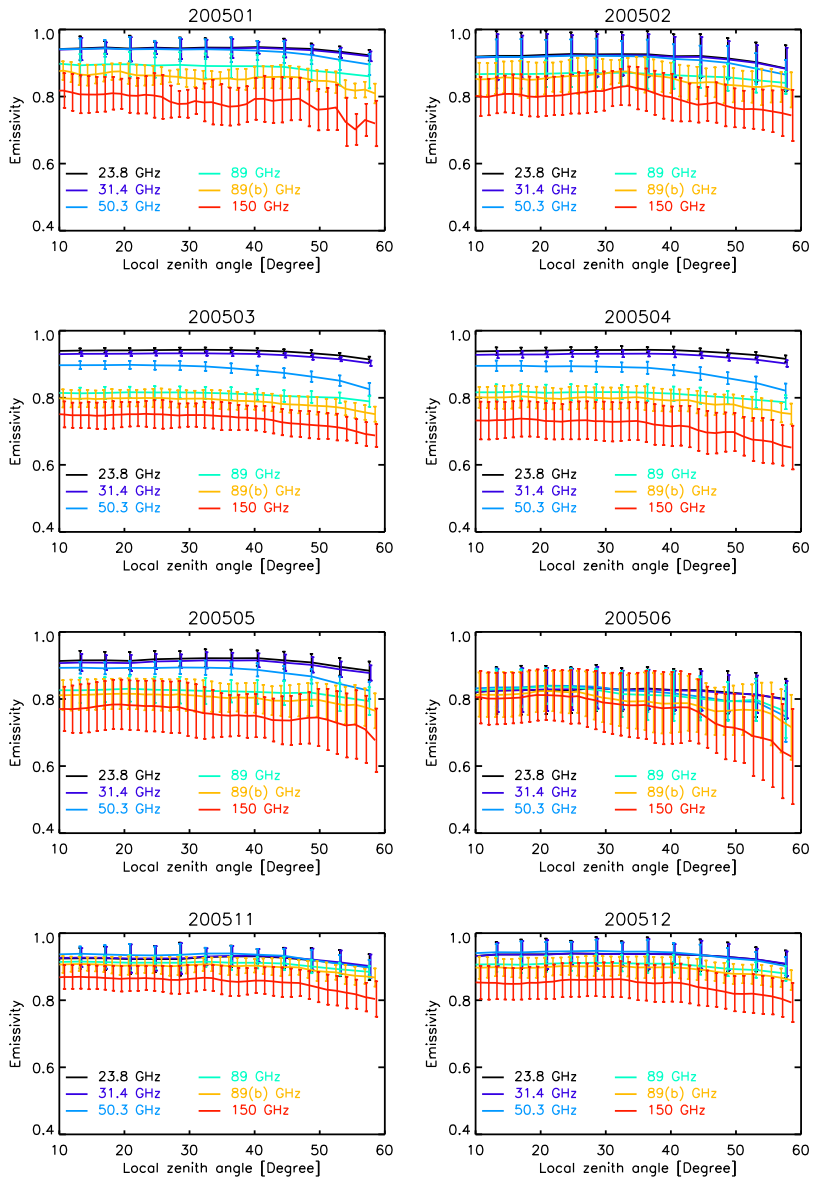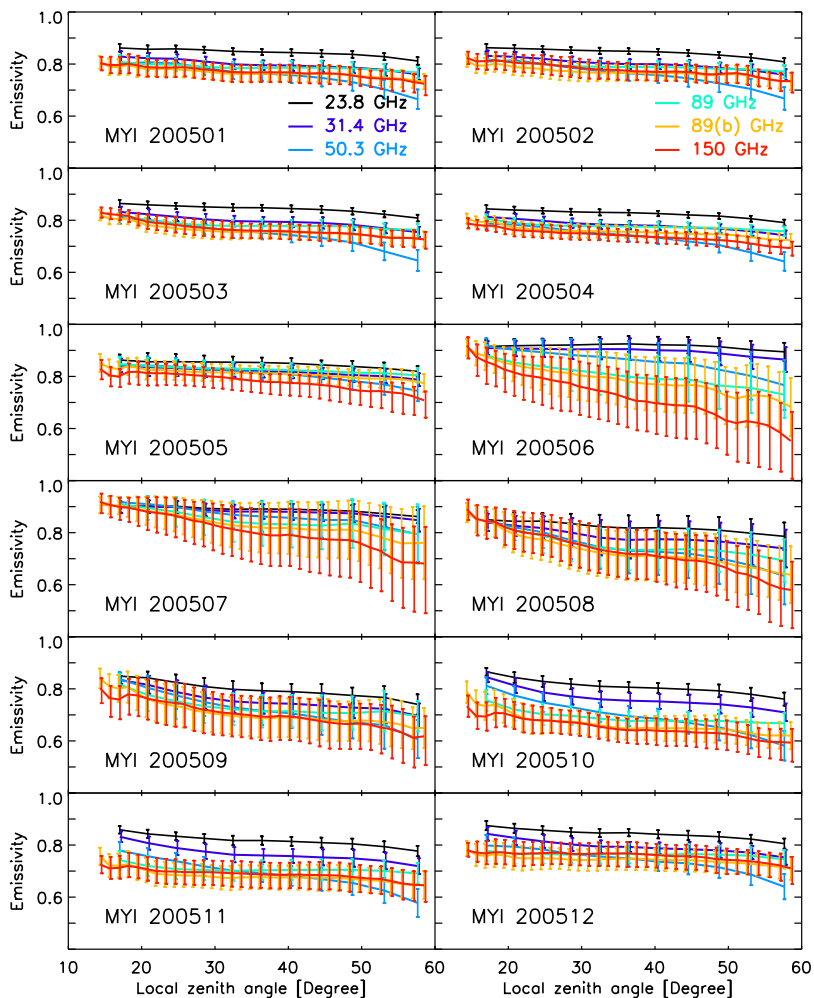
Figure 6.3: Angular variation of monthly averages of multiyear ice emissivities for different months of 2005. Top left: January ('MYI 200501'), bottom right: December ('MYI 200512'). 89 GHz and 89(b) GHz represent emissivities at 89 GHz channels of AMSU-A and AMSU-B respectively.

6.1.2 Seasonal Variation

The seasonal variation of the surface emissivity is studied in the two selected regions in the Arctic. Figure 6.4 shows the seasonal variation of emissivity for all amsu window channels in the area FYI for a local zenith angle of 1.9°. As found in the previous section, it is representative for incidence angles up to 45°. Different solid lines represent different frequencies. The dashed line represents the ice concentration of the region calculated from Special Sensor Microwave Imager (ssm/i) data using the ARTIST Sea Ice (ASI) algorithm Kaleschke et al. (2001). It varies between 0.9 and 0.96 between November and May and drops near zero between July and October. The dash-dotted line represents the average lowest level air temperature from ecmwf. They vary between -12 and -20 °C from November to April and are near melting point from June to September. Overall, the emissivities decrease slightly from November to May. From June to August there is a transition to the emissivities of open water. As the frequency increases, the drop of emissivity during the melting phase becomes smaller and at 150 GHz its no more observed. Similar results were observed by Selbach Selbach et al. (2003) at 157 GHz.

   Figure 6.5 shows the seasonal variation of emissivity for all amsu window channels in the area myi for local zenith angle of 20°. This incidence angle instead of 1.9° as in the case of first-year ice had to be chosen because the high latitudes of the multiyear ice test region are not covered by the central part of the swath but only by the outer parts. However, the change in emissivity with incidence angles below 45° is smaller than the variability within one month (Fig. 6.3). Again the dashed line in Fig. 6.5 represents the ice concentration of the region and the dash-dotted line represents the average lowest level air temperature from ecmwf. During the freezing season, the emissivities vary between 0.75 (150 GHz) and 0.85 (23 GHz). During the summer months the multiyear emissivity goes up to values around 0.9 for all frequencies, peaking in June and then decreasing to about mean winter value as Comiso Comiso (1983) has observed for the smmr frequencies (6.6 – 37 GHz).
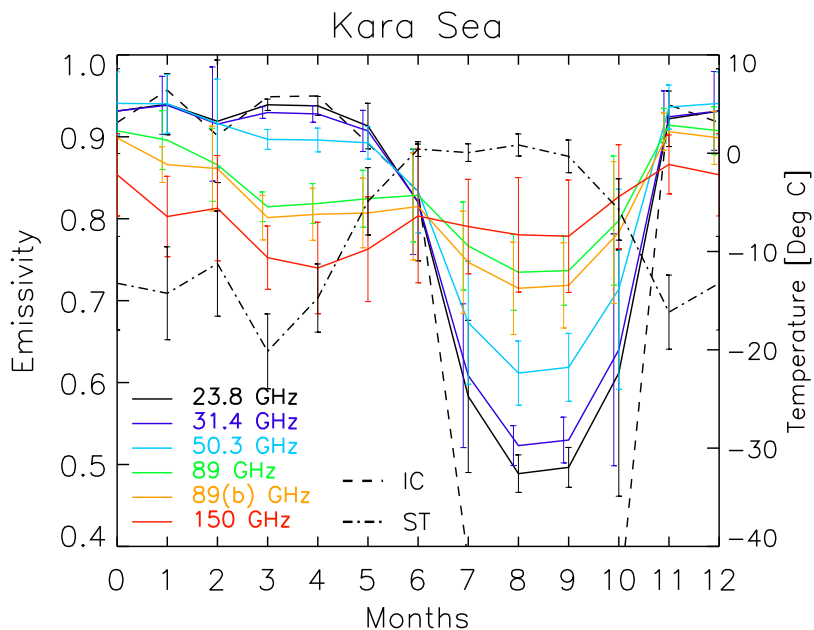
Figure 6.4: Seasonal variation of emissivity at 1.9° incidence angle for the year 2005 in the Kara sea region covered by first-year ice. Dashed line represents the ice concentration (IC) and dashed-dotted line represents the average lowest layer air temperature (ST). 89 GHz and 89(b) GHz represent emissivities at 89 GHz channels of AMSU-A and AMSU-B respectively.

6.1.3 Frequency Variation

Figure 6.6 shows the frequency variation of emissivities for both the area FYI and MYI at a local zenith angle of 20°. The solid lines represent the variation of emissivities for the area FYI and the dotted lines represent the same for the area MYI. During the months November and December the emissivity of the FYI area is high (> 0.86) and nearly constant with a slight decrease towards higher frequencies. The decrease becomes more prominent from January to April when the snow cover increases gradually. When the sea ice is covered with snow, high frequencies (89 GHz and 150 GHz) see only snow and not sea ice and the volume scattering (which reduces emissivity) in snow is strongHallikainen and Winebrenner (1992). In June the emis-
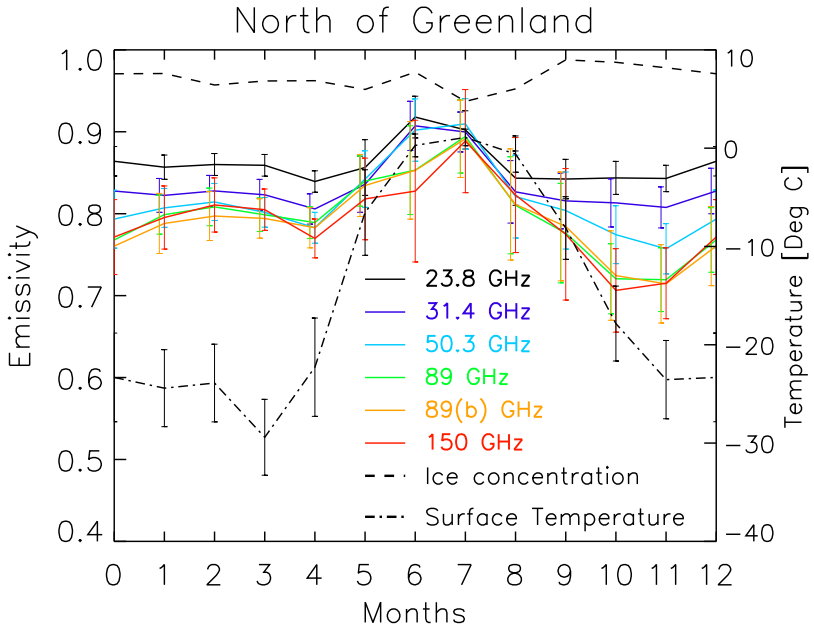
Figure 6.5: Seasonal variation of emissivity at 20° incidence angle in the region in the north of Greenland covered by multiyear ice. Dashed line represents the ice concentration and dashed-dotted line represents the average lowest layer air temperature. 89 GHz and 89(b) GHz represent emissivities at 89 GHz channels of AMSU-A and AMSU-B respectively.

sivity is a mixture of open water and sea ice. From July to October the ice melts and the frequency dependence of open water emissivity is observed. Emissivities of open water modeled at a temperature of 0 °C and salinity of 33 ‰ assuming specular reflection (Stogryn, 1971) are plotted for the months July, August and September (dash-dotted lines in Fig. 6.6). The multiyear ice emissivities are nearly constant around 0.8 during the winter months November to May with slightly higher values at the lowest frequency 23.8 GHz. In June those at 23.8, 31.4 and 50.3 GHz increase to about 0.9 and in July the emissivities at 89 and 150 GHz do similar. From July to October the frequency dependence returns continuously to the winter characteristics.
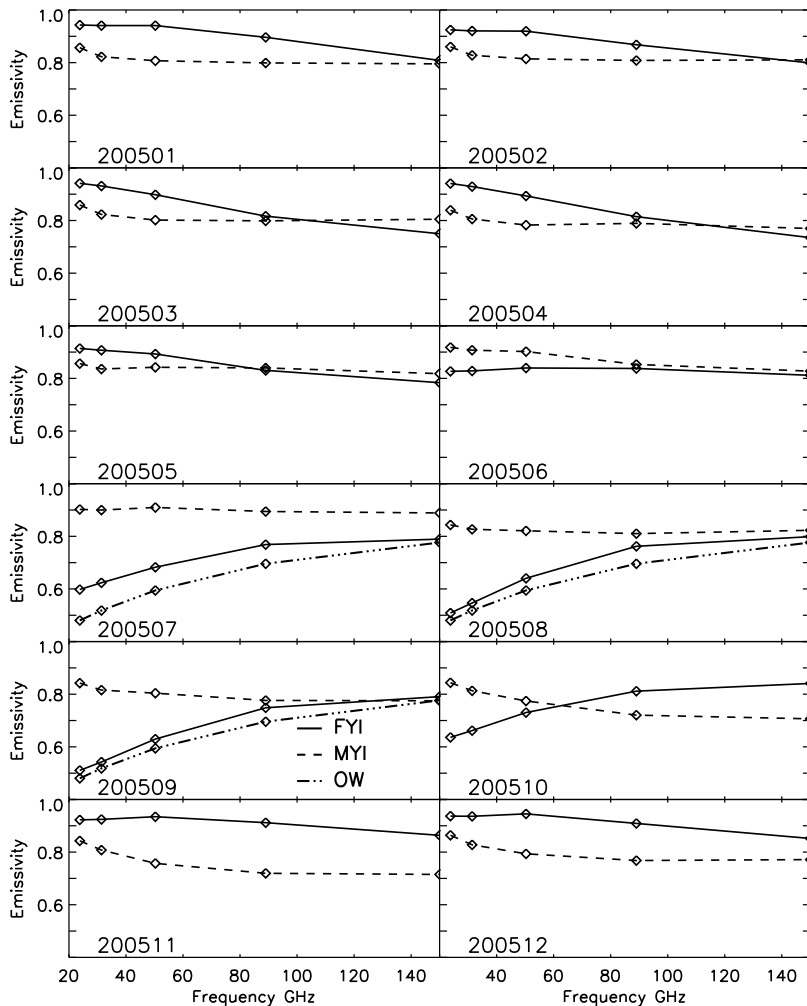
Figure 6.6: Frequency variations of emissivities of test regions in Kara sea and in the north of Greenland from January 2005 (top left, '200501') to December 2005 (bottom right, '200512').

6.1.4 Comparison with Literature Values

Figure 6.7 compares emissivities retrieved for the month November to those from the literature Eppler et al. (1992). The emissivities of first-year ice and dry multiyear ice at 21, 37 and 90 GHz at zenith angle of 50° given for vertical and horizontal polarizations are combined by Eqn. 4.6 to get AMSU-like mixed polarization and are then compared with the retrieved emissivities at similar zenith angle (scan position 28, i.e. $\theta = 48.7°$). For first-year ice the retrievals match well with the literature values. For multiyear ice, even though the frequency variation of both the emissivities is slightly different, the retrieved and literature values are well within their mutual standard deviations. More surface-based measurements of long term evolution of first-year ice and multiyear ice, over the complete yearly cycle are required for the validation of the satellite retrieved emissivities at different frequencies and seasons.

6.1.5 Emissivity Maps

Emissivity maps give us an idea about the spatial variability of emissivity. Figure 6.8 is a one day average emissivity map of 2005/03/15 at 23.8 GHz at resolution of 0.5°. All AMSU overpasses matching in time and space criteria are used for the map irrespective of the local zenith angles. From the map, it is possible to distinguish different surfaces, e.g., low emissivity region as open ocean, high emissivity regions as land and the moderate emissivity region as sea ice. Note that for the emissivity calculations here, the lowest air temperature is used as the surface temperature without any correction even over sea ice. So the errors due to wrong assumption of surface temperature caused unphysical values (> 1.0) of emissivity over a small region in the Kara sea. Figure 6.9 is a one day average emissivity map of 2005/03/15 at 89 GHz.
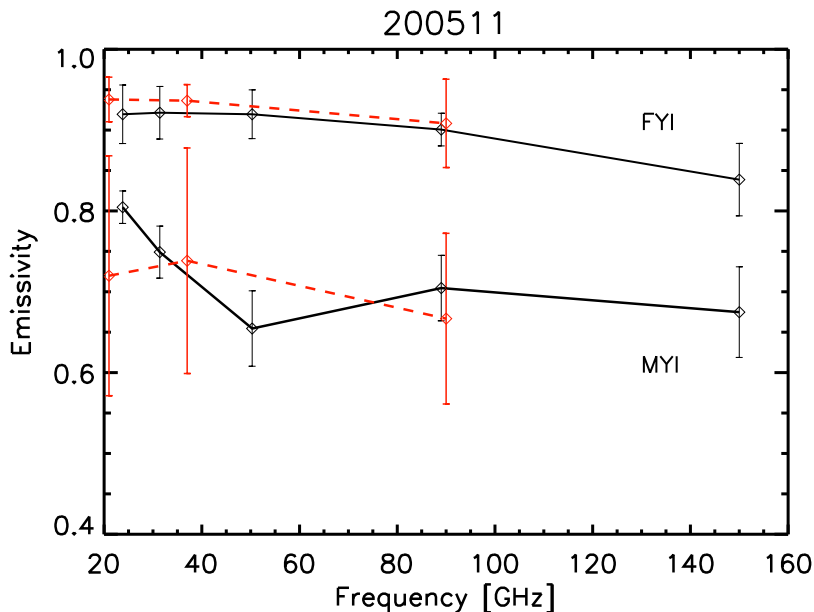
Figure 6.7: Emissivity comparison with literature value Eppler et al. (1992).
Solid lines represent retrieved emissivities and dashed lines represent those
from the literature

6.2 AMSR-E Emissivities

The emissivities calculated using the data obtained from the AMSR-
E instrument on the Aqua platform for the year 2005 are presented
here. Emissivity variations are studied over the two same test regions
selected for the study of emissivities with AMSU data. AMSR-E is a
conically scanning passive microwave imager with an incidence an-
gle of around 55°. The emissivity variation with frequency for all the
months of the year 2005 for all twelve frequencies at both polariza-
tions are studied for first-year ice and multiyear ice (section 6.2.1).
The seasonal variation of emissivities for all frequencies in both polar-
izations is observed (section 6.2.2). Surface emissivity retrieved with
AMSR-E data and with AMSU data are compared and the results are
shown in section 6.2.3. The correlation in emissivity between different
frequencies at vertical and horizontal polarization are also analyzed
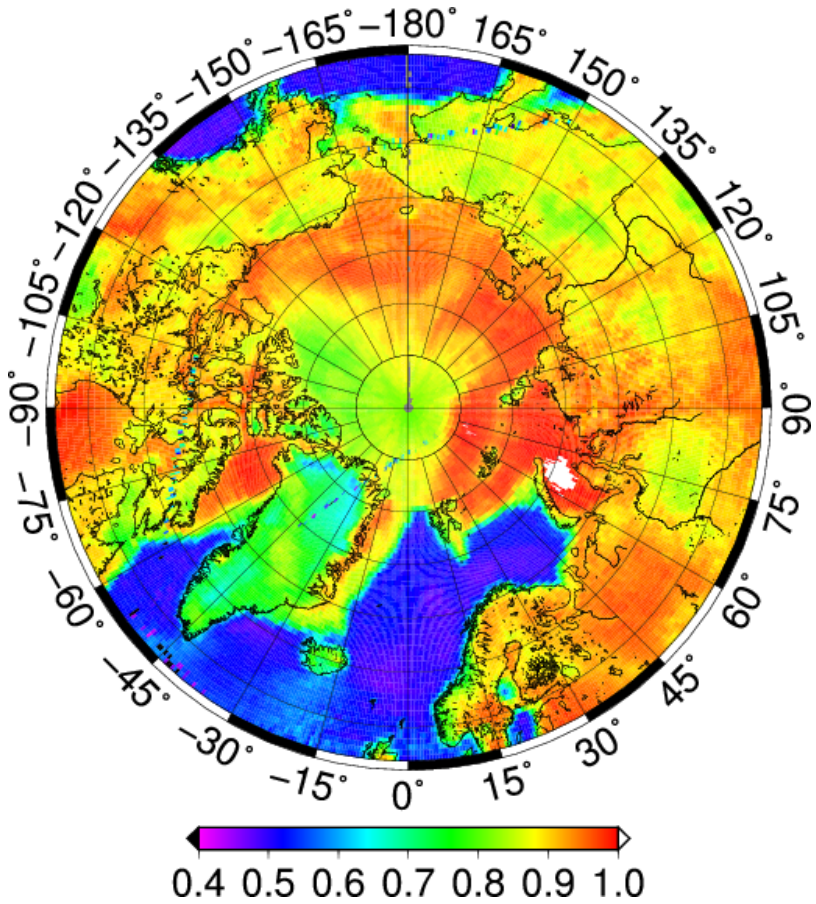
Figure 6.8: Surface emissivity map of the Arctic at 23 GHz, 15 March, 2003.
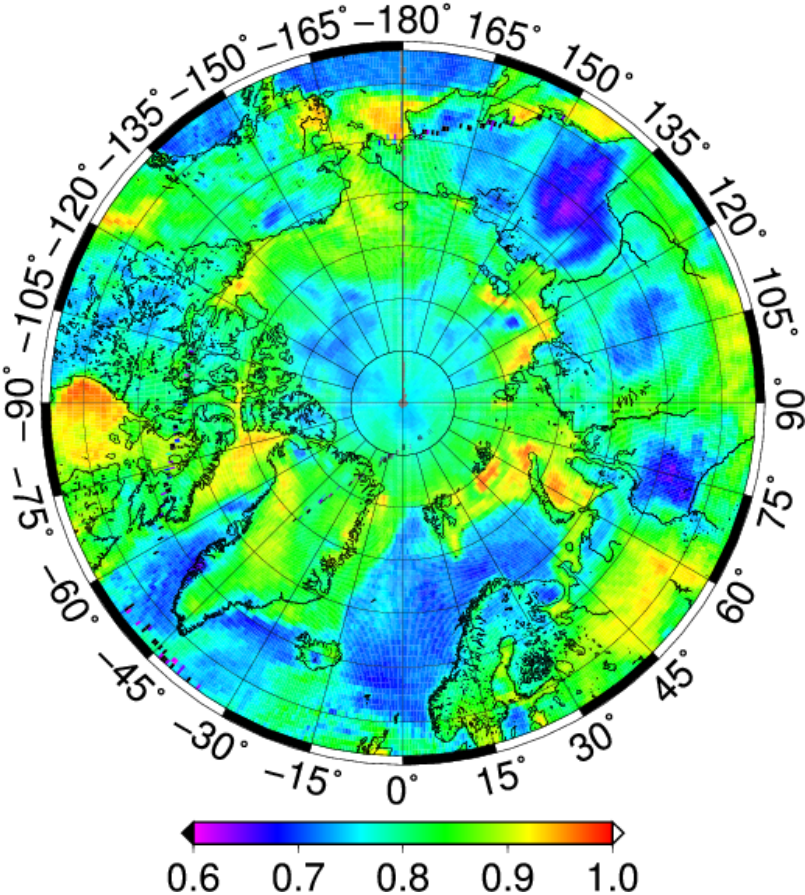
Figure 6.9: Surface emissivity map of the Arctic at 89 GHz, 15 March, 2003.

(section 6.2.4). The results are compared with emissivity values in the literature in section 6.2.5.

6.2.1 Frequency Variation

Figure 6.10 shows the variation of the monthly averaged emissivities of first-year ice at AMSR-E frequencies for both vertical and horizontal polarization for the year 2005. The frequency dependence of emissivity and the difference between emissivities at two polarizations vary for different months. The x-axis represents AMSR-E frequencies and the y-axis represents emissivities. Solid lines represent vertically polarized emissivities and dashed lines represent horizontally polarized emissivities. Starting from November till January, emissivity variation with frequency is low with a slight decrease at high frequencies as observed for AMSU frequencies (Figure 6.10). From February till April the decrease of emissivity with frequency is pronounced. During this period snow depth increases and high frequencies undergo scattering. During the month June, the air temperature becomes higher and ice starts to melt. In that period the emissivity at all frequencies is lowered. Then the difference between vertical and horizontal emissivity starts to increase. From July till October the characteristics of open ocean is observed: increase in emissivity with frequency and the large difference between vertical and horizontal emissivities. The average surface emissivity of first-year ice for all months in 2005 is shown in Table 6.1.

Figure 6.11 shows the variation of the monthly averaged emissivities of multiyear ice at AMSR-E frequencies for both vertical and horizontal polarization for the year 2005. The emissivity variation with frequency for multiyear ice remains the same for all the months except the summer months June and July. The average surface emissivity of multiyear ice for all months in 2005 is shown in Table 6.2.
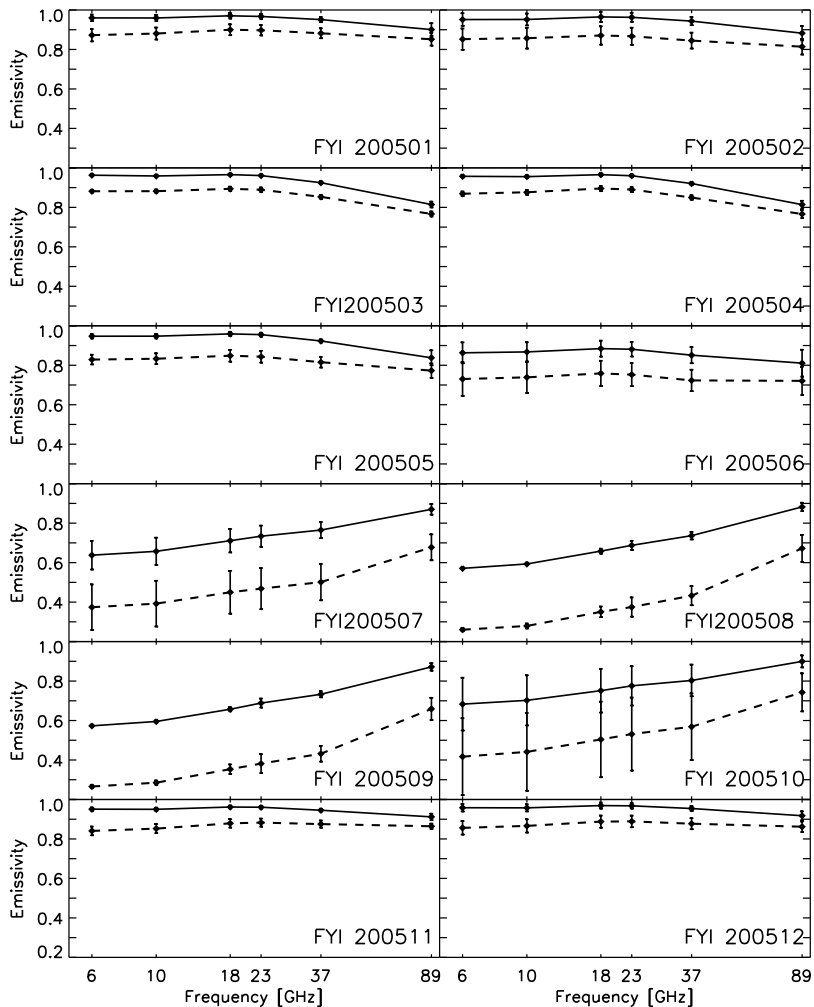
Figure 6.10: Surface emissivities of first-year ice at AMSR-E frequencies at vertical (solid line) and horizontal (dashed line) polarizations from January 2005 (top left, 'FYI 200501') to December 2005 (bottom right, 'FYI 200512').
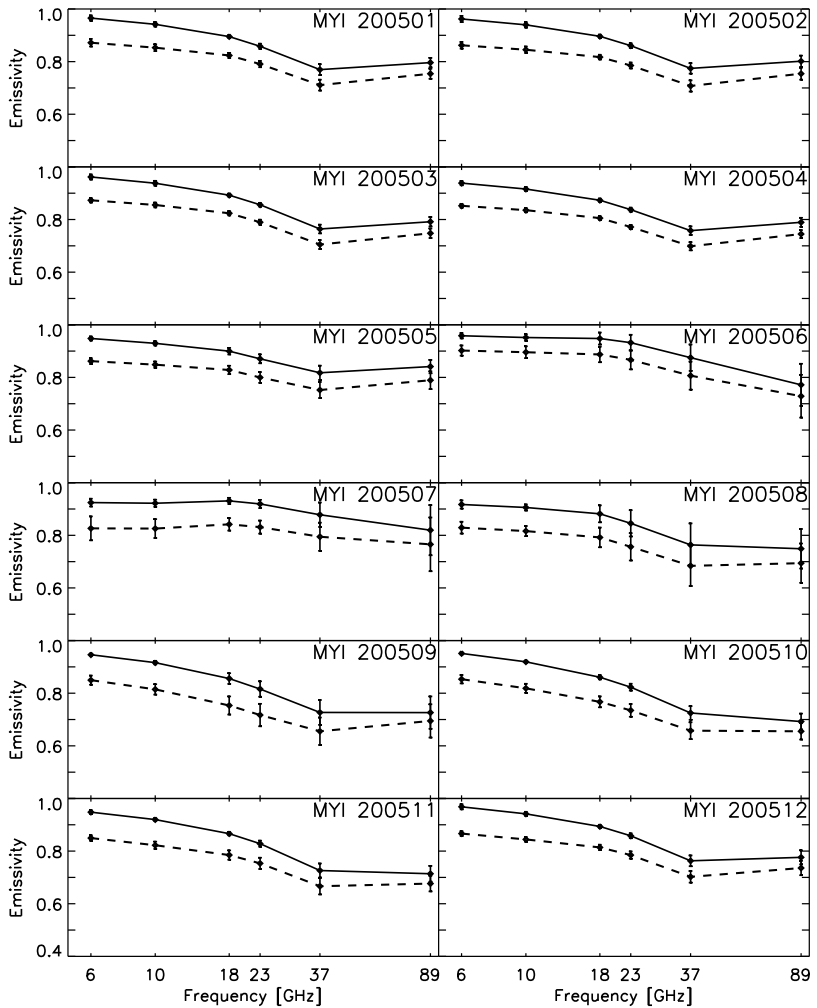
Figure 6.11: Surface emissivities of first-year ice at AMSR-E frequencies at vertical (solid line) and horizontal (dashed line) polarizations from January 2005 (top left, 'MYI 200501') to December 2005 (bottom right, 'MYI 200512').

Table 6.1: Average emissivity values for the first-year ice at AMSR-E frequencies.

Note: June, July and October: open water and sea ice mixed
August and September: open water

Month	Pol.	AMSR-E frequencies in GHz					
		6.9	10.6	18.7	23.8	36.5	89.0
Jan	V	0.960	0.959	0.970	0.967	0.951	0.900
	H	0.872	0.880	0.899	0.897	0.882	0.852
Feb	V	0.951	0.952	0.965	0.963	0.944	0.882
	H	0.852	0.857	0.871	0.867	0.845	0.814
Mar	V	0.963	0.959	0.966	0.961	0.925	0.814
	H	0.882	0.882	0.894	0.889	0.853	0.766
Apr	V	0.957	0.955	0.965	0.960	0.921	0.814
	H	0.869	0.876	0.895	0.890	0.849	0.766
May	V	0.947	0.947	0.959	0.955	0.923	0.838
	H	0.829	0.833	0.848	0.843	0.815	0.773
Jun	V	0.863	0.867	0.884	0.881	0.851	0.812
	H	0.729	0.738	0.758	0.752	0.722	0.722
Jul	V	0.642	0.661	0.714	0.735	0.765	0.866
	H	0.381	0.399	0.455	0.471	0.502	0.671
Aug	V	0.571	0.593	0.658	0.687	0.736	0.882
	H	0.260	0.279	0.350	0.375	0.432	0.672
Sep	V	0.573	0.595	0.657	0.688	0.733	0.871
	H	0.265	0.285	0.353	0.381	0.432	0.659
Oct	V	0.683	0.702	0.751	0.775	0.803	0.899
	H	0.417	0.441	0.504	0.531	0.568	0.743
Nov	V	0.951	0.950	0.962	0.961	0.945	0.912
	H	0.840	0.852	0.879	0.883	0.875	0.864
Dec	V	0.958	0.957	0.969	0.968	0.954	0.917
	H	0.856	0.866	0.888	0.889	0.877	0.862

Table 6.2: Average emissivity values for the multiyear ice at AMSR-E frequencies.

Month	Pol.	AMSR-E frequencies in GHz					
		6.9	10.6	18.7	23.8	36.5	89.0
Jan	V	0.968	0.944	0.894	0.854	0.762	0.791
	H	0.873	0.854	0.822	0.787	0.703	0.749
Feb	V	0.962	0.939	0.896	0.860	0.774	0.801
	H	0.862	0.845	0.817	0.785	0.707	0.754
Mar	V	0.961	0.937	0.892	0.855	0.763	0.791
	H	0.873	0.855	0.823	0.789	0.704	0.747
Apr	V	0.938	0.915	0.873	0.837	0.757	0.789
	H	0.852	0.835	0.805	0.771	0.698	0.744
May	V	0.947	0.929	0.899	0.870	0.817	0.841
	H	0.862	0.848	0.828	0.799	0.752	0.789
Jun	V	0.958	0.951	0.947	0.932	0.874	0.771
	H	0.902	0.895	0.887	0.866	0.806	0.728
Jul	V	0.924	0.921	0.930	0.919	0.878	0.819
	H	0.826	0.825	0.841	0.831	0.794	0.765
Aug	V	0.917	0.905	0.881	0.845	0.763	0.748
	H	0.829	0.816	0.791	0.756	0.683	0.694
Sep	V	0.946	0.916	0.855	0.815	0.726	0.726
	H	0.849	0.814	0.753	0.716	0.655	0.694
Oct	V	0.951	0.919	0.860	0.822	0.724	0.692
	H	0.853	0.818	0.767	0.734	0.657	0.655
Nov	V	0.948	0.919	0.866	0.828	0.726	0.713
	H	0.849	0.822	0.784	0.753	0.666	0.676
Dec	V	0.968	0.941	0.893	0.858	0.763	0.776
	H	0.866	0.844	0.814	0.784	0.702	0.735

Figure 6.12: Seasonal variation of emissivities of first-year ice at AMSR-E frequencies (vertical polarization (black) and horizontal polarization (blue)) 7 GHz (top left), 10 GHz, 18 GHz, 23 GHz, 37 GHz and 89 GHz (bottom right). Pink dashed line: ice concentration. Red dashed line: air temperature. Month 0 and 12 are the same.
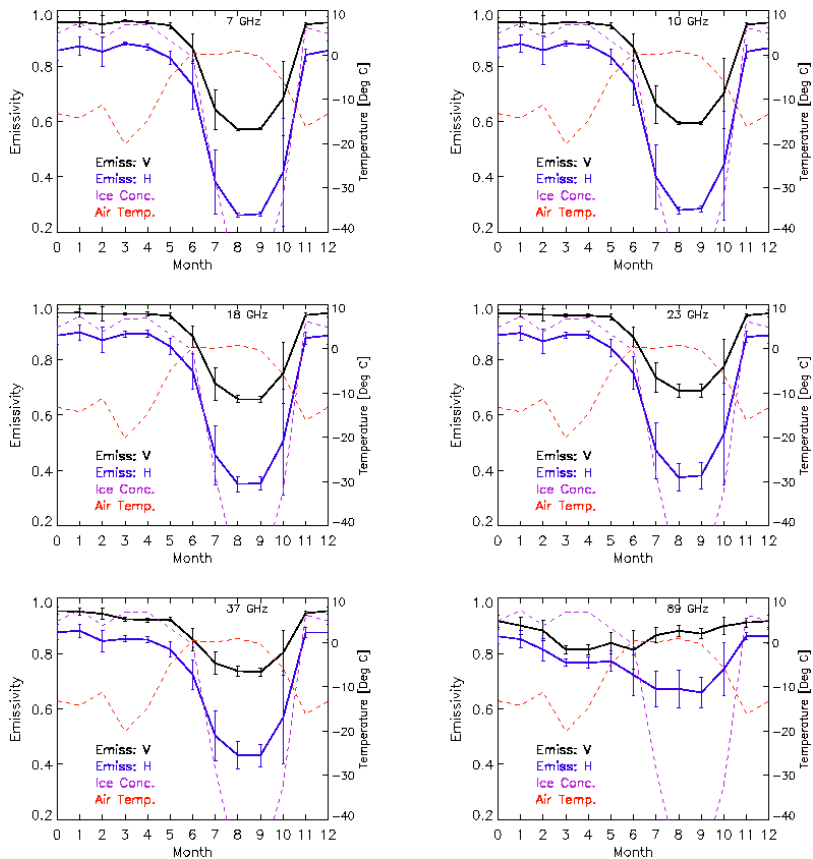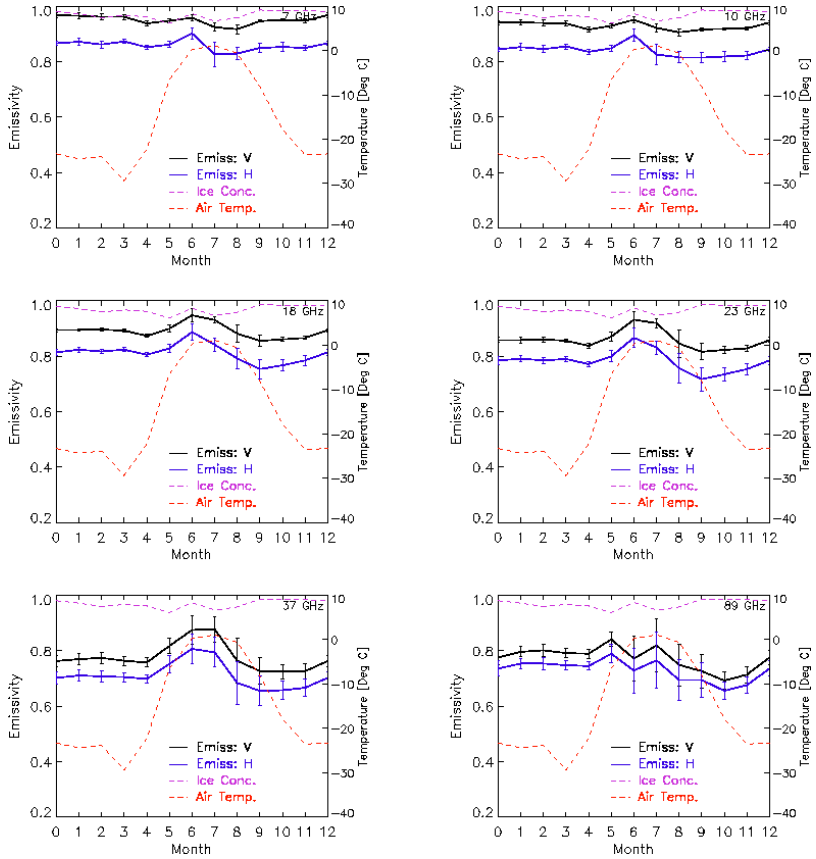
Figure 6.13: Seasonal variation of emissivities of multiyear ice at AMSR-E frequencies (vertical polarization (black) and horizontal polarization (blue)) 7 GHz (top left), 10 GHz, 18 GHz, 23 GHz, 37 GHz and 89 GHz (bottom right). Pink dashed line: ice concentration. Red dashed line: air temperature. Month 0 and 12 are the same.

6.2.2 Seasonal Variation

Figure 6.12 shows the seasonal variation of the emissivity of first-year ice at six different frequencies. The panel at top left shows the variation of surface emissivity at 7 GHz. The black line indicates the emissivities at vertical polarization and blue indicates those at horizontal polarization. The red line indicates the average air temperature and pink line indicates the ice concentration. During the winter months, the air temperature is very low and the water freezes to ice. The surface emissivity and ice concentration are very high and difference between horizontal and vertical emissivity is low. During the months June, July and October the surface contains both open water and ice. So the variability in emissivity is high (large error bars). During August and September, the air temperature is higher, the ice completely melts, ice concentration drops near zero and the emissivity of open water is observed. The the difference between vertical and horizontal emissivities becomes around 0.35. Same seasonal variations are observed for all frequencies till 37 GHz. The bottom left panel shows the vertical and horizontal emissivity variations at 89 GHz. The seasonal variation at this frequency is much less. However the difference between the horizontal and vertical emissivities for summer months (open water) is very high compared to winter months (sea ice). This property has been utilized to retrieve ice concentration at high resolution (Spreen et al., 2007).

Figure 6.13 shows the seasonal variation of the emissivity of multi-year ice at six different frequencies. The emissivities at vertical polarization (black line) and horizontal polarization (blue line) for frequencies 7 – 37 GHz remain constant for all the months except the summer months May to September. Starting from May the emissivities start to increase and reaches maximum in June (0.95 for 7 GHz) and again decreases. The least seasonal variation is observed for 7 GHz, the frequency which penetrates deepest. The physical properties and temperature remain constant for deeper layers and so do the emissivities. The variation of emissivity with season is larger for 89 GHz. The ice concentration (pink dashed line) remains high through out the year. The air temperature (red dashed line) varies from $-30\,^\circ$C (March) to

0 °C (July). The difference between horizontally polarized emissivities
and vertically polarized emissivities remain around 0.1 for all seasons
for frequencies 7 – 37 GHzand for 89 GHz it is around 0.05.

6.2.3 Comparison with AMSU Emissivities

Figure 6.14 shows the comparison between emissivities retrieved from
AMSU and AMSR-E instruments at the first-year ice site. AMSR-E mea-
sures brightness temperature both at horizonal and vertical polariza-
tions whereas AMSU measures in a mixed polarization according to
(4.6). AMSR-E has fixed incidence angle 55° with corresponding scan
angle of 47.4°. Here AMSU emissivities at incidence angle of 53.08° is
compared with the AMSR-E emissivities. The top left panel shows the
emissivities in January and the bottom right panel shows the emissivi-
ties in December. Solid lines represent AMSR-E emissivities and dotted
lines represent AMSU emissivities.

Figure 6.15 shows the comparison between emissivities retrieved
from AMSU and AMSR-E instruments at the multiyear ice site.

The AMSU emissivities and AMSR-E emissivities, combined for AMSU
polarization mixing, show good agreement at all frequencies and for
all months.

6.2.4 Emissivity Correlation

The correlation between the emissivities at different frequencies is an-
alyzed for both first-year ice and for multiyear ice. Figure 6.16 shows
the mutual correlation first-year ice emissivities at all frequencies. Dif-
ferent color represent different frequencies. Solid lines represent fre-
quencies at vertical polarizations and and dotted lines represent fre-
quencies at horizontal frequencies. Each curve shows the correlation
of the emissivity at one frequency with frequencies indicated on the
x-axis. Different panels represent different months. The correlation of
emissivities varies with season. Lower frequencies (7 – 37 GHz) show
similar behavior in correlation and all are correlated each other and
the are least correlated to 89 GHz. The correlation of 89 GHz(red line)
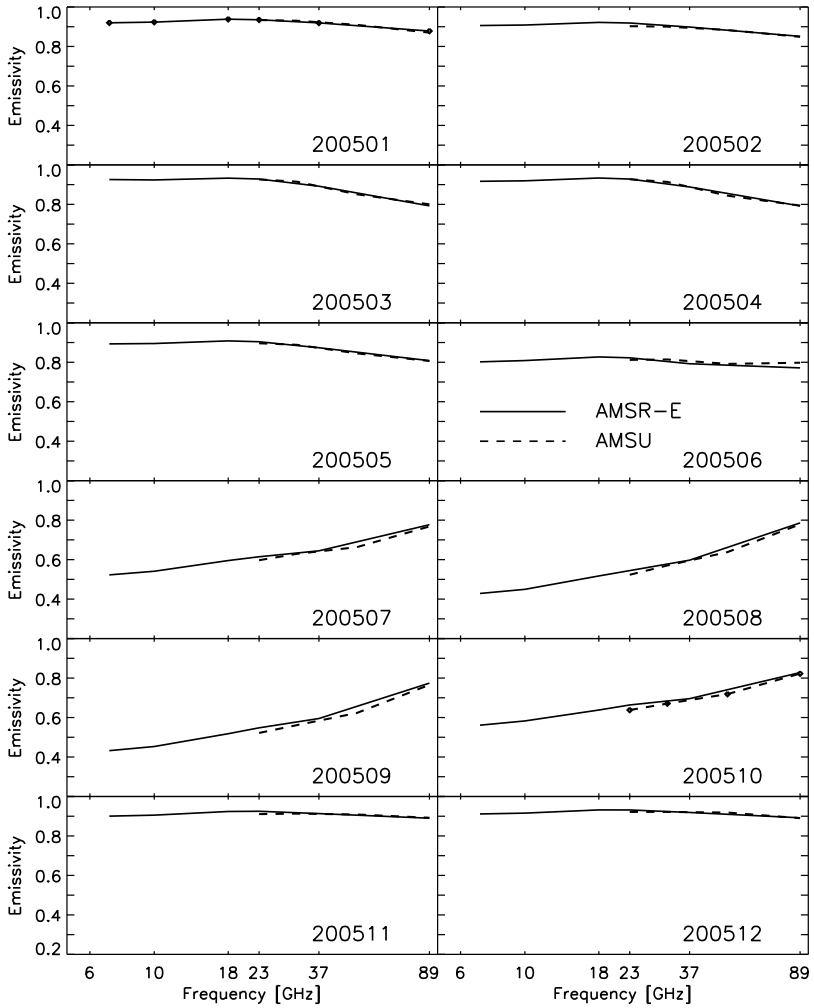
Figure 6.14: Comparison between emissivities retrieved from AMSU (dashed line) and AMSR-E (solid line) instruments over first-year ice.
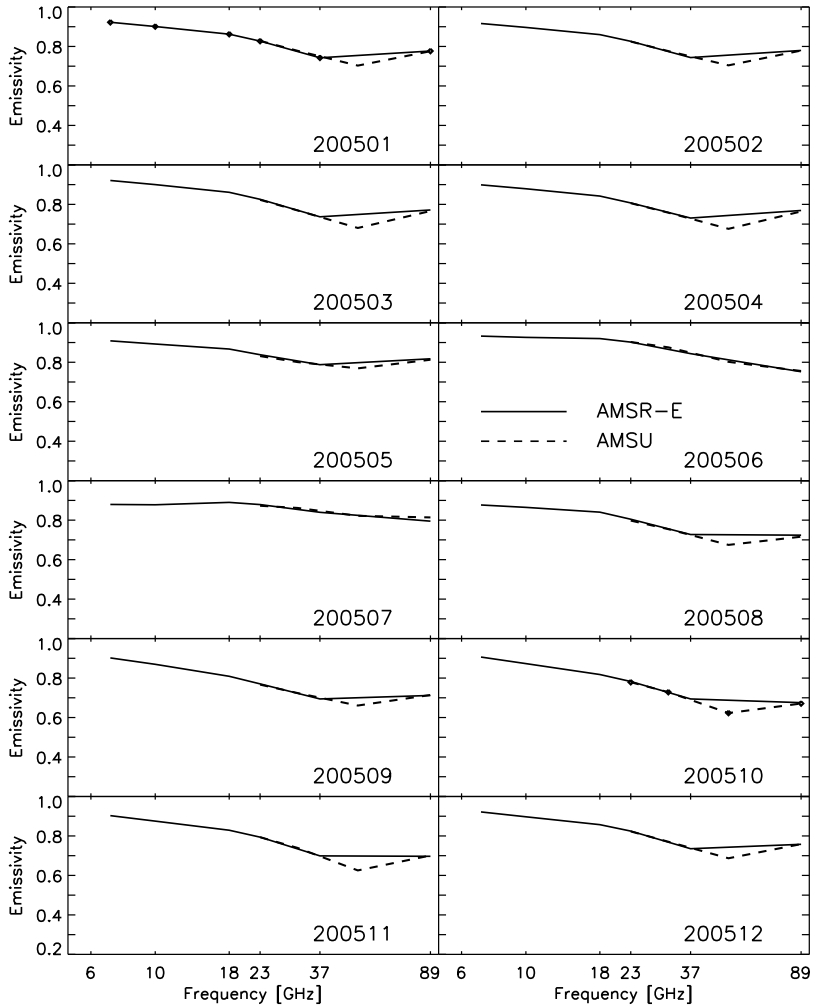
Figure 6.15: Comparison between emissivities retrieved from AMSU (dashed line) and AMSR-E (solid line) instruments over multiyear ice.
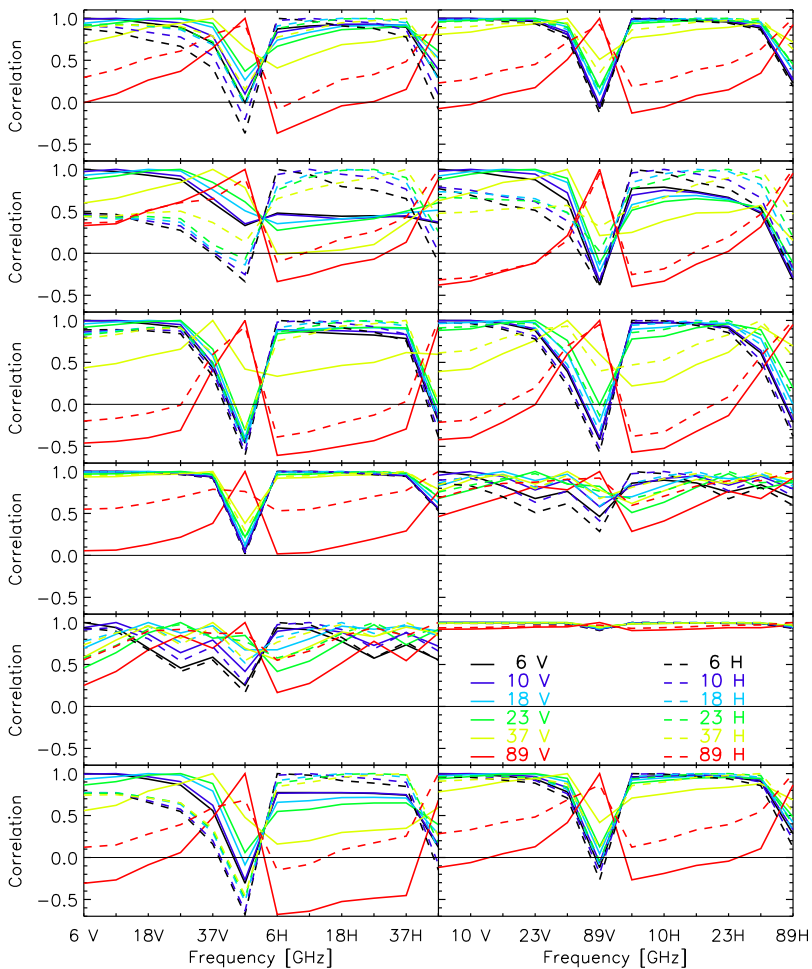
Figure 6.16: Correlation between emissivities in a first-year ice region. Solid lines represent vertical polarizations and dotted lines represent horizontal polarizations. Different panels represent different months. Top left: January 2005 and bottom right: December 2005.
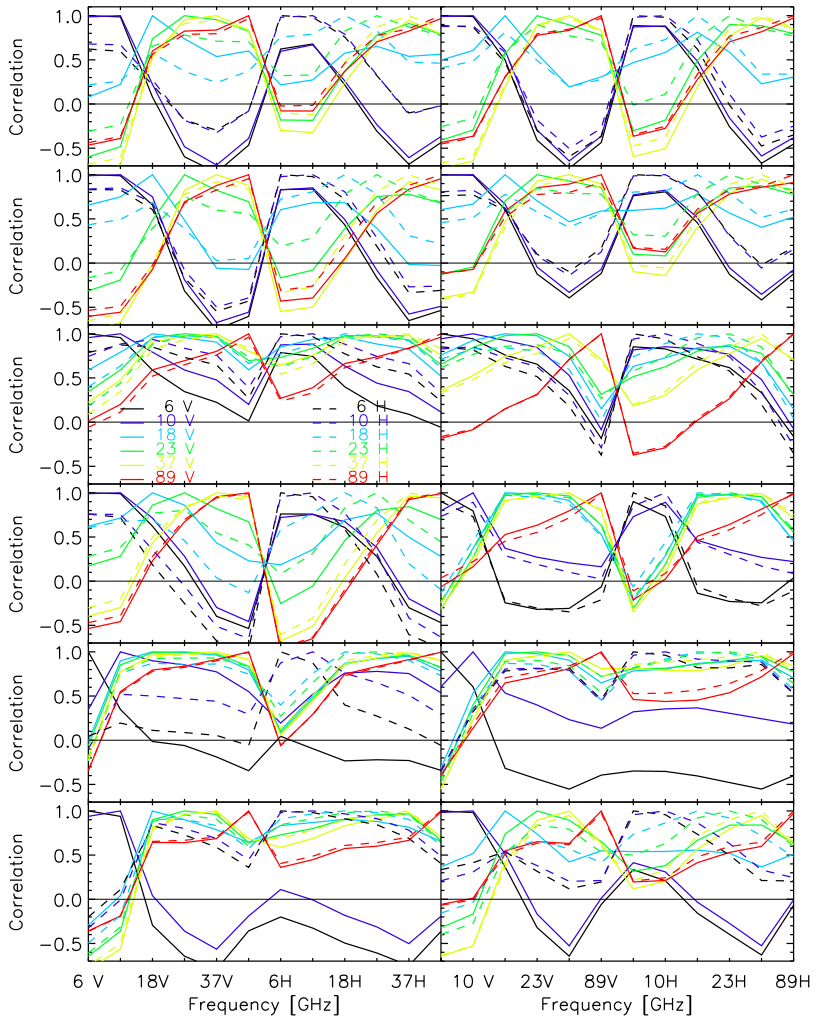
Figure 6.17: Correlation between emissivities in a multiyear ice region. Solid lines represent vertical polarizations and dotted lines represent horizontal polarizations. Different panels represent different months. Top left: January 2005 and bottom right: December 2005.

is different. It is least correlated to low frequencies. During October all
emissivities are correlated to each other and the corelation is around
one. During this month freezing starts. Figure 6.17 shows the mutual
correlation of multiyear ice emissivities at all frequencies. The correla-
tion of emissivities with different frequencies are different for first-year
ice and multiyear ice.

6.2.5 Comparison with Literature
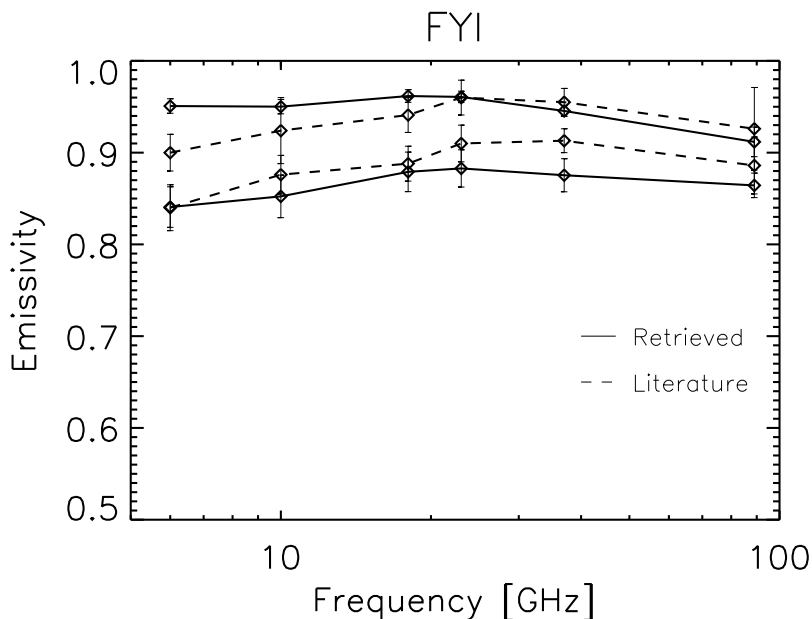
Figure 6.18: First-year ice emissivity comparison with literature value Ep-
pler et al. (1992). Solid lines represent retrieved emissivities and dotted lines
represent those from the literature. Upper lines: vertical polarization and
lower lines: horizontal polarization.

Figure 6.18 compares first-year ice emissivities retrieved for the
month November to those from the literature Eppler et al. (1992).
For first-year ice the retrievals match well with the literature values.
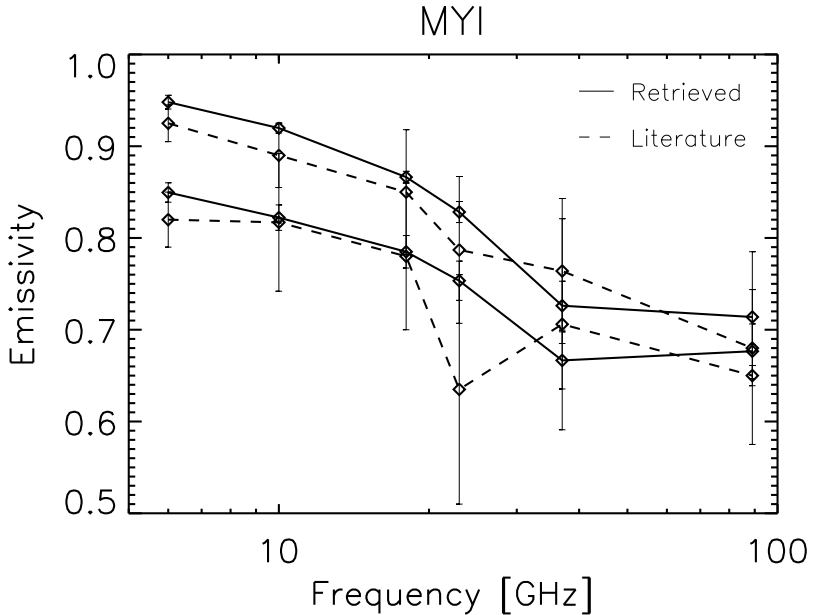
Figure 6.19: Multiyear ice emissivity comparison with literature value Eppler et al. (1992). Solid lines represent retrieved emissivities and dotted lines represent those from the literature. Upper lines: vertical polarization and lower lines: horizontal polarization.

Only 7 GHz vertically polarized emissivity is not within the mutual error limits.

Figure 6.19 compares multiyear ice emissivities retrieved for the month November to those from the literature Eppler et al. (1992). For multiyear ice the retrievals match well with the literature values.

6.3 Summary and Conclusion

The emissivities of two test regions, one covered with first-year ice in winter months and the other with multiyear ice are calculated at the window channels of passive microwave sounder AMSU passive microwave imager AMSR-E.

Correction factors (regression coefficients) are derived for different

frequencies and for different seasons by analyzing SHEBA data at a first-year ice site and a multiyear ice site. Applying the regression coefficients, lowest level air temperatures are corrected to emitting layer temperatures. Corrections are much required for lower frequencies and for winter seasons. Low frequency penetrates deeper. During winter sea ice is covered with snow and the temperature gradient in snow cover is higher than sea ice. During summer months, first year ice melts and no temperature variation is dominant for multiyear ice.

Angular and frequency dependence of the emissivity of different polar surface types are studied. The local zenith angle variation of AMSU emissivities up to $45°$ corresponding to scan positions 4 to 27 for AMSU-A and 10 to 81 for AMSU-B is negligible and for higher incidence angles emissivity decreases. As the frequency increases, the emissivity decreases for sea ice. For young ice the variation of emissivity with frequency is smaller.

The monthly variations of emissivities for different frequencies are derived for the specific regions for the whole year 2005. The ice concentrations of the region are also noticed. During the summer months first-year ice melts and emissivities drop to open water emissivities whereas for multiyear ice a slight increase in emissivity is observed. The frequency dependence of emissivity varies in different months especially at high frequencies due to the variation of snow cover. multiyear ice emissivities at 89 GHz and I50 GHz show larger variation (maximum up to 40%) during the summer months June, July, August and September. Emissivity maps are produced to see the emissivity variation for different surface types of the Arctic.

The emissivity information and the regression coefficients to derive emitting layer temperature from the lowest level temperature will be used to retrieve atmospheric profiles of temperature in Chapter 9.

Sea ice surface emissivities are retrieved from AMSR-E at the two test regions where the AMSU emissivity retrieval has been done. AMSR-E measures radiance at both horizontal and vertical polarizations. The difference in emissivities between two polarizations is more pronounced for open water than for sea ice. The variation of emissivity with frequency and season is observed. Seasonal variation is minimum for multiyear ice at 10 GHz. AMSR-E emissivities are compared with

amsu emissivities and with emissivities from the literature. In both
the case good agreement is found.

7 Optimal Estimation Method

Satellite radiometers make measurements of radiation emitted by the atmosphere and the surface underneath. Our aim is to derive atmospheric parameters such as temperature and humidity from the measured radiance, which is a typical retrieval problem. In order to find the solution for the retrieval problem, one has to formulate the problem properly by describing the measurement in terms of some forward model, find the best solution and to understand the solution or answer. Practically the problem is not trivial since the forward models are not explicitly invertible, the problem might be ill-conditioned and/or ill-posed and also the the errors in measurement can map into errors in solution in a non-trivial way. In this chapter, the optimal estimation method (Rodgers, 1976; Houghton et al., 1983; Rodgers, 2000) used for the temperature/humidity profile retrieval is outlined.

7.1 Measurement Vector and State Vector

Any measurement we make in order to retrieve the desired quantity are represented by a measurement vector $\boldsymbol{y}$ with m elements $y_1, y_2, y_3, \ldots, y_m$.

The quantities to be retrieved are represented by a state vector $\boldsymbol{x}$ with n elements, $x_1, x_2, x_3, \ldots, x_n$. The desired quantity is often continuous e.g., a temperature profile. We can however, only make a finite number of measurements and calculations. So we have to express the unknown in terms of a finite number of parameters, such as temperature on a set of pressure levels.

7.2 Vector Space

In concept of vector spaces, it is convenient to think in terms of linear algebra using vectors even if the forward model is not linear. We consider two such spaces, the measurement space, the space of measurement vectors having m dimensions and the state space, the space of state vectors having n dimensions. Generally the two vector spaces will have different dimensions.

7.3 Forward Model

The Forward Function $\boldsymbol{f}(\boldsymbol{x})$ maps from state space onto measurement space, according the physics of the measurement. The Forward Model $\boldsymbol{F}(\boldsymbol{x})$ is the best approximation of the detailed physics involved in the measurement. Therefore, the relation between the measurement vector and state vector can be written as:

$$\boldsymbol{y} = \boldsymbol{F}(\boldsymbol{x}) + \boldsymbol{e} \qquad\qquad (7.1)$$

where $\boldsymbol{y}$ is the measurement with error $\boldsymbol{e}$, and $\boldsymbol{F}(\boldsymbol{x})$ is a vector valued state function of the state which encapsulates our understanding of the physics of the measurement.

7.4 Inverse or Retrieval Method

The inverse problem/method is the finding of an inverse mapping $\boldsymbol{R}(\boldsymbol{y})$: Given a point in measurement space, which point or set of points in state space could have mapped into it?

7.5 Bayesian Approach

All real measurements are subject to experimental error or 'noise', so that any practical retrieval must allow for this. Given a measurement

together with a description of its error statistics, a forward model describing the relation between the measurement and the unknown state and any *a priori* information, Bayesian approach allows us to identify a class of possible states that are consistent with the available information and to assign the probability density to them. In other words it allows us to describe our knowledge in terms of probability density functions (pdf's). It poses a question: What is the pdf of the state, given the measurement and the *a priori*? Bayes' theorem states:

$$P(\boldsymbol{x}, \boldsymbol{y}) = P(\boldsymbol{x}|\boldsymbol{y})P(\boldsymbol{y}) \tag{7.2}$$

and

$$P(\boldsymbol{y}, \boldsymbol{x}) = P(\boldsymbol{y}|\boldsymbol{x})P(\boldsymbol{x}) \tag{7.3}$$

so that

$$P(\boldsymbol{x}|\boldsymbol{y}) = \frac{P(\boldsymbol{y}|\boldsymbol{x})P(\boldsymbol{x})}{P(\boldsymbol{y})} \tag{7.4}$$

where

$P(\boldsymbol{x})$ is the *a priori* pdf of the state, describing what we know about the state before we make the measurement

$P(\boldsymbol{y})$ is the *a priori* pdf of the measurement

$P(\boldsymbol{x}, \boldsymbol{y})$ is the joint *a priori* pdf of $\boldsymbol{x}$ and $\boldsymbol{y}$

$P(\boldsymbol{y}|\boldsymbol{x})$ is the pdf of the measurement given the state - this depends on experimental error and the forward function

$P(\boldsymbol{x}|\boldsymbol{y})$ is the pdf of the state given the measurement - this is what we want to find

If we have a prior pdf for $\boldsymbol{x}$, $P(\boldsymbol{x})$, and we know statistically how $\boldsymbol{y}$ is related to $\boldsymbol{x}$ via $P(\boldsymbol{y}|\boldsymbol{x})$, then we can find an un-normalized version of $P(\boldsymbol{x}|\boldsymbol{y})$, namely $P(\boldsymbol{y}|\boldsymbol{x})P(\boldsymbol{x})$, which can be normalized if required.

If we assume that experimental error is Gaussian we can express $P(\boldsymbol{y}|\boldsymbol{x})$ as

$$-2\ln P(\boldsymbol{y}|\boldsymbol{x}) = \big(\boldsymbol{y} - \boldsymbol{F}(\boldsymbol{x})\big)^{\mathrm{T}} \boldsymbol{S}_e^{-1}\big(\boldsymbol{y} - \boldsymbol{F}(\boldsymbol{x})\big) + c_1 \tag{7.5}$$

where $\boldsymbol{F}(\boldsymbol{x})$ is the forward model: $\boldsymbol{y} = \boldsymbol{F}(\boldsymbol{x}) + \boldsymbol{e}$ and $\boldsymbol{S}_e$ is the covariance matrix of the experimental error, $\boldsymbol{e}$:

$$\boldsymbol{S}_e = E\{\boldsymbol{e}\boldsymbol{e}^{\mathrm{T}}\} = E\{\big(\boldsymbol{y} - \boldsymbol{F}(\boldsymbol{x})\big)\big(\boldsymbol{y} - \boldsymbol{F}(\boldsymbol{x})\big)^{\mathrm{T}}\} \tag{7.6}$$

and c_1 is a constant.

On the less justifiable assumption that the *a priori* pdf is Gaussian we can write:

$$-2\ln P(\boldsymbol{x}) = (\boldsymbol{x} - \boldsymbol{x_a})^{\mathrm{T}} \boldsymbol{S_a}(\boldsymbol{x} - \boldsymbol{x_a}) + c_2 \qquad (7.7)$$

if $\boldsymbol{x}$ is distributed normally with mean $\boldsymbol{x_a}$ and covariance $\boldsymbol{S_a}$. Thus:

$$\begin{aligned} -2\ln P(\boldsymbol{x}|\boldsymbol{y}) = \big(\boldsymbol{y} - \boldsymbol{F}(\boldsymbol{x})\big)^{\mathrm{T}} \boldsymbol{S_e^{-1}}\big(\boldsymbol{y} - \boldsymbol{F}(\boldsymbol{x})\big) \\ + (\boldsymbol{x} - \boldsymbol{x_a})^{\mathrm{T}} \boldsymbol{S_a^{-1}}(\boldsymbol{x} - \boldsymbol{x_a}) + c_3 \quad (7.8) \end{aligned}$$

where c_3 is a constant. The term

$$\big(\boldsymbol{y} - \boldsymbol{F}(\boldsymbol{x})\big)^{\mathrm{T}} \boldsymbol{S_e^{-1}}\big(\boldsymbol{y} - \boldsymbol{F}(\boldsymbol{x})\big) + \big(\boldsymbol{x} - \boldsymbol{x_a}\big)^{\mathrm{T}} \boldsymbol{S_a^{-1}}(\boldsymbol{x} - \boldsymbol{x_a}) \qquad (7.9)$$

is generally called cost function. We wish to select one of the possible states as the solution to the inverse problem and to assign it with some error estimate. There exists several solution methods. The one we use is the Maximum a-posteriori (Maximum likelihood in atmospheric remote sounding) and Minimum variance method is a closely related method.

7.6 Error Analysis and Characterization

When a retrieval problem is ill-posed, so that it doesn't have a unique solution, we have to select one which is 'best' or 'optimal' from an infinite number of possible solutions. If we want our retrieval to optimize something, we need to know what properties a retrieved state vector might have, so we can choose what we need optimize. We will therefore set up a formal characterization that can be aplied to any retrieval method. The measurement $\boldsymbol{y}$ is conceptually a function of some unknown state $\boldsymbol{x}$:

$$\boldsymbol{y} = \boldsymbol{f}(\boldsymbol{x}, \boldsymbol{b}) + \boldsymbol{e} \qquad (7.10)$$

where,
$\boldsymbol{b}$ is a set of 'known' parameters of this function

e is measurement error, with covariance S_e

The retrieval x is conceptually a function of the form:

$$\hat{x} = R(y, \hat{b}, c) \tag{7.11}$$

where:

R represents the retrieval method,

$\hat{b}$ is the estimate of the forward function parameters b, c represents any parameters used in the inverse method that do not affect the measurement, e.g., *a priori*. Thus the retrieval is related to the 'truth' x formally by:

$$\hat{x} = R(f(x, b) + e, \hat{b}, c) \tag{7.12}$$

which may be regarded as the transfer function of the measurement and retrieval system as a whole. Characterization means evaluating $\partial \hat{x}/\partial x = A$, sensitivity to actual state known as Averaging Kernel.

Error analysis involves evaluating:

$\partial \hat{x}/\partial x = G_y$, sensitivity to noise (or to measurement)

$\partial \hat{x}/\partial b = G_b$, sensitivity to non-retrieved parameters

$\partial \hat{x}/\partial c = G_c$, sensitivity to retrieval method parameters

and understanding the effect of replacing the forward function f by a numerical forward model F.

7.7 The Non-linear Case

The general remote sounding problem is non-linear. Main source of non-linearity is the problem itself, i.e. a non-linear forward model and the non-Gaussian statistics. The Bayesian solution for Gaussian statistics is:

$$-2\ln\big(P(x|y)\big) = \big(y - F(x)\big)^{\mathrm{T}} S_e^{-1}\big(y - F(x)\big)$$
$$+ (x - x_a)^{\mathrm{T}} S_a^{-1}(x - x_a) + c \tag{7.13}$$

The maximum likelihood $\left(\frac{\partial}{\partial x}P(x|y) = 0\right)$ solution requires the solution of:

$$0 = \nabla_x\left(-2\ln\big(P(x|y)\big)\right)$$
$$= -K^{\mathrm{T}} S_e^{-1}\big(y - F(x)\big) + S_a^{-1}(x - x_a) \tag{7.14}$$

where $\boldsymbol{K} = \frac{\partial}{\partial \boldsymbol{x}} \boldsymbol{F}(\boldsymbol{x})$.

If the statistics were non-Gaussian, this equation would be non-linear in $\boldsymbol{x}$, even if $\boldsymbol{F}$ were linear. Newton's method for finding the zero of a scalar function $f(x)$ of one variable is:

$$x_{n+1} = x_n - \left(\frac{\mathrm{d}f(x_n)}{\mathrm{d}x} \right)^{-1} f(x_n) \tag{7.15}$$

The version for a vector-valued function of a vector, $\boldsymbol{g}(\boldsymbol{x})$, is:

$$\boldsymbol{x_{(n+1)}} = x_n - \left(\nabla_{\boldsymbol{x}} \boldsymbol{g}(\boldsymbol{x_n}) \right)^{-1} \boldsymbol{g}(\boldsymbol{x_n}) \tag{7.16}$$

where the inverse is a matrix inverse. If we apply this to the maximum a posteriori problem (Eqn. 7.14):

$$\boldsymbol{g}(\boldsymbol{x}) = -\boldsymbol{K}^{\mathrm{T}} \boldsymbol{S}_e^{-1} \left(\boldsymbol{y} - \boldsymbol{F}(\boldsymbol{x}) \right) + \boldsymbol{S_a}^{-1} \left(\boldsymbol{x} - \boldsymbol{x_a} \right) \tag{7.17}$$

we get:

$$\nabla_{\boldsymbol{x}} \boldsymbol{g} = -\nabla_{\boldsymbol{x}} \boldsymbol{K}^{\mathrm{T}} \boldsymbol{S}_e^{-1} \left(\boldsymbol{y} - \boldsymbol{F}(\boldsymbol{x}) \right) + \boldsymbol{K}^{\mathrm{T}} \boldsymbol{S}_e^{-1} \boldsymbol{K} + \boldsymbol{S_a}^{-1} \tag{7.18}$$

If we ignore the term involving $\nabla_{\boldsymbol{x}} \boldsymbol{K}^T$ – it is usually small – we get:

$$\boldsymbol{x_{n+1}} = \boldsymbol{x_n} + \left(\boldsymbol{S_a}^{-1} + \boldsymbol{K_n}^{\mathrm{T}} \boldsymbol{S_e}^{-1} \boldsymbol{K_n} \right)^{-1}$$
$$\left(\boldsymbol{K_n}^{\mathrm{T}} \boldsymbol{S_e}^{-1} \left(\boldsymbol{y} - \boldsymbol{F}(\boldsymbol{x_n}) \right) + \boldsymbol{S_a}^{-1} (\boldsymbol{x_n} - \boldsymbol{x_a}) \right) \tag{7.19}$$

Equation 7.19 is the so-called m-form of the iteration solution. In the so-called n-form it is:

$$\boldsymbol{x_{n+1}} = \boldsymbol{x_n} + \boldsymbol{S_a} \boldsymbol{K_n}^{\mathrm{T}} \left(\boldsymbol{K_n} \boldsymbol{S_a} \boldsymbol{K_n}^{\mathrm{T}} + \boldsymbol{S_e} \right)^{-1}$$
$$\left(\boldsymbol{y} - \boldsymbol{F}(\boldsymbol{x_n}) + \boldsymbol{K_n}(\boldsymbol{x_n} - \boldsymbol{x_a}) \right) \tag{7.20}$$

In m-form the matrix to be inverted is an $m \times m$ matrix, whereas in n-form the matrix to be inverted is and $n \times n$ matrix.

8 Retrieval of Temperature Profile

Temperature profiles of Earth's atmosphere can be derived from AMSU-A measurements. The twelve channels $3-14$ are located close to the oxygen absorption lines below $60\,\mathrm{GHz}$ which are used for the temperature retrieval. The left panel in figure 8.1 shows the weighting function distribution for all AMSU-A sounding channels and the right panel shows the that for humidity channels of AMSU-B (Karbou et al., 2005b). The weighting function indicates the relative contribution of each atmospheric layer to the measured radiance. For a given atmosphere and frequency, the peak altitude of weighting function increases with increasing zenith angle (Karbou et al., 2005b). This is due to increasing optical depth between the satellite and the instrument scan from nadir to higher angles at the outer swath. Temperature profiles are retrieved using an algorithm (Rosenkranz, 2006) developed for AIRS/AMSU/HSB, and adapted for use with NOAA-16 AMSU-A/B. A forward radiative transfer model is used to calculate microwave brightness temperatures. Components of the microwave model include an atmospheric transmittance model, a surface brightness model and model for the influence of surface scattering characteristics on reflected down-welling emission from the atmosphere.

8.1 Radiative Transfer Calculation

The equation of radiative transfer can be written in the form

$$T_B = T_{\mathrm{Bdirect}} + \tau\Big(T_{SB} + T_{Bsky}\big(1 - \frac{T_{SB}}{T_S}\big)\Big) \qquad (8.1)$$

where T_B is the brightness temperature emitted from the top of the atmosphere, τ is the one-way transmittance of the atmosphere, $T_{Bdirect}$
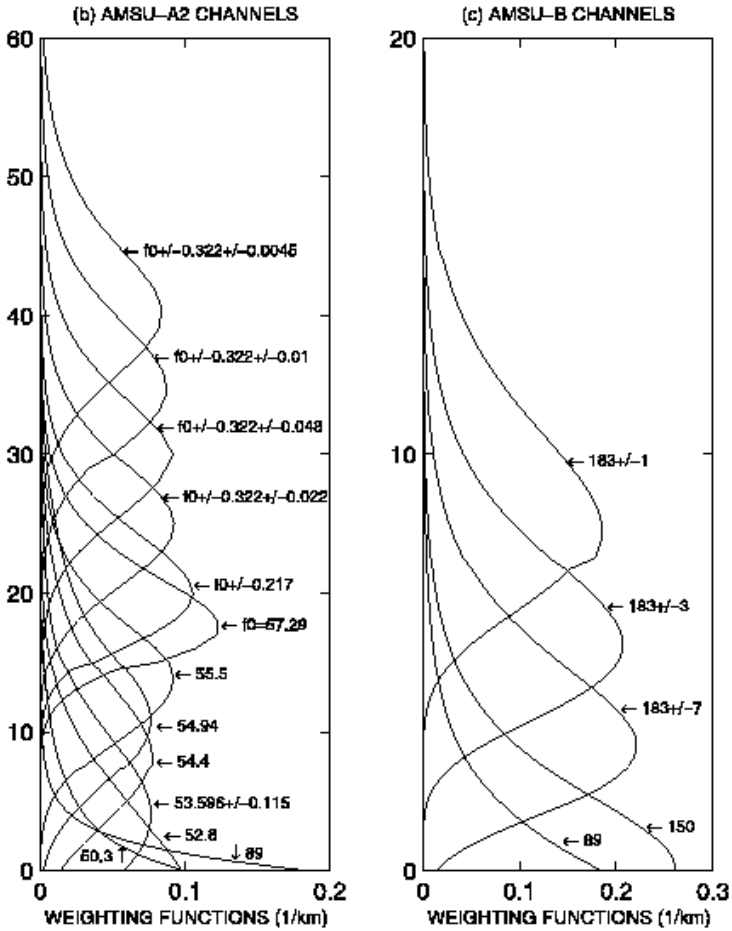
Figure 8.1: Weighting functions of AMSU channels. Y-axis represents height in km. Left panel: weighting functions of sounding channels of AMSU-A. Right panel: weighting factions of five AMSU-B channels. Figure Courtesy: (Karbou et al., 2005b).

is the component of the brightness temperature emitted from the atmosphere on a direct path to space, T_S is the surface temperature, T_{SB} is the surface brightness temperature and T_{Bsky} is the sky brightness temperature (including the attenuated cosmic contribution) as it would be observed from the surface. The form of Eqn. 8.1 allows separation of the estimation of surface brightness from estimation of temperature.

A rapid microwave transmittance algorithm (Rosenkranz, 2003) computes atmospheric transmittance for non-precipitating conditions. The algorithm makes use of the fact that microwave absorption lines of oxygen are well separated from those of water vapor, and they do not overlap one another.

8.2 Surface Brightness Model

The estimation of surface brightness temperature T_{SB} as a function of frequency ν is a part of microwave retrieval algorithm. Even though from a physical point of view, surface temperature and surface emissivity are separate variables, the retrieval treats the product of emissivity ε and temperature as surface brightness temperature (T_{SB}) as an independent variable because this product is closely related to the window channel measurement. Surface skin temperature is retrieved along with air temperature, with which it is correlated, from a different set of channels.

The first step in calculation of surface brightness temperature is a classification of the footprint (Grody et al., 2000) as having one of eight types of surface. The eight surface types are

0 coastline

1 land

2 water

3 high-emissivity sea ice/first-year ice (FYI)

4 low-emissivity sea ice/multiyear ice (MYI)

5 snow (high frequency scattering) (snow1)

6 glacier/snow (very low frequency scattering)

7 snow (low frequency scattering) (snow2)
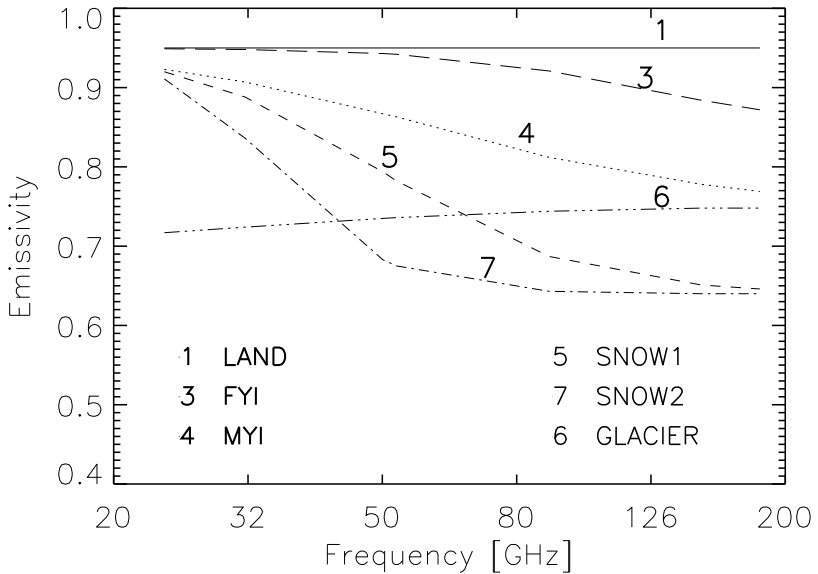
Figure 8.2: A priori emissivities ($\varepsilon_0(\nu)$) of different surface types. The emissivity of water depends on temperature and incidence angle (it is not shown). Coastline emissivities are computed as a mixture of land and water.

The surface type classifications are done by comparing the brightness temperatures at different frequencies. The footprint will be checked whether it is coming under either first-year ice or multiyearice if the absolute value of latitude of the corresponding foot print is greater than $42°$ and if $DF1$ is less than zero:

$$DF1 = 2.85 + 0.02\,T_b(23) - 0.028\,T_b(50) \tag{8.2}$$

where $T_b(23)$ is the brightness temperature measured at $23\,\text{GHz}$ and $T_b(50)$ is the brightness temperature measured at $50\,\text{GHz}$. In order to differentiate first-year from multiyear ice another parameter $DF4$ is used. It is defined as:

$$DF4 = T_b(23) - T_b(31) \tag{8.3}$$

If $DF4$ is less than 3 it is first-year ice and otherwise it is multiyear ice. In order to understand other surface type identification techniques, the reader is advised to refer Grody et al. (2000).

Each surface type is assigned an emissivity spectrum $\varepsilon_0(\nu)$, plotted versus frequency in Figure 8.2. However, because surface emissivity varies, the retrieval is allowed to adjust the surface brightness spectrum in order to fit the observation. The retrieval of surface brightness is combined with the atmospheric moisture profile (H) retrieval, using channels 1, 2, 3 and 15 of AMSU-A, and four AMSU-B channels (150, 183.3 ± 1, ± 3, ± 7). Surface brightness temperature is represented as a function of frequency (ν) by

$$T_{SB}(\nu) = \varepsilon_0(\nu)T_{S0} + T_0 + T_1 F_1(\nu) + T_2 F_2(\nu) \qquad (8.4)$$

where T_{S0} is the *a-priori* surface temperature, ε_0 is the *a-priori* surface emissivity, the parameters T_0, $T1$ and T_2 are part of the retrieval solution, with a priori values of zero and

$$F_1(\nu) = \frac{\nu^s}{(\nu^s + \nu_1^s)} \qquad (8.5)$$

$$F_2(\nu) = \frac{\nu^s}{(\nu^s + \nu_2^s)} \qquad (8.6)$$

The coefficients ν_1, ν_2 and s are assigned according to surface type, see Table 8.1. $F_1(\nu)$ and $F_2(\nu)$ both increase with frequency from zero to unity.

Table 8.1: Surface model parameters fixed by classification ($\sigma_{0,1,2,\rho}$= a priori standard deviations of T_0,T_1,T_2,P_ρ). The quantities ν_1 and ν_2 are in GHz and σ_0, σ_1 and σ_2 are in K. .

Type	Surface	s	ν_1	ν_2	σ_0	σ_1	σ_2	σ_ρ
0	coastline	1.2	90	...			0	0.12
1	land	1.2	90	...	15	20	0	0
2	water	1.5	50	...			0	0.12
3	FYI	3	40	120	10	10	10	0
4	MYI	3	40	120	10	10	10	0
5	snow1	3	50	150	20	20	20	0
6	glacier	3	40	120	20	20	20	0
7	snow2	3	33	90	20	20	20	0

To find the values of T_0, T_1 and T_2 the retrieval needs the Jacobian

matrix whose elements corresponding to these parameters are calculated, at any frequency, as partial derivatives with other parameters including surface temperature held constant:

$$\frac{\partial T_B(\theta)}{\partial T_0} = \frac{\partial T_B(\theta)}{\partial T_{SB}} = \tau(\theta)\Big(1 - \frac{T_{Bsky}(\theta_{ref})}{T_S}\Big) \tag{8.7}$$

$$\frac{\partial T_B(\theta)}{\partial T_1} = \frac{\partial T_b(\theta)}{\partial T_{SB}}F_1 \tag{8.8}$$

$$\frac{\partial T_B(\theta)}{\partial T_1} = \frac{\partial T_b(\theta)}{\partial T_{SB}}F_2 \tag{8.9}$$

where $T_B(\theta)$ is the upwards-propagating brightness temperature and $\tau(\theta)$ is the atmospheric transmittance along the path at angle θ from surface footprint to satellite, T_S is the estimated surface skin temperature, and $T_{Bsky}(\theta_{ref})$ is the downward-propagating sky brightness temperature.

8.3 Estimation Method

8.3.1 Outline

Retrievals are done at AMSU-A resolution. Therefore the AMSU-B measurements are weighted averages over 3×3 spatial arrays that approximate the AMSU-A footprint, nominally $50\,\mathrm{km}$ diameter near nadir. The input vector of measured brightness temperature is accompanied by an input validity vector whose elements are either one or zero. The principal steps in retrieval algorithm are the following (Rosenkranz, 2001):

1. Based on location and month, choose an *a-priori* temperature profile $\hat{T}_a$. Also calculate the magnetic field, which has a minor effect on the transmittance of channel 14.
2. Using location or other criteria, classify surface as discussed in Section 8.2. Compute *a-priori* surface brightness temperature for this class. This depends on the surface temperature by Eqn. 8.4.
3. Test for convergence of channels 1, 2, 3, 15, 17-20 brightness temperatures. If not converged, update the humidity (H) profile and the surface brightness temperature spectrum using these channels.

4. Test for convergence of channels 4 – 14. If not converged, update the temperature profile using these channels.

5. Return to step 2 if convergence did not occur in step 4; else to step 3 if convergence did not occur in step 3; else exit

8.3.2 Estimation of Temperature Profile

The cost function Equation (7.9) to be minimized is of the form

$$(\hat{T} - \hat{T}_a)^{\mathrm{T}} S_t^{-1}(\hat{T} - \hat{T}_a) + (T_b - T_B)^{\mathrm{T}} S_e^{-1}(T_b - T_B) \qquad (8.10)$$

where $\hat{T}$ is the estimate of temperature profile, $\hat{T}_a$ is the *a-priori* temperature profile, S_t is the temperature covariance matrix, T_b is the measured brightness temperature, T_B is the modeled brightness temperature and S_e is the brightness temperature covariance matrix.

Given an existing estimate $\hat{T}_{n-1}$, the next estimated profile is determined from a vector T_b of observed brightness temperatures for channels 4–14.

8.3.3 Convergence Test

Convergence is tested separately for the temperature channels in step 4 and for the moisture/surface channels in step 3. Iteration of both steps are suspended when either one of the following conditions is met:

1. computed brightness temperature vector T_B meets the noise closure criterion

$$\sum_{i=1}^{N_B}[T_{bi} - T_{Bi}]^2 \Delta T_i^{-2} \le N_B \qquad (8.11)$$

   where ΔT_i^{-2} is the instrument noise on channel i and N_B is the number of valid elements in T_b

2. when successive computations of the left side of Eqn. 8.11 change by less than 1% for the temperature channels and 2% for the moisture/surface channels

3. when the number of iterations exceeds a given limit

8.4 Comparison of Retrieved Temperature Profiles
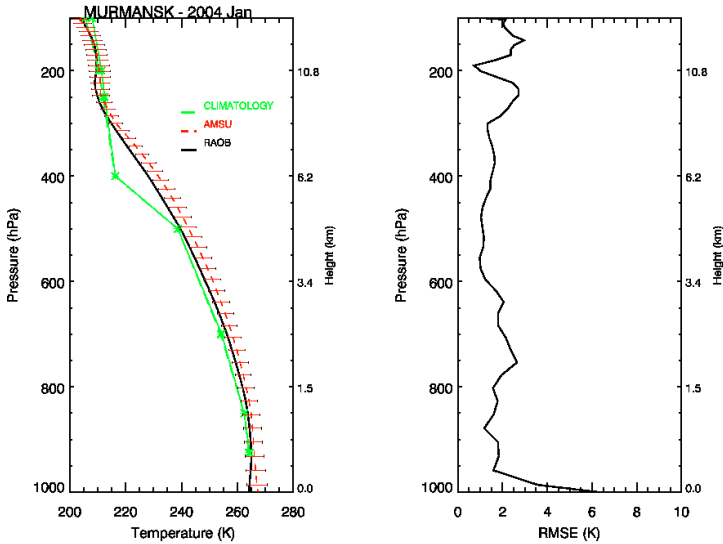
Figure 8.3: Comparison of the retrieved temperature profiles with the radiosonde measurements (Murmansk,January 2004). The error bars represent standard deviation.
Left panel: red line represents averaged temperature profiles retrieved from AMSU measurements, black line represents the average temperature profiles from radiosondes and green line represents climatology of temperature used for the retrieval of temperature profiles from AMSU measurements.
Right panel: root mean square (rms) difference between temperature profiles measured by radiosondes and the temperature profiles retrieved using collocated AMSU measurements.

The retrieved temperature profiles are compared with measurements made by different stations in the polar regions. Radiosonde stations in polar regions are mostly located near coastline where surface type and emissivity might change within the sensor footprint. Fig. 8.3 shows a sample comparison of AMSU retrieved temperature profiles with the collocated radiosonde observation for the station Murmansk

$(68°58'$ N $33°3'$ E) for the month January 2004 and also the root mean square difference between the retrieved profiles and the radiosonde temperature profiles. Collocations are done within a time window of ± 3 hours and space window of ± 100 km. Error bars represent standard deviation. Large deviations are observed near the surface.
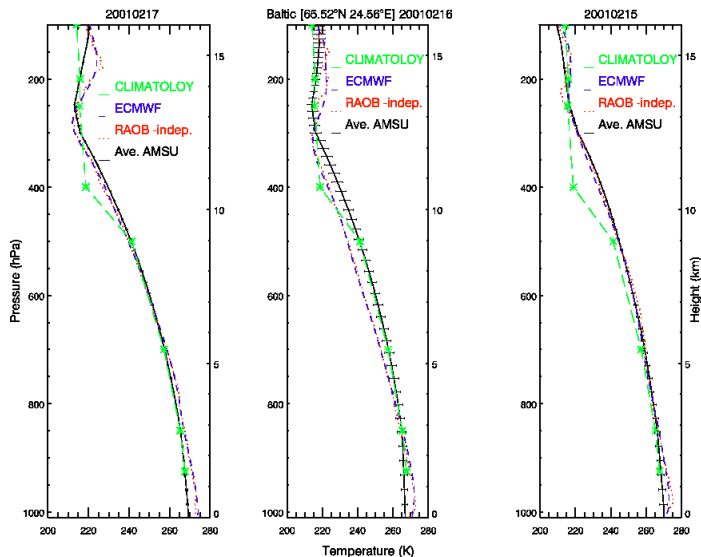
Figure 8.4: Comparison of temperature profiles from different sources (Baltic Sea February 2001); black: AMSU retrieved, green:climatology, violet: ECMWF red: radiosondes. The error bars represent standard deviation. Left panel: Profiles on 17/02/2001. Middle panel: Profiles on 16/02/2001. Left panel: Profiles on 15/02/2001.

The suitability of ECMWF model profiles instead of those from radiosondes for the comparison with AMSU retrieved temperature profiles is demonstrated in Fig. 8.4. Three profiles obtained from a research expedition conducted in the Baltic Sea in 2001 February, which are not assimilated into ECMWF model have been compared with collocated ECMWF profiles and retrieved temperature profiles from AMSU. The error bars indicate the standard deviation. The ECMWF model profiles show good agreement with radiosonde measurements, however

AMSU profiles show deviations, especially near the surface. A possible reason for the deviations of profiles in the Baltic area, or indeed any location close to a coastline, is the simple estimate of the land fraction within the AMSU-A footprint, which is set either to 0 or 1 according to the surface elevation at the center of the footprint; this is a difference from the version of the algorithm in Rosenkranz (2006). Therefore the forward calculation may be starting with an a-priori surface emissivity that is very different from the average over the AMSU-A. footprint. In order to study the temperature profile variation with emissivity variation over sea ice, in-situ observations with homogeneous surface type within the sensor footprint, e.g., from research vessels, are still required.

9 Modification of the Surface Brightness Model for the Temperature Retrieval over Sea Ice

9.1 Introduction

In polar regions, especially over sea ice, there are not enough in-situ measurements of atmospheric parameters because of the remoteness of the region. Also the conventional retrievals, using satellite-borne radiometers do not yield good results because of the variation of surface emissivity and surface temperature. Microwave radiation can easily penetrate a few tens of centimeter of snow and a few centimeters of ice. During winter the air temperature is much below freezing temperature and the water underneath is at around $-2\,°C$. Therefore, a large gradient between temperature on top of the snow and below the ice exists. So its very difficult to quantify the brightness temperatures. Here, an existing temperature retrieval method (Rosenkranz, 2006) using AMSU measurements are modified to improve the temperature profile retrieval over sea ice. The modification are:

1. provide varying *a-priori* surface emissivities for each month
2. regress the lower level air temperature to emitting layer temperature
3. modify surface brightness temperature retrieval.

The following sections describe the modifications applied to the temperature retrieval method in detail and give some results.

The surface emissivity of sea ice varies spatially and temporally. Determination of emissivity requires the knowledge of the temperature of the emitting layer. The penetration depth of microwaves varies between millimeters and decimeters depending on the frequency and

microphysical structure of the sea ice. In most of the studies on sea ice emissivity the temperature of the emitting layer has been assumed to be equal to the surface temperature measured by infrared instruments. This is a potential source of error because of the temperature gradient in the sea ice.

9.2 A-priori Emissivities and Emitting Layer Temperatures

The emissivities retrieved using AMSU measurements described in Chapters 4, 5 and 6 are used as the *a-priori* emissivities, which accounts for the variation of the penetration depth with frequency, air temperature and sea ice temperature. Emissivities are retrieved from two selected regions in the Arctic, one covered by first-year ice and the other by multiyear ice. In general retrieval scheme described in Chapter 8, the lower most atmospheric temperature from the climatology is used as the surface temperature and it is a single temperature for all frequencies. In the modified retrieval method for sea ice, during the winter months, the surface temperature (the emitting layer temperature) is a frequency-dependent quantity. It is derived from the lowest level air temperature (Mathew et al., 2006) with regression coefficients derived for each frequency. Details can be seen in Chapter 5. The new *a-priori* emissivities are shown in the Table 9.1 for first-year ice and Table 9.2 for multiyear ice and the regression coefficients to derive the emitting layer temperature are shown in Table 5.2 and Table 5.3.

9.3 Surface Brightness Temperature Covariance Matrices

Using the surface temperature (emitting layer temperature) and emissivity the *a-priori* surface brightness temperature in the modified retrieval algorithm will be

$$T_{SB}(\nu) = \varepsilon_0(\nu) T_{S0}(\nu) \tag{9.1}$$

Table 9.1: Average emissivity values for the first-year ice. Note: For July and August emissivity of June is assumed and for September and October emissivity of November is assumed.

	23 GHz	31 GHz	50 GHz	89 GHz	150 GHz
Jan	0.943	0.941	0.941	0.878	0.796
Feb	0.925	0.922	0.920	0.863	0.804
Mar	0.941	0.931	0.895	0.806	0.745
Apr	0.940	0.929	0.893	0.810	0.731
May	0.916	0.909	0.893	0.821	0.768
Jun	0.824	0.825	0.837	0.826	0.801
Jul	0.824	0.825	0.837	0.826	0.801
Aug	0.824	0.825	0.837	0.826	0.801
Sep	0.926	0.928	0.937	0.909	0.861
Oct	0.926	0.928	0.937	0.909	0.861
Nov	0.926	0.928	0.937	0.909	0.861
Dec	0.936	0.936	0.944	0.904	0.851

Table 9.2: Average emissivity values for the multiyear ice.

	23 GHz	31 GHz	50 GHz	89 GHz	150 GHz
Jan	0.851	0.807	0.779	0.782	0.779
Feb	0.852	0.810	0.781	0.786	0.789
Mar	0.851	0.805	0.769	0.778	0.777
Apr	0.832	0.790	0.756	0.773	0.752
May	0.854	0.826	0.824	0.825	0.795
Jun	0.920	0.904	0.879	0.818	0.768
Jul	0.894	0.887	0.880	0.854	0.836
Aug	0.830	0.798	0.770	0.762	0.765
Sep	0.810	0.772	0.750	0.734	0.724
Oct	0.821	0.778	0.727	0.689	0.667
Nov	0.827	0.779	0.717	0.700	0.697
Dec	0.852	0.805	0.763	0.758	0.766

where T_{SB} is the surface brightness temperature, ε_0 is the *a-priori* emissivity and T_{S0} is the surface temperature (emitting layer temperature).

Surface brightness temperatures are calculated using the retrieved emissivity and the surface temperatures using the Eqn. 9.1. The covariances of surface brightness temperature can be written as

$$\Sigma_{ij} = \mathrm{E}\Big(\big(B_t(\nu_i) - \bar{B}_t(\nu_i)\big)\big(B_t(\nu_j) - \bar{B}_t(\nu_j)\big)\Big) \tag{9.2}$$

where $B_t(\nu_i)$ is the surface brightness temperature of i-th window channel, $\bar{B}_t(\nu_i) = \mathrm{E}\big(B_t(\nu_i)\big)$, the expected value of i-th entry. $B_t(\nu_j)$ is the surface brightness temperature of j-th window channel and $\bar{B}_t(\nu_j) = \mathrm{E}\big(B_t(\nu_j)\big)$ is the expected value of j-th entry. The surface covariance matrices for first-year ice and multiyear surface for all the 12 months of the year 2005 are added in the appendix A. Now we have the surface brightness measurements from satellite, *a-priori* surface brightness temperatures and the surface brightness temperature covariance matrices. Therefore, instead of retrieving the correction parameters T_0, T_1 and T_2, now we retrieve the surface brightness temperature using the iteration solution equation Eqn. 7.20

$$\boldsymbol{x_{n+1}} = \boldsymbol{x_n} + \boldsymbol{S_a K_n}^{\mathrm{T}} \big(\boldsymbol{K_n S_a K_n}^{\mathrm{T}} + \boldsymbol{S_e}\big)^{-1}$$
$$\big(\boldsymbol{y} - \boldsymbol{F(x_n)} + \boldsymbol{K_n(x_n - x_a)}\big) \quad (7.20)$$

where, the state vector $\boldsymbol{x}$ is the surface brightness temperatures.

9.4 Comparison of Retrieved Profiles

Figure 9.1 shows the comparison of retrieved temperature profile from AMSU data with collocated ECMWF temperature profiles over a first-year ice region in the Kara sea for March 2003. The left panel shows averaged difference between retrieved temperature profiles and collocated ECMWF model temperature profiles. The solid line represents the unmodified retrieval and the dashed line shows the modified retrieval. The right panel shows the root mean square (rms) difference between retrieved temperature profiles and collocated ECMWF model
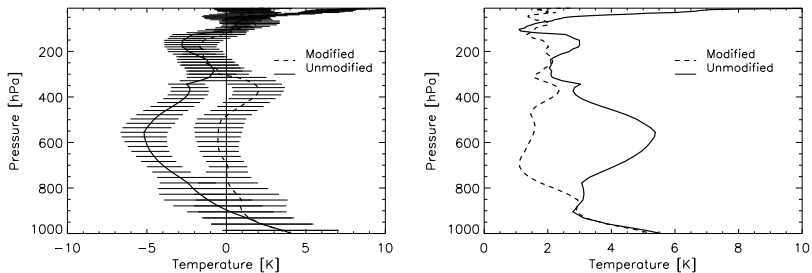
Figure 9.1: Left panel: Averaged difference between temperature profiles from modified and unmodified retrieval and ECMWF model temperature profiles over first-year ice.
Right panel: Root mean square (rms) difference between temperature profiles from modified and unmodified retrieval and ECMWF model temperature profiles over first-year ice.
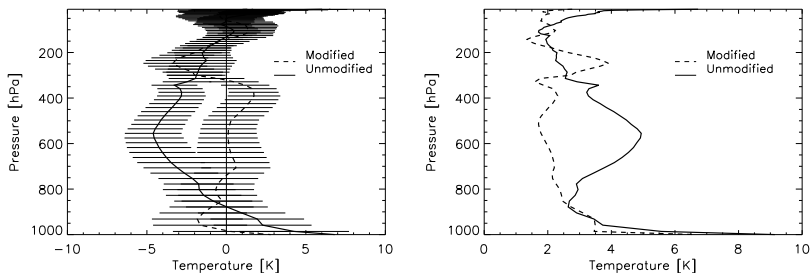
Figure 9.2: Left panel: Averaged difference between temperature profiles from modified and unmodified retrieval and ECMWF model temperature profiles over multiyear ice.
Right panel: Root mean square (rms) difference between temperature profiles from modified and unmodified retrieval and ECMWF model temperature profiles over multiyear ice.

temperature profiles. The solid line represents the unmodified retrieval
and the dashed line represents the modified retrieval. Figure 9.2 shows
the comparison of retrieved temperature profile from AMSU data with
collocated ECMWF temperature profiles over a multiyear ice region in
the North of Greenland for 2003 March. The left panel shows aver-
aged difference between retrieved temperature profiles and collocated
ECMWF model temperature profiles. The solid line represents the un-
modified retrieval and the dashed line shows the modified retrieval.
The right panel shows the root mean square (rms) difference between
retrieved temperature profiles and collocated ECMWF model temper-
ature profiles.

The temperature profiles from the modified retrieval show good
agreement with the model temperature profiles from ECMWF. The
temperature profiles from unmodified retrieval show deviations from
ECMWF temperature profiles up to about 6 K especially from 900 hPa
till 300 hPa. Those discrepancies could be corrected with the new
method of temperature profile retrieval over sea ice. In-situ measure-
ments are required to compare the modified profiles in order to con-
clude the degree of reliability of the present retrieval method over sea
ice.

10 Conclusion and Outlook

The surface emissivity of sea ice is determined using the data from
the passive microwave instruments AMSU and AMSR-E.

The penetration depth of microwaves in sea ice varies between
millimeters and decimeters depending on the frequency and micro-
physical structure. Therefore, in order to find the relation between
the emitting layer temperature and the lowest layer air temperature, a
year-round observation of temperature profiles from the Surface Heat
Budget of the Arctic Ocean (SHEBA) campaign at a first-year and a
multiyear ice site are analyzed. A linear relation between the emit-
ting layer temperature and the lowest level air temperature has been
established. A set of coefficients a and b is derived to linearly relate
the lowest level air temperature and the different emitting layer tem-
peratures. The method accounts for the variation of the penetration
depth with frequency, air temperature, sea ice temperature and the
snow depth.

Applying the regression coefficients, lowest level air temperatures
are corrected to emitting layer temperatures. Corrections are required
to lower frequencies and for winter seasons. During winter, sea ice
is covered with snow and the temperature gradient in snow cover is
higher than in sea ice. During the summer months, first year ice/snow
cover melts and no temperature variation is dominant for multiyear
ice.

Angular and frequency dependence of the emissivity of first-year
ice and multiyear ice are studied. The local zenith angle variation of
AMSU emissivities up to $45°$ corresponding to scan positions 4 to 27
for AMSU-A and 10 to 81 for AMSU-B is negligible. For higher incidence
angles the emissivity decreases. As the frequency increases, the emis-

sivity decreases for sea ice. For young ice the variation of emissivity with frequency is smaller.

The monthly variations of emissivities for different frequencies are derived for the specific regions for the whole year 2005. The ice concentrations of the region are also noticed. During the summer months first-year ice melts and emissivities drop those of open water whereas for multi-year ice a slight increase in emissivity is observed. The frequency dependence of the emissivity varies in different months, especially at high frequencies due to the variation of snow cover. Multi-year ice emissivities at 89 GHz and I50 GHz show larger variations (maximum up to 40%) during the summer months June, July, August and September. Emissivity maps are produced to document the emissivity variations for different surface types.

From the imaging microwave sensor AMSR-E sea ice emissivities are retrieved at the same two test regions as for AMSU. The frequency variation and seasonal variation of first-year ice and multiyear ice emissivities are studied for all AMSR-E frequencies at both horizontal and vertical polarization.

AMSR-E measures radiance at both horizontal and vertical polarizations whereas AMSU measures only in one mixed polarizations mode. The AMSR-E retrieved emissivities at two polarizations are combined together to simulate the AMSU polarization combinations for comparison. The AMSR-E emissivity and AMSU emissivity are in good agreement.

An existing temperature retrieval algorithm (Rosenkranz, 2006) is modified to improve the temperature profile over sea ice by using the retrieved sea ice emissivities from AMSU and the derived temperature correction factors. The modification of the algorithm is done by:

1. providing varying *a-priori* surface emissivities for each month
2. deriving the emitting layer temperature from the lower level air temperature
3. modifying surface brightness temperature retrieval.

Temperature profiles are retrieved with the modified algorithm and compared with ECMWF model temperature profiles. The modification improves the retrieval of temperature profiles. However, the modification in surface brightness has propagated to the pressure levels be-

tween 900 hPa and 300 hPa because the solution for the temperature profile uses the channels with lower weighting functions to correct for the contribution of the troposphere to the channels that are higher in the atmosphere.

The temperature correction factors are derived using the sea ice temperature profiles from two SHEBA measurement cites. The snow depth of those two regions are assumed for the emissivity test regions. The snow depth and snow properties varies with space and time. This contributes to the error in the retrieved emissivities.

In this thesis temperature profiles are retrieved only in two test regions each covered by ice of just one type. However, in general the emission received from a satellite footprint contains contributions from all different surface types such as first-year ice, multiyear ice and open water which may occur within a footprint. So the surface brightness temperature retrieval to be applicable over all sea ice surfaces, contribution from all surface types should be considered. This is a task for future research.

The retrieved temperature profiles are compared with ECMWF model profiles. In principle, it would be preferable to use radiosonde profiles for this purpose because of their higher resolution and complete independence. However, they are very rare over sea ice of concentration near 1, especially if ice of just one type is required. A comparison in the Baltic has revealed a good coincidence of ECMWF and radiosonde profiles (Chapter 9).

In fact, the surface emissivity retrieval method is promising. The retrieved emissivities and derived emitting layer temperatures could improve the temperature retrieval over sea ice.

Appendix

A Surface Covariance Matrices

Table A.1: Surface brightness covariance matrices for the first-year ice (January to June).

Month	ν	23 GHz	31 GHz	50 GHz	89 GHz	150 GHz
	23 GHz	22.91	22.27	22.07	17.99	19.59
	31 GHz	22.27	21.81	22.58	19.89	23.67
Jan	50 GHz	22.07	22.58	34.24	43.89	67.24
	89 GHz	17.99	19.89	43.89	77.53	134.97
	150 GHz	19.59	23.67	67.24	134.97	257.68
	23 GHz	88.73	83.34	62.54	37.20	4.49
	31 GHz	83.34	79.07	62.95	43.64	17.84
Feb	50 GHz	62.54	62.95	73.17	77.29	82.77
	89 GHz	37.20	43.65	77.29	120.46	167.41
	150 GHz	4.49	17.85	82.77	167.41	277.48
	23 GHz	3.88	3.85	4.52	5.68	8.23
	31 GHz	3.85	4.02	5.41	6.68	9.39
Mar	50 GHz	4.52	5.41	12.61	13.36	18.65
	89 GHz	5.68	6.68	13.36	19.95	32.52
	150 GHz	8.23	9.39	18.65	32.52	61.11
	23 GHz	5.96	5.93	8.37	1.46	-12.19
	31 GHz	5.92	6.18	9.55	3.14	-10.28
Apr	50 GHz	8.37	9.55	19.37	11.74	-4.59
	89 GHz	1.45	3.14	11.74	21.70	33.61
	150 GHz	-12.19	-10.28	-4.59	33.60	111.78
	23 GHz	19.83	18.05	7.39	-13.28	-28.94
	31 GHz	18.05	17.05	8.97	-7.46	-20.37
May	50 GHz	7.39	8.97	16.71	24.93	29.66
	89 GHz	-13.28	-7.46	24.93	88.63	136.81
	150 GHz	-28.94	-20.37	29.66	136.81	246.95
	23 GHz	212.04	187.76	121.72	6.17	-45.57
	31 GHz	187.76	174.65	132.46	42.93	-2.42
Jun	50 GHz	121.72	132.46	156.19	133.75	110.07
	89 GHz	6.17	42.93	133.75	217.25	245.01
	150 GHz	-45.57	-2.42	110.07	245.02	337.57

Table A.2: Surface brightness covariance matrices for the first-year ice (July to December).

Month	ν	23 GHz	31 GHz	50 GHz	89 GHz	150 GHz
	23 GHz	447.41	415.11	346.76	203.06	124.80
	31 GHz	415.11	387.62	326.91	195.78	119.96
Jul	50 GHz	346.76	326.91	287.01	182.82	116.95
	89 GHz	203.06	195.78	182.82	135.41	100.35
	150 GHz	124.80	119.96	116.95	100.33	115.29
	23 GHz	32.96	37.55	49.94	51.45	40.24
	31 GHz	37.55	46.06	61.29	62.37	43.77
Aug	50 GHz	49.94	61.29	89.33	92.99	71.77
	89 GHz	51.45	62.37	92.99	106.16	103.42
	150 GHz	40.24	43.77	71.77	103.42	169.63
	23 GHz	40.06	45.54	60.20	56.84	18.69
	31 GHz	45.54	55.12	73.32	68.17	16.60
Sep	50 GHz	60.20	73.32	107.41	102.30	38.12
	89 GHz	56.84	68.17	102.30	108.17	72.33
	150 GHz	18.69	16.60	38.12	72.33	172.91
	23 GHz	1391.45	1297.45	1095.57	664.60	411.22
	31 GHz	1297.45	1211.31	1024.71	624.64	388.26
Oct	50 GHz	1095.57	1024.71	879.88	542.54	343.99
	89 GHz	664.60	624.64	542.54	345.92	231.91
	150 GHz	411.22	388.26	343.99	231.91	188.76
	23 GHz	27.67	25.12	14.81	0.42	-13.79
	31 GHz	25.12	23.15	14.98	2.79	-9.30
Nov	50 GHz	14.81	14.98	16.96	12.70	8.61
	89 GHz	0.42	2.79	12.70	22.29	33.00
	150 GHz	-13.79	-9.30	8.61	33.00	65.32
	23 GHz	37.49	35.24	24.74	11.02	-0.74
	31 GHz	35.24	33.49	25.23	13.79	5.65
Dec	50 GHz	24.74	25.23	30.24	29.33	38.80
	89 GHz	11.02	13.79	29.33	47.47	86.03
	150 GHz	-0.741	5.65	38.80	86.03	180.60

Table A.3: Surface brightness covariance matrices for the multiyear ice (January to June).

Month	ν	23 GHz	31 GHz	50 GHz	89 GHz	150 GHz
	23 GHz	6.79	9.70	21.13	10.17	12.40
	31 GHz	9.70	17.74	33.85	16.96	19.40
Jan	50 GHz	21.13	33.85	72.95	34.20	41.81
	89 GHz	10.17	16.96	34.20	24.19	31.16
	150 GHz	12.40	19.40	41.81	31.16	55.44
	23 GHz	4.70	8.14	14.64	11.37	15.60
	31 GHz	8.14	16.67	28.53	18.57	24.40
Feb	50 GHz	14.64	28.53	56.96	38.80	56.48
	89 GHz	11.37	18.57	38.80	40.01	60.79
	150 GHz	15.60	24.40	56.48	60.79	99.72
	23 GHz	5.34	9.32	17.57	11.47	14.73
	31 GHz	9.32	18.55	34.11	21.33	27.76
Mar	50 GHz	17.57	34.11	70.29	41.84	55.77
	89 GHz	11.47	21.33	41.84	32.76	42.74
	150 GHz	14.73	27.76	55.77	42.74	57.91
	23 GHz	8.51	11.86	21.64	15.05	15.00
	31 GHZ	11.86	18.89	33.68	21.12	22.36
Apr	50 GHz	21.63	33.68	65.10	39.51	44.04
	89 GHz	15.05	21.11	39.51	30.45	31.67
	150 GHz	15.00	22.36	44.04	31.67	39.08
	23 GHz	33.23	37.27	45.41	27.72	15.93
	31 GHz	37.27	46.26	60.08	38.39	31.23
May	50 GHz	45.41	60.08	85.36	57.57	58.10
	89 GHz	27.70	38.39	57.57	49.01	59.64
	150 GHz	15.93	31.23	58.10	59.65	109.10
	23 GHz	84.49	99.75	108.47	81.51	82.86
	31 GHz	99.75	128.05	167.47	149.11	154.09
Jun	50 GHz	108.47	167.47	313.85	347.86	360.77
	89 GHz	81.51	149.11	347.86	452.07	509.16
	150 GHz	82.86	154.09	360.77	509.16	750.14

Table A.4: Surface brightness covariance matrices for the multiyear ice (July to December).

Month	ν	23 GHz	31 GHz	50 GHz	89 GHz	150 GHz
Jul	23 GHz	19.60	24.68	38.41	39.86	49.78
	31 GHz	19.60	24.68	38.41	39.86	49.78
	50 GHz	38.41	87.71	214.12	294.08	346.97
	89 GHz	39.86	111.59	294.08	431.65	519.37
	150 GHz	49.78	131.15	346.97	519.37	707.33
Aug	23 GHz	148.52	211.29	246.19	162.41	126.80
	31 GHz	211.29	312.85	385.88	275.59	229.90
	50 GHz	246.19	385.88	528.33	428.29	404.24
	89 GHz	162.41	275.59	428.29	408.89	433.84
	150 GHz	126.80	229.90	404.24	433.84	569.17
Sep	23 GHz	69.76	93.43	126.30	112.88	128.16
	31 GHz	93.43	127.46	173.73	159.95	181.77
	50 GHz	126.30	173.73	248.50	242.29	283.21
	89 GHz	112.88	159.95	242.29	275.99	342.64
	150 GHz	128.16	181.77	283.21	342.64	470.77
Oct	23 GHz	23.02	33.71	51.15	32.49	39.33
	31 GHZ	33.71	50.46	76.98	50.30	58.49
	50 GHz	51.15	76.98	124.93	84.84	96.64
	89 GHz	32.49	50.30	84.84	73.25	89.91
	150 GHz	39.33	58.49	96.64	89.91	128.44
Nov	23 GHz	14.84	24.11	37.48	24.10	24.27
	31 GHz	24.11	40.62	61.50	36.66	36.71
	50 GHz	37.48	61.50	99.05	64.46	68.17
	89 GHz	24.10	36.66	64.46	78.71	90.91
	150 GHz	24.27	36.71	68.17	90.91	116.79
Dec	23 GHz	7.50	12.50	19.69	13.91	14.59
	31 GHz	12.50	22.84	34.56	20.85	21.56
	50 GHz	19.69	34.56	60.26	41.75	47.80
	89 GHz	13.91	20.85	41.75	54.18	65.29
	150 GHz	14.59	21.56	47.80	65.29	86.18

B Acknowledgments

I would like to thank Dr. Georg Heygster for giving me an opportunity to do my PhD. His support throughout the project was incredible. Georg, a man full of love and kindness, was always there to answer all my question and to guide me.

All my present and former colleagues made my work a simple task. I thank my present colleagues Christian Melsheimer, Jens Borgmann, Parag Narvekar, Heidrun Wiebe, Nathalie Courcoux, Mashrab Kuvatov and Lothar Meyer-Lerbs for their help and support.

I acknowledge the help of my former colleagues, Jungang Miao, Nathalie Selbach, Jens Dannenberg, Hendrik Laue, Hong Gang, Poornendu Prathap Singh, Gunnar Spreen and Lars Kaleschke.

I would like to thank Prof. Rosenkranz for the temperature retrieval code and his willingness to answer all my questions.

I would like to thank the SAT group for giving all the required data and the processing platforms.

Thanks to Viju Oomman John for introducing to me the University, Sreerekha T. R. for being there to hear all my struggles, feelings, frustrations and jokes. Also, Stefanie Buehler, Prof. Bleck-Neuhaus, PIP and PEP team for making my stay in Germany easier, especially in the beginning.

I extend my gratitude towards Prof. Justus Notholt and Prof. Lars Kaleschke for reviewing my thesis and for their valuable comments.

The workers and members of the New Testament Church made my days in Germany a sweet experience. I am indebted to their unlimited love, encouragement and prayers.

My husband Remsy Tharakan and my son George Stephen Tharakan came into my life during the course of my thesis. Without their love, co-operation and support this thesis would never have been pos-

C Bibliography

Andrews, D. G., 2000: *An Introduction to Atmospheric Physics*. Cambridge University Press.

Barber, D. G., Fung, A. K., Grenfell, T. C., Nghiem, S. V., Onstott, R. G., Lytle, V. I., Perovich, D. K. and Gow, A. J., 1998: The role of snow on microwave emission and scattering over first-year sea ice. *IEEE Trans. Geosci. Rem. Sens.*, **36**, 5, 1750–1763.

Buehler, S. A., Kuvatov, M. and John, V. O., 2005: Scan asymmetries in AMSU-B data. *Geophys. Res. Lett.*, **32**.

Comiso, J. C., 1983: Sea Ice Effective Microwave Emissivities From Satellite Passive Microwave and Infrared Observations. *J. Geophys. Res.*, **88**, C12, 7686–7704.

Comiso, J. C., Cavalieri, D. J. and Markus, T., 2003: Sea Ice Concentration, Ice Temperature, and Snow Depth Using AMSR-E Data. *IEEETGRS*, **41**, 2, 243–252.

Comiso, J. C. and Kwok, R., 1996: Surface and radiative characteristics of summer Arctic sea ice cover from multi-sensor satellite observations. *J. Geophys. Res.*, **101**, C12, 28,397–28,416.

English, S. J. and Hewison, T. J., 1998: A fast generic millimeter-wave emissivity model. *Proceedings of SPIE*, **3503**, 288–300.

Eppler, D., Farmer, L. D., Lohanick, A. W., Anderson, M. R., Cavalieri, D. J., Comiso, J., Gloersen, P., Garrity, C., Grenfell, T. C., Hallikainen, M., Maslanik, J. A., Mätzler, C., Melloh, R. A., Rubinstein, I. and Swift, C. T., 1992: Passive Microwave Signatures of Sea Ice. In *Microwave remote sensing of sea ice*, Carsey, F. D., ed., AGU Monograph, 68, Washington, D.C.: Am. Geophys. Union, 47–71.

Felde, G. W. and Pickle, J. D., 1995: Retrieval of 91 and 150 GHz

Earth surface emissivities. *J. Geophys. Res.*, **100**, D10, 20,855–20,866.

Fuhrhop, R., Grenfell, T. C., Heygster, G., Johnson, K.-P., Schrader, P. S. M. and Simmer, C., 1998: A combined radiative transfer model for sea ice, open ocean and atmosphere. *Radio Sci.*, **33**, 2, 303–316.

Fuhrhop, R., Simmer, C., Schrader, M., Heygster, G., Johnson, K.-P. and Schüssel, P., 1997: *Study of Passive Remote Sensing of the Atmosphere and Surface Ice*. Tech. Rep., Institut für Meereskunde, Kiel.

Garrity, C., 1992: Characterization of Snow on Floating Ice and Case Studies of Brightness Temperature Changes During the Onset of Melt. In *Passive Microwave Signatures of Sea Ice*, Carsey, F. D., ed., AGU Monograph, 68, Washington, D.C.: AGU, 313–328.

Goodrum, G., Kidwell, K. B. and Winston, W., 2000: *NOAA KLM USER'S GUIDE*. U.S. Department of Commerce, National Oceanic and Atmospheric Administration.

Grenfell, T. C., 1992: Surface-Based Passive Microwave Studies of Multiyear Sea Ice. *J. Geophys. Res.*, **97**, C3, 3485–3501.

Grenfell, T. C. and Lohanick, A. W., 1985: Temporal variations of the Microwave Signatures of Sea Ice During the Late Spring and Early Summer Near Mould Bay NWT. *J. Geophys. Res.*, **90**, C3, 5063–5074.

Grody, N., Weng, F. and Ferraro, F., 2000: Application of AMSU for obtaining hydrological parameters. In *Microwave Radiometry and Remote Sensing of the Earth' s Surface and Atmosphere*, Pampaloni, P. and Paloscia, S., eds., VSP, Netherlands, 339–352.

Haggerty, J. A. and Curry, J. A., 2001: Variability of sea ice emissivity estimated from airborne passive microwave measurements during FIRE SHEBA. *J. Geophys. Res.*, **106**, D14, 15 265–15 277.

Haggerty, J. A. and Curry, J. A., 2002: Potential for estimating cloud liquid water path over sea ice from airborne passive microwave measurements. *J. Geophys. Res.*, **107**, D1, AAC2–1–AAC2–13.

Hallikainen, M. and Winebrenner, D. P., 1992: The physical basis of sea ice remote sensing. In *Microwave remote sensing of sea ice*, Carsey, F. D., ed., AGU Monograph, 68, Washington, D.C.: Am. Geophys. Union, 29–46.

Hewison, T. J. and English, S. J., 1999: Airborne Retrievals of Snow and Ice Surface Emissivity at Millimeter Wavelengths. *IEEE Trans. Geosci. Rem. Sens.*, **37**, 4, 1871–1879.

Heygster, G., Melsheimer, C., Mathew, N., Toudal, L., Saldo, R., Andersen, S., Tonboe, R., Schyberg, H., Tveter, F. T., Thyness, V., Gustafsson, N., Landelius, T., Dahlgren, P. and Perov, V., 2006: *Integrated Observation and Modeling of the Arctic Sea ice and Atmosphere.* Tech. Rep., IUP, University of Bremen. Final Report for EU project EVK-CT-2002-00067.

Hollinger, J. P., B. E. Troy, J., Ramseier, R. O., Asmus, K. W., Hartman, M. F. and Luther, C. A., 1984: Microwave Emission From High Arctic Sea Ice During Freeze-up. *J. Geophys. Res.*, **89**, C5, 8104–8122.

Hong, G., Heygster, G. and Kunzi, G., 2005: Detection of tropical deep convective clouds from AMSU-B water vapor channels measurements. *J. Geophys. Res.*, **110**, D05205, 1–15.

Hong, G., Heygster, G., Kunzi, K., Wanbiao, L., Yuanjing, Z. and Bolin, Z., 2003: Retrieval of Microwave Surface Emissivities at TMI Frequencies in Shouxian. *Advances in Atmospheric Science*, **20**, 2, 253–259.

Houghton, J., 2002: *The Physics of Atmosphere.* ISBN 0-512-01122-1, Cambridge university press.

Houghton, J. T., Taylor, F. W. and Rodgers, C. D., 1983: *Remote sounding of atmosphere.* Cambridge university press, Cambridge.

Janssen, M. A. (Ed.), 1993: *Atmospheric remote sensing by microwave radiometry.* Wiley series in remote sensing, New York: John Wiley & Sons, Inc. 572 pp.

JAXA, 2005: *AMSR-E Data Users Handbook.* Japan Aerospace Exploration Agency (JAXA), 1401 Numanoue, Ohashi, Hatoyama-machi, Hiki-gun, Saitama, Japan.

Kaleschke, L., Lüpkes, C., Vihma, T., Haarpaintner, J., Bochert, A., Hartmann, J. and Heygster, G., 2001: SSM/I Sea Ice Remote Sensing for Mesoscale Ocean-Atmosphere Interaction Analysis. *Canadian Journal of Remote Sensing*, **27**, 5, 526–537.

Karbou, F., Aires, F., Prigent, C. and Eymard, L., 2005a: Potential of

AMSU-A and -B measurements for atmospheric temperature and humidity profiling over land. *J. Geophys. Res.*, **110**, D07109, 1–16.

Karbou, F., Prigent, C., Eymard, L. and Pardo, J., 2005b: Microwave land emissivity calculations using AMSU instruments. *IEEE Trans. Geosci. Rem. Sens.*, **43**, 5, 948–959.

Kawanishi, T., Sezai, T., Ito, Y., Imaoka, K., Takeshima, T., Ishido, Y., Shibata, A., Miura, M., Inahata, H. and Spencer, R. W., 2003: The Advanced Microwave Scanning Radiometer for the Earth Observing System (AMSR-E), NASDA's contribution to the EOS for global energy and water cycle studies. *IEEE Trans. Geosci. Rem. Sens.*, **41**, 2, 184–193.

Koenig-Langlo, G. and Marx, B., 1997: The Meteorological Information System at the Alfred Wegener Instiute. In *Climate and Environmental Database Systems*, Lautenschlager, M. and Reinke, M., eds., Kluwer Academic Publishers.

Lubin, L. and Massom, R., 2006: *Polar Remote Sensing: Atmosphere and Oceans*, vol. 1 of *ISBN: 3-540-43097-0*. Praxis Publishing,Chichester, UK.

Mathew, N., Heygster, G., Melsheimer, C. and ars Kaleschke, L., 2006: Surface emissivity of Arctic sea ice at AMSU window frequenc ies. *IEEE Trans. Geosci. Rem. Sens.* Submitted.

Mätzler, C., 2005: On the Determination of Surface Emissivity From Sattelite Observations. *IEEE Geosci. Rem. Sens. Lett.*, **2**, 2, 160–163.

Melsheimer, C. and Heygster, G., 2005: Retrieval of total water vapour over the Arctic from space-bourne microwave radiomater data. In *Reports on Marine Research 520/2006*, AWI Postdam.

Miao, J., Johnsen, K.-P., Kern, S., Heygster, G. and Kunzi, K., 2000: Signature of Clouds over Antarctic Sea Ice Detected by the Special Sensor Microwave/Imager. *IEEE Trans. Geosci. Rem. Sens.*, **38**, 5, 2333–2344.

Moore, T. E., Perovich, D. F. and Moritz, R. E., 2002: Preface. *J. Geophys. Res.*, **107**, C10.

Perovich, D. K., Elder, B. C. and Richter-Menge, J. A., 1997: Observation of the annual cycle of sea ice temperature and mass balance. *Geophys. Res. Lett.*, **24**, 5, 555–558.

Przybylak, R., 2003: *The Climate of the Arctic*. ISBN 1-4020-1134-2, Kluwer Academic Publishers.

Rodgers, C. D., 1976: REtieval of Retrieval of Atmospheric Temperature and Composition From Remote Measurements of Thermal Radiation. *Rev. Geophys. and Space Phys.*, 609–624.

Rodgers, C. D., 2000: *Inverse methods for atmospheric sounding theory and practice*, vol. 2. World Scientific Publihing Co. Pte. Ltd.

Rosenkranz, P. W., 2001: Retrieval of Temperature and Moisture Profiles From AMSU-A and AMSU-B Measurements. *IEEE Trans. Geosci. Rem. Sens.*, **39**, 11, 2429–2435.

Rosenkranz, P. W., 2003: Rapid Radiative Transfer Model for AMSU/HSB Channels. *IEEE Trans. Geosci. Rem. Sens.*, **41**, 2, 362–368.

Rosenkranz, P. W., 2006: Microwave radiative transfer model validation. *J. Geophys. Res.*, **111**, D09S07.

Selbach, N., 2003: *Determination of Total Water Vapour and Surface Emissivity of Sea Ice at 89 GHz,157 GHz and 183 GHz in the Arctic Winter*. Ph.D. thesis, University of Bremen.

Selbach, N., Hewison, T. J., Heygster, G., Miao, J., McGrath, A. J. and Taylor, J. P., 2003: Validation of total water vapor retrieval with an airborne millimeter-wave radiometer over Arctic sea ice. *Radio Sci.*, **38**, 4, MAR 26–1–MAR 26–8. ISBN 3-8325-0385-5.

Spreen, G., Kaleschke, L. and Heygster, G., 2005: Operational Sea Ice Remote Sensing with AMSRE-E 89 GHz Channels. In *2005 IEEE International Geoscience and Remote Sensing Symposium Proceedings*, IEEE, ed., 6.

Spreen, G., Kaleschke, L. and Heygster, G., 2007: Sea Ice Remote Sensing with AMSRE-E 89 GHz Channels. *J. Geophys. Res.*

Stogryn, A., 1971: Equation for calculating the dielectric constant of saline water. *IEEE transactions on microwave theory and techniques*, 733–736.

Tonboe, R., Andersen, S., Toudal, L. and Heygster, G., 2006: Sea ice emission modelling applications. In *Thermal Microwave Radiation – Applications for Remote Sensing*, Mätzler, C., Rosenkranz, P. W., Battaglia, A. and Wigneron, J. P., eds., IEE Electromagnetic Waves Series, IEE, London, UK.

Tonboe, R. T., 2006: Simulation of the seasonal sea ice microwave

surface emissivity variability at sounding frequencies. *IEEE Trans. Geosci. Rem. Sens.* Submitted.

Tucker III, W. B., Perovich, D. K., Gow, A. J., Weeks, W. F. and Drinkwater, M. R., 1992: Physical properties of sea ice relevant to remote sensing. In *Microwave remote sensing of sea ice*, Carsey, F. D., ed., AGU Monograph, 68, Washington, D.C.: Am. Geophys. Union, 9–28.

Ulaby, F. T., Moore, R. K. and Fung, A. K., 1981: *Microwave Remote Sensing, Active and Passive. Volume I: Fundamentals and radiometry.* Norwood, USA: Artech House.

Ulaby, F. T., Moore, R. K. and Fung, A. K., 1986: *Microwave Remote Sensing, Active and Passive. Volume III: From Theory to Applications.* 1990 edn., Norwood, USA: Artech House.

Uppala, S. M. et al., 2005: The ERA-40 re-analysis. *Q. J. R. Meteorol. Society*, **131**, 612, 2961–3012. DOI:10.1256/qj.04.176.

Warren, S. G., Rigor, I. G., Untersteiner, N., Radionov, V. F., Bryazgin, N. N., Aleksandrov, Y. I. and Colony, R., 1999: Snow depth on Arctic sea ice. *Journal of Climate*, **12**, 6, 1814–1829.

Weng, F., Yan, B. and Grody, N. C., 2001: A microwave land emissivity model. *J. Geophys. Res.*, **106**, D17, 22,115–20,123.

Weng, F., Zhao, L., Ferraro, R. R., Poe, G., Li, X. and Grody, N. C., 2003: Adavanced microwave sounding unit cloud and precipitation algorithms. *Radio Sci.*, **38**, 4.

Wentz, F. J., 1983: A model function for ocean microwave brightness temperatures. *J. Geophys. Res.*, **88**, C3, 1892–1908.